Studies on the molecular mechanism of selective ER degradation via autophagy

オートファジーによる選択的小胞体分解における分子機構の研究

2023年1月

千葉大学大学院　融合理工学府

石井俊輔

（千葉大学審査学位論文）

Studies on the molecular mechanism of selective ER degradation via autophagy

オートファジーによる選択的小胞体分解における分子機構の研究

2023年1月

千葉大学大学院　融合理工学府

石井俊輔

Table of Contents

ABSTRACT

The endoplasmic reticulum (ER) is a major cell compartment where protein synthesis, folding and post-translational modifications occur with assistance from a wide variety of chaperones and enzymes. Quality control systems selectively eliminate abnormal proteins that accumulate inside the ER due to cellular stresses or genetic mutations. ER-phagy, i.e., selective autophagy of the ER, is a mechanism that maintains or re-establishes cellular and ER-specific homeostasis through removal of abnormal proteins. However, how ER luminal proteins are recognized by the ER-phagy machinery remains unclear.

In this study, I applied the aggregation-prone protein, six-repeated islet amyloid polypeptide (6xIAPP), as a model ER-phagy substrate, which formed large aggreges inside the ER. I found that cell cycle progression 1 (CCPG1), which is an ER-phagy receptor, efficiently mediates 6xIAPP degradation via ER-phagy. I also identified prolyl 3-hydroxylase family member 4 (P3H4) as an endogenous cargo of CCPG1-dependent ER-phagy. The ER luminal region of CCPG1 contains several highly conserved regions among vertebrates that I refer to as cargo interaction regions (CIRs). I confirmed that CIR1 directly interacts with 6xIAPP and CIR2 binds directly to P3H4 in vitro. Notably, each of cargos were simultaneously recognized via different CIRs, suggesting that CIRs of CCPG1 determines specific luminal cargos for ER-phagy. Furthermore, cargo recognition via the luminal region of CCPG1 was represented to be independent of ER-phagy promotion activity. These findings indicate that CCPG1 is a bispecific ER-phagy receptor for ER luminal proteins and the autophagosomal membrane that contributes to the efficient removal of aberrant ER-resident proteins through ER-phagy.

INTRODUCTION

Proteins are fundamental macromolecules for living cells, and a human cell consists of a very high concentration of proteins (several billion protein molecules at total concentrations ranging from 50 ~ 300 mg/ml) (Srivastava and Bernhard, 1986; Albe *et al.*, 1990; Brown, 1991). Therefore, protein homeostasis, called "proteostasis", is crucial for physiological processes of the organisms. To assume proteostasis stability, a strict regulation of the synthesis and the degradation of proteins has evolutionally acquired. Cells synthesize wide variety of proteins from the genetic information, which are coordinately regulated by various signals derived from in/outside the cell. Environmental stimuli trigger several specific response pathways leading to transcriptional activation of (co-)factors that contribute to re-folding or degradation of misfolded proteins, which provide stress tolerance to cells. Furthermore changes in protein expression dynamics result in functional differentiation of individual cells and give rise to their characteristics. Protein degradation systems for excessive or misfolded proteins are also important to maintain proteostasis. Cells have two distinct protein degradation pathways, including the ubiquitin-proteasome system and the autophagy-lysosomal degradation system. Considering that the intracellular proteome consists of numerous kinds of different proteins, it is a big challenge for the degradation machinery to maintain cellular equilibrium in a highly crowded environment. However, harmful target materials are strictly monitored and efficiently removed by selective degradation mechanisms. A defect of the degradation pathways can lead to collapse the proteostasis that results in pathological onset which accounts for approximately 40% of human diseases (Bradbury, 2003).

The endoplasmic reticulum (ER) is the largest organelle and synthesizes approximately 35% of the proteins in a cell (Uhlén *et al.*, 2015; Juszkiewicz and Hegde, 2018). These proteins mature through processes occurring in the ER, including cleavage of signal sequences, folding, disulfide bond formation, and glycosylation. Then, the proteins are selectively transported to the endomembrane system, plasma membrane, or exterior of the cell (Ellgaard and Helenius, 2003; Bukau *et al.*, 2006; Ni and Lee, 2007). However, external stresses and genetic mutations can lead to the accumulation of unfolded proteins in the ER, causing ER storage diseases (e.g., hereditary emphysema) (Callea *et al.*, 1992; Rutishauser and Spiess, 2002; Hebert and Molinari, 2007). In the liver of an alpha1-antitripsin deficiency patient, amorphous semi-electron dense materials inside the dilated ER were observed, suggested that accumulation of unfolded proteins in the ER causes histological functional disorder (Owen *et al.*, 1983; Callea and Desmet, 2021). Unfolded proteins accumulated in the ER are recognized by unfolded protein response (UPR) receptors (IRE1, PERK, and ATF6), which induce molecular chaperones to re-fold or degrade the proteins through ER-associated degradation (ERAD); this is known as the ER stress response pathway (Chakrabarti *et al.*, 2011; Ruggiano *et al.*, 2014; Hetz *et al.*, 2020). However, not all misfolded proteins in the ER are degraded through ERAD (Houck *et al.*, 2014; De Leonibus *et al.*, 2019).

Macroautophagy (hereinafter referred to as autophagy) is a bulk degradation system in which an isolation membrane engulfs a portion of the cytoplasm and delivers it to lysosomes for degradation (Mizushima and Komatsu, 2011; Mercer *et al.*, 2018; Melia *et al.*, 2020; Klionsky *et al.*, 2021). Recent studies have revealed that large cellular structures, such as organelles (Lemasters, 2005; Singh *et al.*, 2009; Maejima *et al.*, 2013), ribosomes (Kraft *et al.*, 2008), protein aggregates (Webb *et al.*, 2003; Øverbye *et al.*, 2007), invading pathogens (Nakagawa *et al.*, 2004), lysosomes (Maejima *et al.*, 2013) and protein droplets (Wilfling *et al.*, 2020; Yamasaki *et al.*, 2020), are selectively degraded via autophagy. This selectivity is achieved through autophagy receptors, which link cargos to the autophagosomal membrane. The interaction motifs between autophagy receptors and autophagy-related gene (ATG) proteins are evolutionarily conserved, as several proteins contain the microtubule-associated protein light chain 3 (LC3)-interacting region (LIR). The LIR contributes to selective interaction with cargos, which are recruited to the autophagosomal membrane (Stolz *et al.*, 2014). The FIP200-interacting region (FIR) is another binding motif that links cargos to FIP200, a component of the ULK1 complex that is indispensable to autophagy induction (Smith *et al.*, 2018; Turco *et al.*, 2019). ER-phagy (reticulophagy) is a type of autophagy that can selectively remove the ER (DE DUVE, 1963; Bernales *et al.*, 2006) and maintains ER homeostasis through remodeling of ER conformation via the degradation of excessive membrane or removal of unfolded luminal proteins (Jia *et al.*, 2011; Pengo *et al.*, 2013; Molinari, 2021). Several proteasome-resistant ER proteins, such as ATZ variant of alpha1-antitrypsin (Teckman and Perlmutter, 2000; Marciniak *et al.*, 2016), the E90K mutant of GnRHR (Houck *et al.*, 2014), can be a cargo for ER-phagy. The observation of dilated ER and enhanced expression of UPR genes in autophagy-deficient cells also supported those hypotheses (Pengo *et al.*, 2013).

Since the identification of yeast ATG39 and ATG40, as well as mammalian FAM134B, as ER-phagy receptors (Khaminets *et al.*, 2015; Mochida *et al.*, 2015), several additional ER-phagy receptor proteins have been identified, including SEC62 (Fumagalli *et al.*, 2016), RTN3L (Grumati *et al.*, 2017), cell cycle progression 1 (CCPG1) (Smith *et al.*, 2018), TEX264 (An *et al.*, 2019; Chino *et al.*, 2019), ATL3 (Chen *et al.*, 2019), CALCOCO1 (Nthiga *et al.*, 2020), C53 (Stephani *et al.*, 2020), Epr1 (Zhao *et al.*, 2020), and RHD3 (Sun *et al.*, 2022). All ER-phagy receptors tether the ER membrane to the autophagosomal membrane through interaction with Atg8/LC3 (Mochida and Nakatogawa, 2022). CCPG1 also interacts with FIP200 (Smith *et al.*, 2018). Each receptor is responsive to diverse intracellular stresses. The reticulon-like proteins ATG40 and FAM134B have short hairpin transmembrane domains and generate membrane curvature, leading to fragmentation of the ER and incorporation into the autophagosome under starvation conditions (Bhaskara *et al.*, 2019; Jiang *et al.*, 2020; Mochida *et al.*, 2020). SEC62 causes ER degradation during recovery from ER stress (Fumagalli *et al.*, 2016), while CCPG1 promotes peripheral ER degradation during ER stress (Smith *et al.*, 2018). TEX264 ensures the canonical degradation of the ER via ER-phagy and is regulated by phosphorylation of its LIR (Chino *et al.*, 2019; Chino *et al.*, 2022). SEC62, CCPG1, and TEX264 all have one or two transmembrane domains, and only CCPG1 has a long intraluminal domain.

In mammals, ER-phagy receptors, which have different tissue distribution, are associated with various functional disorders. FAM134B (long-form) expresses ubiquitously, however relatively higher in the brain and in peripheral neurons, while its splicing variant, FAM134B-2 (short-form) expresses more higher in liver, kidney, spleen, and white adipose tissues(Chino *et al.*, 2019; Kohno *et al.*, 2019; Keles *et al.*, 2020). The relationship between severe functional disorders(e.g., neuropathy) and loss-of-function mutations of FAM134B has been reported (Kurth *et al.*, 2009; Murphy *et al.*, 2012). Ubiquitously expressed SEC62 is also involved in the co-translational insertion of premature proteins toward the ER, and mutations of SEC62 are reported in various disorders including not only vital organs but also cancers (Linxweiler *et al.*, 2017). RTN3 was suggested to associate with Alzheimer's disease, since the deficiency of RTN3 accelerate amyloid deposition in Alzheimer's model mouse (Shi *et al.*, 2014; Zou *et al.*, 2018). CCPG1 is abundant in the pancreas, stomach, kidney and liver (Smith *et al.*, 2018; Chino *et al.*, 2019). At present, any of pathogenic disorders corelate with CCPG1 have been identified. Since insoluble protein aggregates accumulate inside the ER due to artificial pancreas-specific suppression of CCPG1, it has been speculated that CCPG1 contributes to the suppression of protein aggregation. (Smith *et al.*, 2018). Given the differences of tissue distribution and physiological phenotype among the ER-phagy receptors, it is indicated that ER-phagy receptors maintain tissue homeostasis in each appropriate tissues.

In the UPR pathway, luminal domains of UPR receptors on the ER membrane sense unfolded luminal proteins in the ER and activate UPR signaling (Schröder and Kaufman, 2005). Although bulk incorporation of the ER into autophagosomes via ER-phagy receptors has been studied thoroughly, the process of selective protein recognition inside the ER during ER-phagy remains largely unexplored. Recent studies have revealed that several ER-resident proteins link ER-luminal cargos to ER-phagy receptors. Calnexin and binding immunoglobulin protein (BiP) are ER chaperones that deliver misfolded proteins to the ERAD machinery and also interact with FAM134B to mediate ER-phagy for misfolded procollagen (Fregno *et al.*, 2018; Forrester *et al.*, 2019). PGRMC1, which is a binding partner of ER-phagy receptor RTN3L, captures low-molecular-weight misfolded proteins (Chen *et al.*, 2021). However, whether any of these ER-phagy receptors can directly recognize ER luminal proteins for selective ER-phagy remains unclear.

In this study, I characterized an ER luminal protein, six-repeated islet amyloid polypeptide (6xIAPP), as a model ER-phagy substrate in mammalian cells and found that aggregated 6xIAPP is efficiently degraded by ATG protein- and CCPG1-dependent ER-phagy processes. I found that the luminal region of CCPG1 is essential for ER-phagic degradation of selective proteins and identified prolyl 3-hydroxylase family member 4 (P3H4) as an endogenous ER luminal protein recognized by CCPG1. CCPG1 possesses several highly conserved regions among vertebrates, and 6xIAPP and P3H4 directly interact with different parts of the luminal CCPG1 domains, which contain cargo interaction regions (CIRs). Thus, my data revealed that CCPG1 luminal regions directly recognize ER luminal cargos for ER-phagy, and simultaneous binding of multiple cargos to CCPG1 might drive the efficient removal of aberrant ER-resident proteins.

RESULTS

6xIAPP-RFP-GFP-KDEL is delivered to the lysosomes

Islet amyloid polypeptide (IAPP) is a 37-amino acid (aa) protein secreted from pancreatic islet β-cells, and aggregation of IAPP is associated with type 2 diabetes (Klöppel *et al.*, 1985; Butler *et al.*, 2003). As 6xIAPP forms oligomers and induces severe ER stress in yeast (Kayatekin *et al.*, 2018), I examined whether 6xIAPP is degraded through ER-phagy in mammalian cells. To monitor lysosomal degradation of IAPP, 6xIAPP or 1xIAPP was fused with red fluorescent protein (RFP), green fluorescent protein (GFP) and an ER retention signal, KDEL (forming IAPP-RFP-GFP-KDEL, hereafter referred to as IAPP-RG), and inserted into a lentivirus vector under a doxycycline (Dox)-dependent promoter (Figure 1). In mammalian cells, 6xIAPP-RG showed reticular and dot-like localization patterns, and increased molecular mass, compared with 1xIAPP-RG, which was similar in size to the 4.3-MDa ribosome complex (60S ribosome protein L19; RPL19) (Figure 2). Glycosylation can be an indicator of proteins translocated into the ER lumen. Because IAPP-RG does not have any glycosylation sites, its electrophoretic mobility was not altered by treatment with endoglycosidase H (Endo H) (Figure 3). Therefore, I artificially inserted an opsin glycosylation site in the C-terminus of each IAPP construct (IAPP-Gly-HA-KDEL and IAPP-RG-Gly-KDEL). These proteins (both 1x and 6xIAPP) underwent glycosylation in mammalian cells (Figure 4, and 5). Membrane permeabilization assays also showed that, while cytosol-facing RFP-GFP-cytochrome b5 (RG-Cytb5; a transmembrane domain of cytochrome b5 fused with RFP-GFP) was readily stained with anti-GFP antibody after digitonin treatment, whereas 6xIAPP-RG was stained only after cells had been treated with the stronger detergent Triton X-100 but not digitonin (Figure

6). These results suggest that 6xIAPP in mammalian cells primarily resides in the ER luminal environment at steady state.

When IAPP-RG is delivered to the lysosomes, the acidic conditions and lysosomal proteases rapidly attenuates GFP fluorescence. In contrast, RFP, which is relatively resistant to the lysosomal environment, accumulates within the lysosomes (Katayama *et al.*, 2008). Therefore, an increase in the RFP signal of lysosomes detected through fluorescence microscopy, elevation of the RFP/GFP ratio based on flow cytometry, and detection of cleaved RFP through immunoblotting can be interpreted as representing lysosomal degradation of IAPP-RG.

1xIAPP-RG was clearly co-localized with translocon-associated protein subunit alpha (TRAPα), which is an ER marker (Figure 7), but not with lysosomal-associated membrane protein 1 (LAMP1), which is a lysosome marker (Figure 8). On the other hand, although 6xIAPP-RG showed a reticular pattern and numerous dot structures colocalized with the TRAPα signal, GFP-negative and RFP-positive signals of 6xIAPP-RG accumulated in LAMP1-positive lysosomes, and RFP signals associated with lysosomes remained after Dox removal (Figure 7, and 8). Accumulation of REP-positive and GFP-negative signals were also observed in other cell lines (A549, H1299, HT1080, U2OS and Min6) derived from diverse tissues (Figure 9), which suggested that lysosomal degradation of 6xIAPP-RG is a universal response. For note, fluorescence loss in photobleaching (FLIP) assay showed that 6xIAPP-RG had relatively lower fluidity compared to 1xIAPP-RG in HeLa cell (Figure 10). I next quantified the reduction in fluorescence after Dox removal through flow cytometry. Although 1xIAPP-RG was stable, 6xIAPP-RG was rapidly degraded within 24 h of Dox removal (Figure 11). Notably, the RFP/GFP ratio of 6xIAPP-RG was efficiently increased to 2.5-fold greater than that of 1xIAPP-RG, and this increase was clearly suppressed by the lysosomal inhibitor bafilomycin A_1 (Figure 11). Treatment with bafilomycin A_1 enlarged lysosomes and caused the accumulation of GFP and RFP signals of 6xIAPP-RG, but not 1xIAPP-RG, inside lysosomes (Figure 12).

I attempted to examine whether 6xIAPP-RG without KDEL is degraded by lysosome. However, 6xIAPP-RG without KDEL was not detected in cell lysates (Figure 13). The inhibition of ER to Golgi transport by brefeldin A caused the accumulation of 1xIAPP-RG without KDEL, but not of 6xIAPP-RG without KDEL, suggesting that 6xIAPP-RG without KDEL is unstable in the ER (probably mediated by proteasomal degradation). Another problem is that if I was to use 6xIAPP without KDEL, it would be challenging to distinguish lysosomal degradation via ER-phagy from ER–Golgi transport. Thus, I used 6xIAPP-RG with KDEL in the ER-phagy experiments.

I confirmed that 6xIAPP-HA-KDEL (6xIAPP-HA), in which HA was used instead of RFP-GFP, also accumulated upon bafilomycin A_1 treatment; these findings suggested that lysosomal degradation of 6xIAPP is not mediated by the RFP-GFP tag (Figure 14). Moreover, both 6xIAPP-RG and 6xIAPP-HA accumulated inside lysosomes after the inactivation of lysosomal proteases using a lysosome inhibitor cocktail that contained E64d, pepstatin A, and leupeptin (Figure 15). Flow cytometric analysis also demonstrated a significant reduction in the RFP signal for 6xIAPP-RG. A previous report revealed that 6xIAPP on the ER is degraded by the proteasome in yeast (Kayatekin *et al.*, 2018). Indeed, treatment not only with bafilomycin A_1, but also with the proteasomal inhibitor bortezomib, led to 6xIAPP-RG accumulation in the insoluble fraction (Figure 16). Importantly, while bafilomycin A_1 clearly inhibited the generation of cleaved RFP, bortezomib neither reduced nor increased the amount of cleaved RFP derived from

6xIAPP-RG (Figure 16), indicating that the proteasome system is not associated with lysosomal degradation under these conditions. The 6xIAPP accumulated due to proteasome inhibition is likely located in the cytosol, where it cannot be removed through ER-phagy. I found that both GFP and RFP signals in cells expressing low 6xIAPP-RG levels were diminished after Dox removal. In contrast, only the GFP signal was markedly reduced in cells highly expressing 6xIAPP-RG (Figure 17). Although most of the 6xIAPP that accumulated under proteasome inhibitor treatment was not glycosylated, some glycosylated 6xIAPP accumulated under lysosomal inhibitor (Figure 18). These results indicate that 6xIAPP exists in two distinct populations in mammalian cells, undergoing to lysosomal and proteasomal degradation, respectively. Cells highly expressing 6xIAPP-RG were used to detect lysosomal degradation in subsequent experiments.

6xIAPP in the ER is degraded by ER-phagy

GFP dot structures of 6xIAPP-RG, but not 1xIAPP-RG, were colocalized with LC3, an autophagosome marker (Figure 19). To verify whether 6xIAPP is degraded by autophagy, HeLa cells expressing 6xIAPP-RG with core autophagy genes knocked out, i.e., FIP200 (Hara *et al.*, 2008), ATG5 (Mizushima *et al.*, 2001) or ATG9A (Saitoh *et al.*, 2009), were generated using clustered regularly interspaced short palindromic repeats (CRISPR). Quantitative analysis via flow cytometry revealed that the reduction of GFP signals of 6xIAPP-RG after Dox removal was significantly suppressed in the autophagy-KO cells (Figure 20). Furthermore, FIP200-KO cells showed diminished co-localization of 6xIAPP-RG with LC3 and fewer RFP dots with LAMP1-positive structures (Figure 21). These data suggest that 6xIAPP is degraded in an autophagy-dependent manner.

I observed that the number of endogenous LC3 dots was increased when

6xIAPP-RG was expressed (Figure 19). To quantify autophagic activity, 1x or 6xIAPP-HA under the Tet-On promoter was introduced into HeLa cells stably expressing RFP-GFP-LC3, as a ratiometric autophagy probe (Kimura *et al.*, 2007). With the expression of 6xIAPP-HA, but not 1xIAPP-HA, the RFP/GFP ratio of RFP-GFP-LC3 was elevated 2.7-fold and increased number of GFP punctate structures were observed within 48 h of Dox induction (Figure 22, and 23). In addition, the amount of endogenous LC3-II increased with expression of the 6xIAPP construct (Figure 24). These data suggest that autophagic activity is promoted by the expression of 6xIAPP.

If ER-phagy degraded 6xIAPP present in the ER lumen, 6xIAPP should be degraded along with ER membrane components. Therefore, I detected the lysosomal degradation of an ER component using RG-Cytb5, which localizes RFP-GFP on the ER (Figure 25). RG-Cytb5 was stably localized to the ER in HeLa cells, and treatment with Torin 1, an inhibitor of mammalian target of rapamycin complex 1 (mTORC1), induced GFP-negative and RFP-positive dots (Figure 26). The expression of 6xIAPP-HA increased the number of GFP-negative and RFP-positive dots. While tunicamycin, an ER stressor, moderately increased the amount of cleaved RFP, Torin 1 and 6xIAPP-HA induced marked accumulation of cleaved RFP (Figure 27), suggesting that 6xIAPP is eliminated by ER-phagy alongside ER components.

CCPG1 is the essential ER-phagy receptor associated with the degradation of 6×IAPP

To investigate whether autophagic degradation of 6xIAPP requires ER-phagy receptor proteins, such as FAM134B, SEC62, RTN3, CCPG1, and TEX264, immunoprecipitation (IP) of 1xIAPP-RG and 6xIAPP-RG was performed. While no ER-phagy receptor was precipitated in the presence of 1xIAPP-RG, 6xIAPP-RG co-precipitated with endogenous CCPG1 (Figure 28). I observed that the amount of endogenous CCPG1, but not the amount of other ER-phagy receptors, was increased upon expression of 6xIAPP-RG (Figure 28). The increase in CCPG1 was further augmented by bafilomycin A_1 treatment (Figure 29). Consistent with the previous finding that ER stressors (e.g., tunicamycin and thapsigargin) transcriptionally activate the expression of CCPG1 (Smith *et al.*, 2018), 6xIAPP-RG increased the mRNA abundance of CCPG1 (Figure 30), suggesting that aggregated ER-luminal proteins induce CCPG1 expression. Since it was speculated that the accumulation of 6xIAPP-RG inside the ER might induce ER stress in mammalian cells, as it has been reported in yeast (Kayatekin *et al.*, 2018). Therefore, I evaluated activation of UPR against 6xIAPP, and found the known UPR pathway is unlikely to be a major factor in the transcriptional induction of CCPG1 upon 6xIAPP-RG expression (data not shown). Additionally, FIP200-KO cells accumulated CCPG1, which also interacts with 6xIAPP. These results were consistent with the finding that CCPG1-KO cells, but not other ER-phagy receptor-KO cells, suppressed the reduction in GFP fluorescence of 6xIAPP-RG, as measured using flow cytometry (Figure 31). The autophagic degradation of 6xIAPP-RG was restored by exogenous expression of HA-CCPG1 (Figure 32, and 33), suggesting that the KO phenotype is not an off-target effect of CRISPR. I also showed that 6xIAPP formed large complexes (Figure 2) and endogenous CCPG1 migrated to high-density fractions, which have similar molecular mass to 6xIAPP (Figure 34). These results indicate that CCPG1 plays an essential role in ER-phagy-dependent degradation of 6xIAPP aggregates.

CCPG1 is a vertebrate-specific gene and regulates ER-phagy via cytoplasmic N-terminal LIR and FIRs (Smith *et al.*, 2018). Notably, among ER-phagy receptors, only

CCPG1 has a large ER luminal region, which consists of > 500 aa (Kostenko *et al.*, 2006). However, the physiological function of this luminal domain remains unclear. Therefore, I hypothesized that the ER luminal region of CCPG1 is associated with the recognition of ER luminal cargos. The CCPG1Δ289–757 mutant lacking the whole ER luminal region (CCPG1 luminal-deletion) failed to restore the RFP/GFP ratio of 6xIAPP in CCPG1-KO cells (Figure 33). CCPG1-KO cells showed fewer GFP-negative and RFP-positive dots for 6xIAPP-RG; these were recovered through re-expression of full-length CCPG1, but not CCPG1 luminal-deletion (Figure 35). I then performed an RFP cleavage assay, which demonstrated that re-expression of full-length CCPG1 restored lysosomal degradation of 6xIAPP-RG (Figure 36). On the other hand, re-expression of CCPG1 luminal-deletion had only a moderate effect on CCPG1-KO, likely due to bulk ER-phagy via the cytoplasmic domain of CCPG1. These results indicate that the luminal region of CCPG1 is required for ER-phagy-dependent lysosome degradation of 6xIAPP.

Overexpression of CCPG1 leads to the formation of punctate structures on the ER, which reportedly co-localize with ATG proteins in mammalian cells (Smith *et al.*, 2018). Although the luminal-deletion mutant of CCPG1 co-localized with LC3, the rate of puncta formation was reduced (Figure 37). On the other hand, the mutant of both LIR and FIRs, which was an interaction-deficient mutant for LC3 and FIP200, showed complete abolishment of co-localization of CCPG1 with LC3, instead accumulating as large amorphous structures under ER stress conditions. However, no accumulation of CCPG1 was observed when both the luminal domain and ATG protein-interaction motifs were deleted (Figure 37). These data suggest that the localization of CCPG1 to autophagosomes is dependent on LIR and FIRs, but not the luminal domain. In addition, luminal domain-dependent formation of aggregate-like structures by CCPG1 may result from interactions with mis-folded proteins in the ER.

P3H4 is an endogenous substrate for CCPG1-dependent ER-phagy

To identify endogenous substrates for CCPG1-dependent ER-phagy, I searched for proteins that interacted with CCPG1 in a luminal domain-dependent manner. I performed IP using FLAG-CCPG1 and its mutants, as described below, and subjected the immunoprecipitates to mass spectrometry (MS) analysis. MS screening 1 used FLAG-CCPG1 full-length and FLAG-CCPG1 luminal domain-deletion as a negative control, and MS screening 2 used FLAG-CCPG1 cytosolic domain-deletion (Figure 38). The resultant immunoprecipitants were analyzed through liquid chromatography with tandem mass spectrometry (LC-MS/MS; Figure 38). I identified numerous ER luminal proteins, including ER chaperones, ERAD components, glycosidases, and enzymes for collagen maturation. Among these proteins, I focused on P3H4, which was identified in both MS screens and has not yet been studied in the context of autophagy. P3H4 is an ER-resident protein belonging to the Leprecan (leucine proline-enriched proteoglycans) family (Ochs *et al.*, 1996; Gruenwald *et al.*, 2014) and forms a complex with prolyl 3-hydroxylase to regulate lysine hydroxylation of collagen (Heard *et al.*, 2016). P3H4 exhibited CCPG1-luminal domain-dependent interaction with CCPG1 (Figure 39). To monitor pulse-chased lysosomal degradation of P3H4, I employed a HaloTag based cleavage assay for P3H4 (HaloTag becomes resistant to lysosomal degradation after ligand binding) (Yim *et al.*, 2022). HeLa cells stably expressing ssHalo-P3H4 were transfected with siRNA against CCPG1. After 3 days, the cells were exposed to tetramethylrhodamine-conjugated ligand for 1 h and then incubated for 24 h. Generation of the Halo cleavage band was significantly impaired in CCPG1-depleted cells (Figure 40). Cleavage of reporters was restored through re-expression of CCPG1, but not the luminal-domain deletion mutant or LIR/FIR mutants (Figure 40). These data suggest that P3H4 is degraded by CCPG1 in a luminal domain- and autophagy-dependent manner. Notably, endogenous P3H4 accumulated markedly in the pancreas, stomach, heart, and muscle of adult brain-rescued ATG5-KO mice (Yoshii *et al.*, 2016) (Figure 41), suggesting that some tissues constitutively degrade P3H4 via ER-phagy. Considering that CCPG1 is also highly expressed in exocrine tissues such as the pancreas and stomach (Chino *et al.*, 2019), these results suggest that CCPG1 has a functional relationship with P3H4. P3H4 also accumulated in CCPG1-KO or bafilomycin A_1-treated HeLa cells (Figure 42). Additionally, overexpression of HA-CCPG1 reduced the amount of P3H4. These data indicate that P3H4 is an endogenous substrate for CCPG1-dependent ER-phagy.

Highly conserved ER-luminal regions of CCPG1 contain functional domains

As the ER-luminal region of CCPG1 is essential for ER-phagy-mediated degradation of 6xIAPP and P3H4, I apportioned the luminal region into conserved regions through sequence alignment among vertebrates. Although the length of the CCPG1 sequence varied among species by up to 120 aa, the ER luminal region of CCPG1 contained four highly conserved regions (region A: aa 288–401, region B: aa 411–457, region C: aa 482–550, region D: aa 621–734) (Figure 43). I presumed that regions A–D of CCPG1 include the cargo interacting region (CIR) and generate C-terminal-truncated mutants (Δ742–757, Δ621–757, Δ551–757, Δ411–757, and Δ289–757) (Figure 44). First, I measured bulk ER-phagy activity using ssRFP-GFP-KDEL, an ER-luminal fluorescence reporter for ER-phagy (Chino *et al.*, 2019), and found that overexpression of the full-length sequence or any truncated mutant in CCPG1-KO cells promoted lysosomal degradation of ssRFP-

GFP-KDEL (Figure 45), suggesting that the cytosolic region (containing LIR and FIRs) and transmembrane domain of CCPG1 are sufficient for the induction of bulk ER-phagy. The cleavage of ssRFP-GFP-KDEL by some truncated mutants, including Δ551–757 and Δ411–757, compared to full-length CCPG1 was more efficient probably due to the high expression level. From these results, enhancement of bulk-ER-phagy activity caused by overexpression of the CCPG1 luminal-deletion mutant might result in partial recovery of lysosomal degradation of 6xIAPP (Figure 36). In contrast, lysosomal degradation of 6xIAPP-RG was not rescued through overexpression of the Δ411–757 and Δ289–757 mutants of CCPG1 in CCPG1-KO cells (Figure 46, and 47), indicating that highly conserved regions within 411–551 aa, including regions B and C, might recognize 6xIAPP for degradation via ER-phagy. I defined the highly conserved regions B–D as CIR 1–3 (Figure 48).

To characterize these CIRs, I generated CIR1-, CIR2- and dual CIR1- and CIR2-truncated mutants, and analyzed the associated lysosomal degradation of 6xIAPP-RG. Contrary to my expectations, lysosomal degradation of 6xIAPP-RG was rescued by all CIR1- and CIR2-related mutants (Figure 49, and 50). Therefore, I hypothesized that region D, defined as CIR3, may contribute to 6xIAPP degradation along with CIR1, CIR2, or both. I found that truncated CCPG1 with both CIR1 and CIR3 deleted was unable to restore the lysosomal degradation of 6xIAPP-RG (Figure 49, and 50). Alternatively, bulk ER-phagy activity detected using ssRFP-GFP-KDEL was restored with overexpression of the any CIR-related mutants of CCPG1 (Figure 51). These results demonstrate that the ER luminal region of CCPG1 contains functional domains, i.e., CIRs, required for the selective degradation of 6xIAPP.

I conducted similar experiments using another cargo, P3H4. CCPG1 mutants lacking CIR2 did not rescue the lysosomal degradation of RG-P3H4 (Figure 52). Furthermore, CCPG1ΔCIR2 no longer co-localized to the dot-like structures observed for RG-P3H4, in contrast to the full-length sequence and other mutants of CCPG1 (Figure 53). These findings suggest that P3H4 undergoes CIR2-dependent ER-phagy degradation, and that CCPG1 contains multiple cargo recognition sequences in the ER luminal region.

CIR1 directly interacts with IAPP, while CIR2 interacts with P3H4.

Next, I verified whether CCPG1 directly interacts with P3H4 and 6xIAPP. All recombinant proteins containing the full length of the ER luminal region, each CIR region alone (CIRs 1–3), CIR1+3 of CCPG1, P3H4, and 6xIAPP combined with small tags (ALFA, HA, and FLAG) (Götzke *et al.*, 2019), and dihydrofolate reductase (DHFR) for stabilization (Iwakura *et al.*, 1992) were synthesized in vitro using a cell-free protein synthesis system (Shimizu *et al.*, 2001; Shimizu *et al.*, 2005). Expression levels were estimated through immunoblotting, and the synthesized proteins were mixed at a 1:3 volume ratio (antigen: binding partner) in lysis buffer for IP using specific antibodies. 6xIAPP efficiently interacted with the entire C-terminal region (241–757) of CCPG1 (Figure 54). Although HA-6xIAPP did not co-precipitate with CIR2 and CIR3 alone, it did co-precipitate with CIR1 alone, and with CIR1+CIR3. In contrast, the entire C-terminal region and CIR2 alone co-immunoprecipitated by HA-P3H4 (Figure 55). These observations suggest that the CIRs of CCPG1 directly interact with ER luminal cargos, and that different CIRs contribute to the recognition of different cargos.

The ER luminal region of CCPG1 simultaneously recognizes multiple cargos.

As 6xIAPP and P3H4 directly interacted with different CIRs of CCPG1, I hypothesized that a single molecule of CCPG1 could simultaneously interact with 6xIAPP and P3H4. Therefore, I checked for competitive inhibition using excess levels of the same recombinant proteins with different tags synthesized using a cell-free protein translation system. The presence of excess FLAG-P3H4 inhibited co-IP of HA-P3H4 with ALFA-CCPG1 (full-length of C-terminal) (Figure 56), while the addition of excess DHFR-FLAG had no effect on that interaction. Similarly, co-IP of HA-6xIAPP by ALFA-CCPG1 was inhibited by excess FLAG-6xIAPP (Figure 57), indicating that interaction of the cargo with CCPG1 can compete with the same excess cargos under in-vitro conditions.

Then, I confirmed competitive inhibition of 6xIAPP and P3H4 against CCPG1. Recombinant AFLA-CCPG1 was mixed with HA-P3H4 or FLAG-6xIAPP, or both, and then immunoprecipitated using anti-ALFA antibody beads. The presence of P3H4 had no inhibitory effect on binding between 6xAIPP and CCPG1; similarly, 6xAIPP did not inhibit the binding of CCPG1 to P3H4 (Figure 58). This result suggests that a single CCPG1 molecule interacts with multiple cargos simultaneously.

DISCUSSIOUN

In this study, I found that CCPG1 directly interacts with ER luminal proteins via CIRs, which recognize different types of cargo (Figure 59). CCPG1 is a receptor not only for LC3 and FIP200, but also for ER luminal proteins (via its long ER luminal region). Therefore, my findings provide new insights, indicating that CCPG1 is a bispecific receptor for ER luminal cargos and the autophagic membrane; it drives selective ER-phagy and the cargo selectivity thereof, thereby promoting efficient degradation of particular cargos through ER-phagy.

6xIAPP promotes primary nucleation and increases proteotoxicity (Kayatekin *et al.*, 2018). Excessive expression of 6xIAPP in yeast clogs the translocon, which is then removed through proteasomal degradation via Ste24. Upon ZMPSTE24, a mammalian homolog of yeast Ste24 inhibition by Lopinavir, 6xIAPP proteotoxicity also decreased cell viability in mammalian pancreatic cells (Kayatekin *et al.*, 2018). Since Lopinavir was reported to inhibit autophagic-lysosomal degradation (Zha *et al.*, 2013), expression of 6xIAPP and lysosomal activity are suggested to be closely related to cytotoxicity. I employed 6xIAPP fused with several different tags (fluorescent proteins or HA-tag) and the KDEL signal as a model ER-phagy substrate. Moreover I found that 6xIAPP is primarily translocated within the ER at a steady state in mammalian cells, as verified by the analysis of N-glycosylation using a construct fused with the glycosylation site from opsin (Figure 4, and 5). Aggregated 6xIAPP was primarily degraded through autophagy under the investigated conditions (Figure 19−21). On the other hand, proteasome inhibition led to the accumulation of 6xIAPP, which was detected in the insoluble fraction without glycosylation (Figure 18); this indicated that 6xIAPP was mis-localized to the cytoplasm because of stress-induced inhibition of protein translocation (Kang *et al.*, 2006) or was dislocated from the clogged ER translocon by ZMPSTE24 (Ast *et al.*, 2016; Kayatekin *et al.*, 2018). These results demonstrate that 6xIAPP in mammals does not always clog the translocon, but some proportion may be successfully translocated into the ER, where aggregated 6xIAPP is targeted for ER-phagy. Analysis of cells expressing low and high levels of 6xIAPP indicated a difference in dependence (Figure 17). Low expression levels of 6xIAPP were mainly degraded through a non-lysosomal pathway. On the other hand, highly expressed 6xIAPP was largely degraded through the lysosomal pathway (Figure 17). I speculated that 6xIAPP aggregated in the ER is an ERAD-inefficient substrate, similar to aggregated procollagen (Ishida *et al.*, 2009). 6xIAPP formed large oligomers under my conditions (Figure 2). The conformation of aggregated 6xIAPP at high concentrations in the ER might lead to its recognition by CCPG1.

I observed that the overexpression of 6xIAPP alone is sufficient to induce autophagy (Figure 19, 22−24), likely because the increased abundance of CCPG1 is directly recognized by both FIP200 and LC3 (Figure 28, and 29). This finding is supported by a previous report that overexpression of WT CCPG1, but not mutant LIR or FIR, promotes ER-phagy (Smith *et al.*, 2018). This raises the question of how 6xIAPP induces CCPG1 expression. ER stress induces CCPG1 expression (Smith *et al.*, 2018). Moreover, the UPR factors PERK, XBP1, and MIST1 are associated with CCPG1 transcription (Tian *et al.*, 2010; Adamson *et al.*, 2016). However, I did not detect activation of the UPR pathway by 6xIAPP overexpression in HeLa cells, although ER-phagy was induced. In addition, I confirmed that 6xIAPP-RG was degraded in cell lines from diverse tissues (Figure 9). Since not all the tissues from which these cell lines are derived express CCPG1, it is speculated that the expression of CCPG1 had elevated with canceration. Alternatively, different pathways could be substituted for the transportation of 6xIAPP-RG toward the lysosomes.

Future work is needed to identify the specific transcription factor(s) responsible for CCPG1 induction by 6xIAPP. Identification of the pathways that regulate CCPG1 expression and establishment of regulatory methods will contribute to the therapeutic treatment expecting for removing the aggregate proteins observed in ER storage disease. Conversely, as previous reports discussed, functional inhibition of CCPG1 could enhances ER stress to eliminate malignant cells in several cancers.

Another open question is how CCPG1 induces autophagy. I initially assumed that a luminal cargo transduces a signal from the ER lumen to the cytoplasmic side to induce ER-phagy, similar to the induction of the UPR; if this is the case, cargo binding to CCPG1 might trigger ER-phagy. However, overexpression of a CCPG1 mutant lacking the whole ER luminal region induced autophagy (Figure 45). Therefore, the expression of CCPG1, which recruits FIP200 and LC3 to the ER membrane, might be sufficient to initiate ER-phagy, even without an ER luminal cargo. Although this mechanism may not be elegant, it is very straightforward, and CCPG1-dependent ER-phagy does not require any additional signal transduction pathways.

As CCPG1 has the largest ER luminal domain among known ER-phagy receptors, it has been speculated that CCPG1 recognizes ER luminal proteins (Smith and Wilkinson, 2017; Grumati *et al.*, 2018; Smith *et al.*, 2018; Wilkinson, 2020). I revealed that CCPG1 directly interacts with cargos, including 6xIAPP and P3H4. P3H4 was reported to play a role in catalyzing the complex hydroxylation process of collagen chains. Physiologically, P3H4 is a prognostic factor for lung adenocarcinoma and bladder cancer (Li *et al.*, 2018; Jin *et al.*, 2021); it contributes to cancer invasion and growth (Hao *et al.*, 2020), suggesting that CCPG1 may have a protective effect against these cancers. In addition, endogenous P3H4 accumulated in the pancreas and stomach of autophagy-deficient mice (Figure 41), suggested that it undergoes degradation dependent on the autophagy-lysosome pathway, particularly in exocrine organs.

Several ER chaperones, including BiP, calnexin, PDIA1, PDIA3, CALR, and TXNDC5, were identified by MS analysis of proteins binding to the luminal region of CCPG1 (Figure 38). This is consistent with a previous finding that ER chaperones, including PDIA6, accumulated in the pancreas of CCPG1 hypomorphic mice (Smith *et al.*, 2018). As FAM134B has been reported to bind to BiP and calnexin, which mediates the capture of luminal misfolded proteins under ER stress conditions (Fregno *et al.*, 2018; Forrester *et al.*, 2019; Chipurupalli *et al.*, 2022), CCPG1 may employ a similar mechanism, in which ER chaperones mediate the degradation of luminal proteins through ER-phagy. CCPG1 is an ER-stress-responsive gene, suggesting that ER-phagy may share common substrates with ERAD, and that cross-talk may exist, depending on the amount of degradation. In this scenario, although ER-phagy exhibits more extensive selective recognition of unfolded proteins, its substrate selectivity might be similar to the UPR, such that direct recognition of a substrate by the luminal region of CCPG1 may contribute to ER-phagy-specific selectivity.

Homology searches were performed with the Position-Specific Iterative Basic Local Alignment Search Tool (PSI-BLAST) using human sequences of CIRs from CCPG1; however, I detected no proteins containing similar domains. Moreover, further searches using the InterPro database (v90.0) (Blum *et al.*, 2021) identified no paralogs or proteins with conserved CIR-related regions. In addition, no similarity among CIRs in CCPG1 was found through sequence alignment. The AlphaFold tool predicted that CIRs

1–3 have different structures (Jumper *et al.*, 2021; Varadi *et al.*, 2022), and my data indicated different cargo selectively among these CIRs; this indicated that each CIR recognizes the cargo using different machinery.

The three-dimensional structure of CCPG1 has not demonstrated yet. Moreover, many regions of CCPG1 were predicted as intrinsically disordered regions (IDRs) by structure prediction programs, such as Alphafold2, trRosetta (Yang *et al.*, 2020) and PSIPRED (McGuffin *et al.*, 2000). The flexibility of the steric structure recalls the instability of CCPG1, while it may contribute to the acquisition of diverse cargo selectivity. Since CCPG1 contains LIR and FIR in its cytoplasmic region and induces ER-phagy, which in turn induces the degradation of ER components including CCPG1 itself, it is inferred that its half-life is relatively short. Therefore, I speculated that rather than ensuring the structural stability, the structural flexibility to recognize a wider range of cargos may have been conserved.

Future work is needed to identify the specific motifs or transient and specific regional structures that bind ER-phagy substrates and reveal the detailed mechanisms of substrate selectivity.

MATERIALS AND METHODS

Antibodies

Rabbit polyclonal anti-LAMP1 antibodies were a gift from Y. Tanaka (Kyusyu University). Rabbit polyclonal anti-TRAPα antibodies were gifted by R.S. Hegde (MRC LMB). Mouse monoclonal anti-HA (clone 16B12, 901502) was purchased from BioLegend Funakoshi (Tokyo, Japan). Mouse monoclonal anti-RFP (M204-3) and anti-LC3 (M152-3) antibodies, and rabbit polyclonal anti-LC3 (PM036), anti-p62 (PM045) and anti-ATG9A (PD042MS) antibodies were purchased from MBL (Tokyo, Japan). Mouse monoclonal anti-β-actin (281-98721), anti-GFP (clone mFX75, 012-22541) and anti-FLAG (018-22381) antibodies were purchased from Wako (Osaka, Japan). Mouse monoclonal anti-RPL19 (WH0006143M1), anti-β-actin (A2228) and anti-FLAG (F4042) antibodies were purchased from Sigma-Aldrich (St. Louis, MO, USA). Mouse monoclonal anti-HSP90 (610419) antibodies were purchased from BD Biosciences (Tokyo, Japan). Mouse monoclonal anti-Halo (G9211) antibody was purchased from Promega (Madison, WI, USA). Rabbit polyclonal anti-FAM134B (21537-1-AP), anti-RTN3 (12055-2-AP), anti-CCPG1 (13861-1-AP), anti-TEX264 (25858-1-AP), anti-RB1CC1 (FIP200) (17250-1-AP), anti-ATG5 (10181-2-AP), anti-Histone-H3 (17168-1-AP) and anti-ATF6 (24169-1-AP) antibodies were purchased from Proteintech (Tokyo, Japan). Rabbit polyclonal anti-SEC62 (NBP1-84045) antibodies were purchased from Novus biologicals (Centennial, CO, USA). Rabbit polyclonal anti-P3H4 (A13754) antibodies were purchased from ABclonal (Woburn, MA, USA). Rabbit polyclonal anti-ALFA antibodies were raised in rabbits through immunization with the ALFA peptide (Eurofins). GFP-nanobody and ALFA tag-nanobody Sepharose were generated through conjugation of GFP-nanobody protein purified from pOPINE GFP nanobody (plasmid #49172; Addgene, Watertown, MA, USA) and ALFA tag-nanobody protein (Götzke *et al.*, 2019) purified from pRSET-A ALFA–His to N-hydroxy succinimide-activated Sepharose 4 Fast Flow (GE Healthcare, Chicago, IL, USA). Mouse monoclonal anti-FLAG M2 affinity gel (A2220) and anti-FLAG M2 magnetic beads (M8823) were purchased from Sigma-Aldrich. Mouse monoclonal anti-HA conjugated Sepharose (014-23081) was purchased from Wako.

Plasmids

To generate pCW_1x (or 6x) IAPP-RFP-GFP-KDEL or 1x (or 6x) IAPP-RFP-GFP, IAPP-related constructs, human IAPP and 6xIAPP sequences (synthesized using gBlocks Gene Fragments; Integrated DNA Technologies; Coralville, IA, USA) were inserted into the pCW57.1 vector (plasmid #41393; Addgene) along with DNA encoding the mCherry, super-folder GFP (sfGFP) and, if indicated, KDEL sequences. For pCW_1x (or 6x) IAPP-HA-KDEL, each IAPP sequence and 3× hemagglutinin (HA)-tag was used. pCW_1x (or 6x) IAPP-Gly-HA-KDEL was generated through insertion of the N-glycosylation site from opsin (Pedrazzini *et al.*, 2000) into pCW_1x (or 6x) IAPP-HA-KDEL. To generate pCW ssRFP-GFP-KDEL, the signal sequence of prolactin and the mCherry, super-folder GFP and KDEL sequences were subcloned into the pCW57.1 vector. For pCW ssRFP-GFP-P3H4, cDNA of human P3H4 amplified from total cDNA of HEK293T cells was used. To generate full-length or truncated CCPG1 constructs, cDNA of CCPG1s was amplified from HEK293FT total cDNA and inserted into the pLenti cytomegalovirus vector GFP Puro (plasmid #17448; Addgene) or pMRX-IB (Morita *et al.*, 2018); these plasmids were generated from pMXs

(Kitamura *et al.*, 2003) along with enhanced GFP, 3xFLAG-tag or 3xHA-tag. Truncated constructs were prepared through PCR-mediated site-directed mutagenesis. To generate pMRXIB_RFP-GFP-LC3 and pMRXIB_RFP-GFP-Cytb5, cDNA of rat LC3 and the transmembrane domain of Cytb5 was amplified from pMXs-IP-EGFP-LC3 (plasmid #38195; Addgene) and pMXs-puro GFP-b5 ER (plasmid #38274; Addgene) and inserted into the pMRX-IB vector. For the ATG- or ER-phagy receptor gene-targeted CRISPR vector, the specific sgRNA sequences were inserted into lentiCRISPR v2 hygro (plasmid #98291; Addgene) or lentiGuide-puro (plasmid #52963; Addgene). For plasmids with a cell-free protein synthesis system in vitro, DHFR (amplified from PURExpress DHFR), 3xHA-tag, 3xFLAG-tag, ALFA-tag, P3H4, and the indicated regions of CCPG1 (amplified from total cDNA of HEK293FT) were inserted into a PURExpress plasmid (provided with the PURE system kit from New England Biolabs, Ipswich, MA, USA). pCMV-VSVG (plasmid #8454; Addgene) and psPAX2 (plasmid #12260; Addgene) were used for lentivirus production. pCMV-VSVG and Gag were used for retrovirus production.

Cell Culture

HeLa, HEK293FT, U2OS, H1299, A549 and MIN6 cells were cultured in Dulbecco's modified Eagle's medium (Nacalai Tesque, Kyoto. Japan) supplemented with 10% fetal bovine serum (FBS; MP Biomedicals, Santa, Ana, CA, UK) and 50 mg/ml penicillin and streptomycin (regular medium) in a 5% CO_2 incubator.Tetracycline-On (Tet-On) cells were generated through lentiviral transduction with a pCW57.1 vector containing the single-vector Tet-On component.

For compound treatment, cells were incubated at the indicated times with 0.2 μM bafilomycin A_1 (LC Laboratories, Woburn, MA, USA), 1 µM Torin 1 (Tocris Bioscience, Ellisville, MO, USA), 2 µg/ml tunicamycin (Sigma-Aldrich, 0.2 µM thapsigargin (Santa Cruz Biotechnology, Dallas, TX, USA), 10 µg/ml E64d (Peptide Institute, Osaka, Japan), 100 µM pepstatin A (Peptide Institute), 20 µg/ml leupeptin (Peptide Institute), 50 µg/ml brefeldin A (Wako) or 1 µg/ml Dox (Clontech, Mountain View, CA, USA).

Generation of a KO cell line using CRISPR/Cas9 gene editing (mixed population of WT and KO cells)

SgRNA sequences for KO cells were designed using CHOPCHOP [FIP200 (5′ - GGCTGCAATCATGGCCAACC -3′): Atg5 (5′ - AAGAGTAAGTTATTTGACGT -3′): Atg9A (5′ -AGGATATTCGAGAGAAGAAG -3′): CCPG1(5′ - ACAGTGATTCATCTTGTGGT -3′): FAM134B (5′ - ACTCTTTGGCAGCAACCGTG -3′): RTN3 (5′ - AAGAAGACTGGGTTTGTCTT -3′): SEC62 (5′ - CCACCAATATGATGGGTCAC -3′): TEX264 (5′ - GCTACTACTGGGCCTGATTG -3′)] and cloned into lentiCRISPR v2 hygro (plasmid #98291; Addgene) or lentiGuide-puro (plasmid #52963; Addgene). HeLa cells were infected with the lentivirus and then cultured for 7 days under hygromycin/puromycin selection. The hygromycin/puromycin-resistant cells were used as KO cell lines.

Generation of a clonal KO cell line using CRISPR/Cas9 gene editing

To generate clonal HeLa CCPG1 KO cells, HeLa cells were transfected with pSpCas9(BB)-2A-Puro (PX459) V2.0 (plasmid #62988; Addgene) containing the sgRNA sequence of CCPG1. Puromycin was transiently applied for 24 h post-transfection. After culturing for > 5 days, single cell clones were isolated through dilution into 96-well plates and screened for successful KO of CCPG1 through immunoblotting.

Generation of stable cell lines through lentiviral and retroviral infection

Stable cell lines were generated using lentiviral and retroviral expression systems. HEK293FT cells were transiently co-transfected with lentiviral or retroviral vectors using PEI MAX regent (Polysciences, Warrington, PA, USA). After culturing for 72 h, the growth medium containing the virus was centrifuged, and the resulting supernatant was collected. HeLa cells were incubated with this virus-containing medium for 48 h and then selected with 1 μg/ml puromycin (InvivoGen, San Diego, CA, USA), 5 μg/ml blasticidin S (Wako), 100 μg/ml hygromycin B (Wako), or 500 μg/ml G418 (Nacalai Tesque).

Immunoblotting

Cells were washed with cold phosphate-buffered saline (PBS) and lysed in lysis buffer (1% Triton X-100, 50 mM Tris-HCl pH 7.5, 1 mM ethylenediaminetetraacetic acid [EDTA], and 150 mM NaCl) supplemented with protease inhibitor cocktail (EDTA-free; Nacalai Tesque) and 1 mM phenylmethanesulfonyl fluoride for the collection of soluble fractions, or 1xSDS sample buffer (0.0625 mM Tris-HCl pH 6.8, 2% SDS,10% 2-mercaptoethanol, and 10% glycerol) for the collection of whole cell lysates, for 15 min at 4°C. The soluble lysates were clarified through centrifugation at 20,630 × *g* for 5 min, and 6× sodium dodecyl sulfate (SDS) sample buffer was added. The samples were heated to 95°C for 5 min prior to SDS/polyacrylamide gel electrophoresis (SDS/PAGE), in which 20 μg of protein per lane was separated and then transferred to a polyvinylidene disulfide membrane (Millipore, Burlington, MA, USA). Immunoblot analysis was performed with the indicated antibodies suspended in Signal Enhancer Hikari (Nacalai Tesque) and the immunoreactive proteins were visualized using ImmunoStar Zeta (Wako).

siRNA knockdown experiments

Stealth RNAi oligonucleotides were purchased from Thermo Fisher Scientific (Waltham, MA, USA). The following sequences were used: siCCPG1, 5'-UUCCAAUAUAGAUACUGUCUUCGGG -3' and siLuciferase (siLuc), 5'-AAUUAAGUCCGCUUCUAAGGUUUCC-3'. The stealth RNAi oligonucleotides were transfected into cells using Lipofectamine RNAiMAX (13778150; Thermo Fisher Scientific) according to the manufacturer's instructions.

Mice

All animal experiments were approved by the Institutional Animal Care and Use Committee of the University of Tokyo. Atg5$^{-/-}$;NSE-Atg5 mice (Yoshii *et al.*, 2016) and Fip200$^{flox/flox}$;Nestin-Cre mice (Liang *et al.*, 2010) have been described previously. To obtain post-nuclear supernatants, tissue homogenates were centrifuged at 500 × *g* for 10 min and the supernatants were boiled in sample buffer.

LC-MS/MS analysis of FLAG-CCPG1 immunoprecipitates

HeLa stably expressing FLAG-CCPG1, as well as the FLAG-CCPG1 luminal deletion mutant and FLAG and FLAG-CCPG1 cytosol deletion mutant, were incubated and lysed with lysis buffer (50 mM Tris-HCl, pH 7.5, 150 mM NaCl, 1% NP-40, and complete EDTA-free protease inhibitor [03969-21; Nacalai Tesque]). After centrifugation at 17,700 × *g* for 10 min, the supernatants were incubated with anti-FLAG M2 magnetic beads for

3 h at 4°C with gentle rotation. The eluted proteins were enzymatically digested according to a phase-transfer surfactant (PTS) protocol (Rappsilber *et al.*, 2007). Then, 50 μL of each eluted sample was mixed with 85 μL PTS buffer. Samples were reduced with 10 mM dithiothreitol at room temperature for 30 min and alkylated with 50 mM 2-iodoacetamide (804744; Sigma-Aldrich) at room temperature for 30 min. Next, samples were diluted five-fold through addition of 50 mM NH_4HCO_3 solution followed by digestion with 1 μg of lysyl endopeptidase (LysC; 121-05063; Wako) at 37°C for 4 h. Samples were further digested with 1 μg trypsin at 37°C for 8 h. An equal volume of ethyl acetate acidified with 0.5% trifluoroacetic acid (TFA) was added to the digested samples. After centrifugation twice at 10,000 × g for 10 min at room temperature, the aqueous phase containing the peptides was collected and dried using a SpeedVac concentrator (Thermo Fisher Scientific). The dried peptides were solubilized in 100 μL of 2% acetonitrile and 0.1% TFA, and the peptide mixture was trapped on a hand-made C18 STAGE tip prepared as described previously (Boersema *et al.*, 2009). The trapped peptides were subjected to a previously reported dimethyl-labeling procedure (Boersema *et al.*, 2009). Subsequently, CH_2O and $NaBH_3CN$ (light label) were added to the FLAG-only sample. Similarly, CD_2O and $NaBH_3CN$ (heavy label) were added to the FLAG-NEK9 sample. The dimethyl-labeled peptides remaining on the tip were eluted with 100 μL of 80% acetonitrile and 0.1% TFA. The light- and heavy-labeled eluates were mixed and dried using a SpeedVac concentrator. Each sample was dissolved in 2% acetonitrile and 0.1% TFA, and loaded into the LC-MS system with an Orbitrap Exploris 480 MS instrument (Thermo Fisher Scientific) equipped with a nano-high-performance liquid chromatography system (Advance UHPLC; Bruker Daltonics, Billerica, MA, USA) and HTC-Pal autosampler (CTC Analytics, Zwingen, Switzerland) with a trap column

(0.3 × 5 mm, L-column ODS; Chemicals Evaluation and Research Institute, Tokyo, Japan). Samples were separated using a gradient of mobile phases A (0.1% formic acid/H_2O) and B (0.1% formic acid and 100% acetonitrile) at a flow rate of 300 nL/min (4–32% B for 190 min, 32–95% B for 1 min, 95% B for 2 min, 95% to 4% B for 1 min, and 4% B for 6 min) with a homemade capillary column (length, 200 mm and inner diameter, 100 μm) packed with 2-μm C18 resin (L-column2; Chemicals Evaluation and Research Institute). Then, the eluted peptides were electrosprayed (2.1 kV) and introduced into the MS instrument. Data were obtained in positive ion mode for data-dependent MS/MS ($ddMS^2$) acquisition. Full MS spectra were obtained across a scan range of 350–1,800 m/z with 60,000 full width at half maximum (FWHM) resolution at 200 m/z. MS^2 spectra were obtained with 7,500 FWHM resolution at 200 m/z. For $ddMS^2$ acquisition, full MS spectra were obtained every 3 sec and MS^2 spectra were obtained during the 3 sec intervals. The most abundant precursor ions (excluding isotopes of a cluster) above the 5.0e3 intensity threshold with a charge state from 2+ to 7+ were selected using a 2.0-*m/z* isolation window. A 20-s dynamic exclusion period was applied. The raw data obtained were used for a database search (UniProt reviewed the mouse database on September 13th, 2018) with the Sequest HT algorithm running on the Proteome Discoverer 2.5 platform (Thermo Fisher Scientific). The parameters for database searches were as follows: peptide cleavage was set to trypsin; missed cleavage sites were allowed for up to two residues; peptide lengths were set to 6–144 aa; and mass tolerances were set to 10 ppm for precursor ions and 0.02 Da for fragment ions. Carbamidomethylation of cysteine and dimethylation [H(4)C(2), or D(4) C(2)] of lysin and the peptide N-terminus were set as fixed modifications. Oxidation of methionine was set as a variable modification. A significance threshold of $p < 0.05$ was applied. The abundances of precursor ions were calculated based on the area of the precursors, determined with Proteome Discoverer 2.5.

Insoluble fraction assay

Cells were lysed in lysis buffer with protease inhibitor cocktail and 1 mM phenylmethanesulfonyl fluoride for 15 min at 4°C. The lysate was clarified through centrifugation at 20,630 × *g* for 30 min. Then, the supernatant was collected as the soluble fraction, and the pellet (containing the insoluble fraction) was washed three times with fresh lysis buffer. The insoluble pellet was suspended in a volume of lysis buffer equal to the soluble fraction volume and then mixed with 6× SDS sample buffer. The samples were heated to 95°C for 5 min and then sonicated.

Glycosylation assay

Cells expressing IAPP constructs fused with the glycosylation site of opsin (Pedrazzini *et al.*, 2000) were lysed in 1× lysis buffer without protease inhibitor, incubated for 15 min on ice, and then centrifuged at 20,630 × *g* for 5 min. The supernatant of each lysate was mixed with 10× glycoprotein denaturing buffer, heated for 5 min at 95°C, and then incubated with endoglycosidase H or H_2O at 37°C for 10 h. Next, 6× SDS sample buffer was added to each product; the mixture was heated to 95°C for 5 min, and then analyzed through SDS-PAGE and immunoblotting.

Sucrose gradient fractionation

Cells were lysed in CHAPS (3-[(3-cholamidopropyl)dimethylammonio]-1-propanesulfonate) buffer containing protease inhibitor for 30 min on ice. Then, the lysates were centrifuged at 20,630 × *g* for 30 min at 4°C to remove insoluble components; the resulting supernatants were layered on top of a 10–50% discontinuous sucrose gradient and centrifuged at 259,000 × *g* for 90 min at 4°C (CS 150FNX; rotor: S55S [9124280K]; Hitachi, Tokyo, Japan). Eleven 200-μl fractions were collected and mixed with 6× SDS sample buffer, and then analyzed through SDS-PAGE and immunoblotting.

Immunofluorescence microscopy

Cells were plated on coverslips, fixed in 3.7% formaldehyde in PBS for 15 min, permeabilized with 50 μg/ml digitonin or 0.1% Triton X-100 in PBS for 5 min, and then blocked with 10% newborn bovine serum (NBS) in PBS for 45 min. After blocking, each sample was incubated with the indicated primary antibodies for 1 h. After washing, each sample was incubated with Alexa-647 conjugated anti-mouse or anti-rabbit IgG secondary antibodies (Thermo Fisher Scientific) for 1 h. The stained cells were observed under a confocal laser microscope (FV1000 IX81; Olympus, Tokyo, Japan) using a 100× oil immersion objective lens with a numerical aperture of 1.40. Images were acquired using FV10-ASW 2.1 imaging software.

Flow cytometry

Cells were trypsinized with EDTA and recovered through detachment from the dish. The cells were passed through a 70-μm cell strainer, and then resuspended in 10% FBS and 1 μg/ml 4′,6-diamidino-2-phenylindole (DAPI) in PBS for flow cytometric analysis using a CytoFLEX S flow cytometer equipped with NUV 375 nm (DAPI), 488 nm (GFP), and 561 nm (RFP) lasers (Beckman Coulter, Brea, CA, USA). Dead cells were detected through DAPI staining. In each sample, 10,000 cells were acquired and the RFP/GFP fluorescence ratio was calculated as red fluorescence intensity divided by green fluorescence intensity in RFP-positive cells. The data were processed with Kaluza software (Beckman Coulter).

Immunoprecipitation

Cells were lysed in lysis buffer with protease inhibitor cocktail and 1 mM phenylmethanesulfonyl fluoride, for 15 min at 4°C. The lysate was clarified through centrifugation at 20,630 × *g* for 5 min, and the resulting supernatant was collected. A portion of this supernatant was mixed with 6× SDS buffer, heated to 95°C for 5 min, and then used as an input. GFP-nanobody Sepharose beads were added to the mixture, which was incubated for 2 h at 4°C. The Sepharose beads were washed four times with lysis buffer prior to elution with SDS sample buffer. The samples were subsequently separated through SDS-PAGE and analyzed through immunoblotting.

In-vitro protein biding assay

Each DHFR- and small-tag-fusion protein was synthesized using PURE frex2.1 and suspended in 1× lysis buffer containing 1% Triton X-100. Substrates for IP and target proteins were mixed at a ratio of 1:3, and the Sepharose beads conjugated to specific antibodies or nano-bodies against HA, FLAG, or ALFA were incubated at 4°C for 1 h. The beads were washed four times with 1× lysis buffer and 2× SDS sample buffer was added. The mixture was then heated to 95°C for 5 min, and analyzed using SDS-PAGE and immunoblotting. For analysis of competition for the same cargos, FLAG-tagged products were added at three times the volume of HA-tagged cargos. For analysis of competition for different cargos, P3H4 and 6xIAPP were mixed at equal volumes. SDS-PAGE and immunoblotting were performed for analysis.

RNA extraction, reverse transcription and quantitative real-time PCR

Total RNA was extracted from cells using ISOGEN II (NIPPON GENE, Tokyo, Japan). Reverse transcription was performed using ReverTra Ace reverse transcription reagents (TOYOBO LIFE SCIENCE, Osaka, Japan). The following gene-specific primer sequences were used: human CCPG1, 5'-TTCTGTGACCCCCACTGACA-3' (forward) and 5'-TTGGCTGCTTTCTCCTTGCT-3' (reverse); human GAPDH, 5'-CCACATCGCTCAGACACCA-3' (forward) and 5'-GGCAACAATATCCACTTTACCAGAG-3' (reverse); human spliced-XBP1, 5’-CTGAGTCCGAATCAGGTGCAG-3’ (forward) and 5’-ATCCATGGGGAGATGTTCTGG-3’ (reverse); human HRD1, 5’-CCAGTACCTCACCGTGCTG-3’ (forward) and 5’-GCCTCTGAGCTAGGGATGC-3’ (reverse); human CHOP, 5’-AGAACCAGGAAACGGAAACAGA-3’ (forward) and 5’-TCTCCTTCATGCGCTGCTTT-3’ (reverse); human BiP, 5’-TGTTCAACCAATTATCAGCAAACTC-3’ (forward) and 5’-TTCTGCTGTATCCTCTTCACCAGT-3’ (reverse). Relative quantification of gene expression was performed according to the $2^{(-\Delta\Delta CT)}$ method. The housekeeping gene GAPDH was used as an internal control to normalize the variability in expression levels.

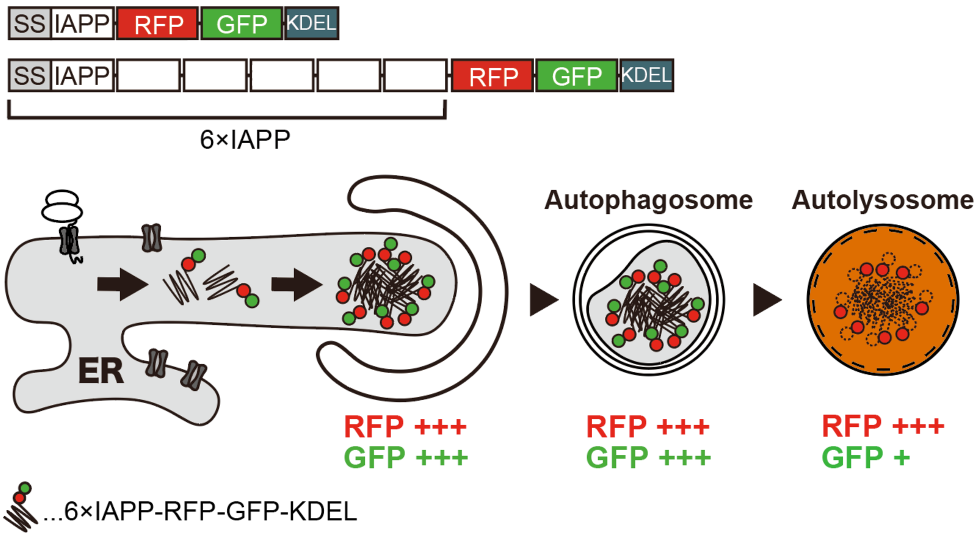

Figure 1. Schematic diagrams of the ER-phagy substrate 1x (or 6x) IAPP-RFP-GFP-KDEL (1x [or 6x] IAPP-RG).

In the lysosome, GFP fluorescence is diminished, whereas RFP fluorescence remains intact due to resistance to acidic pH and lysosomal proteases.

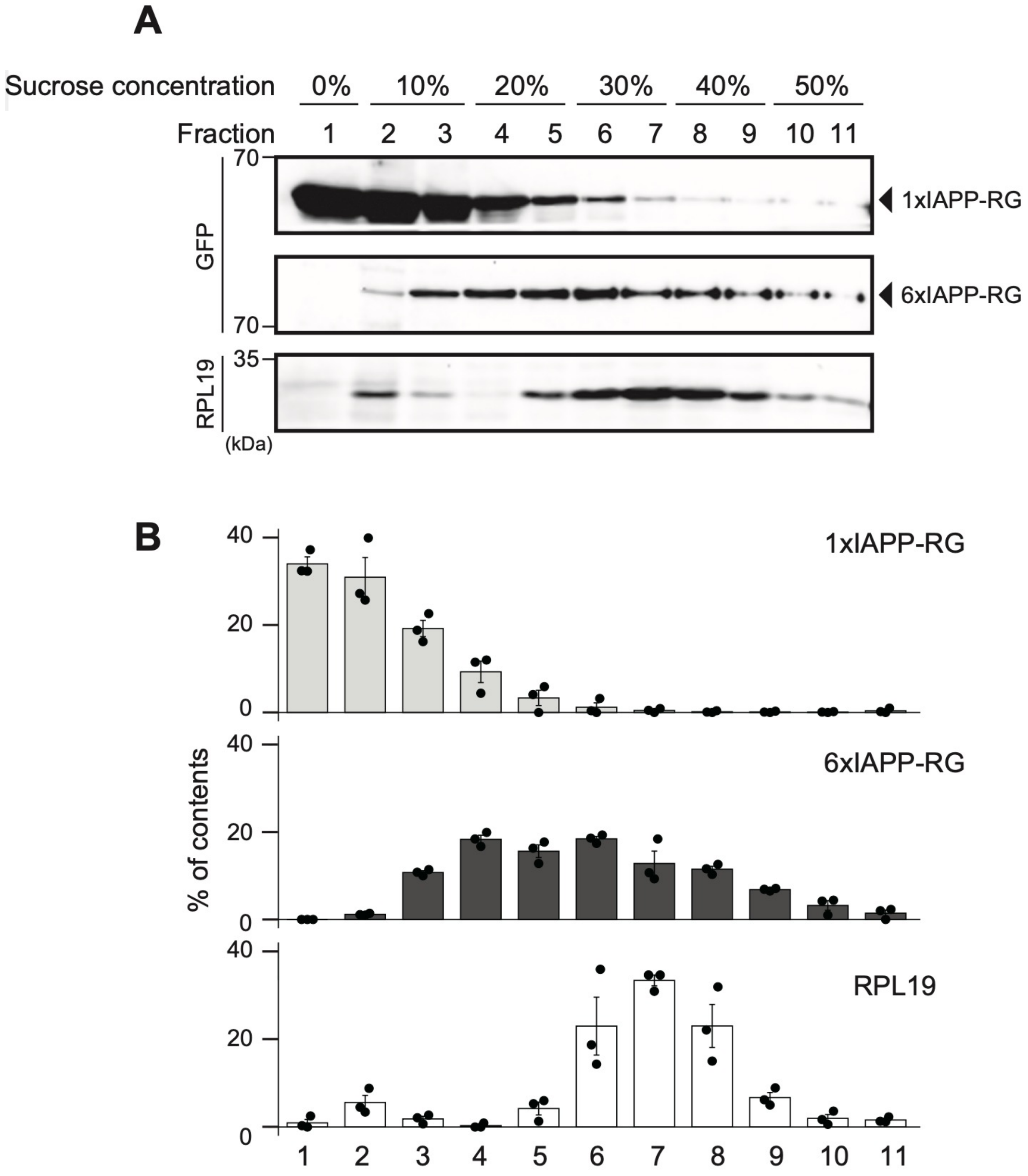

Figure 2. 6xIAPP forms large aggregates in the ER lumen.

Tet-On HeLa cells expressing 6x (or 1x) IAPP-RFP-GFP-KDEL were incubated in medium containing Dox for 48 h prior to lysis with CHAPS buffer, and the lysates were fractionated on a discontinuous 10–50% sucrose gradient. Each fraction was collected, subjected to SDS-PAGE and analyzed through immunoblotting with antibodies against GFP and RPL19 (a ribosome component) (A). Data represent the mean ± SE of three independent experiments (B).

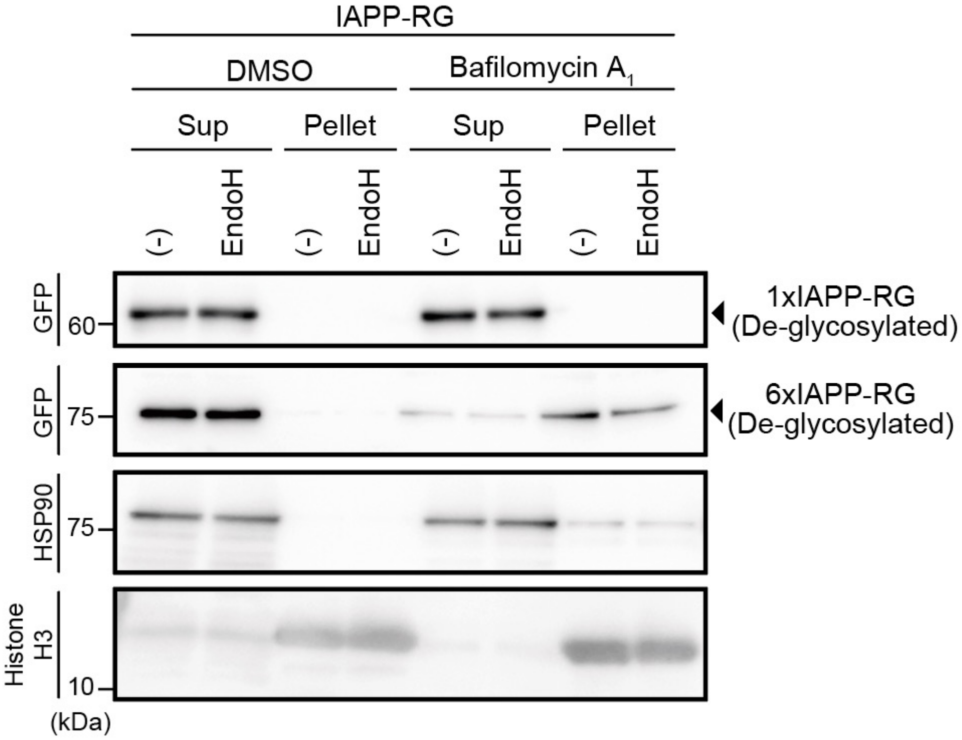

Figure 3. IAPP-RG constructs are not glycosylated.

Tet-On HeLa cells expressing 1x (or 6x) IAPP-RG were cultured in Dox-containing medium for 48 h, then treated with DMSO or Bafilomycin A_1 24 h prior to analysis. The cells were suspended in lysis buffer and centrifugated; the supernatants were then collected as the soluble fraction, whereas pellets were collected as the insoluble fraction. Each fraction was treated with H_2O or endoglycosidase H (Endo H), then analyzed through immunoblotting using antibodies against GFP, HSP90 and Histone H3.

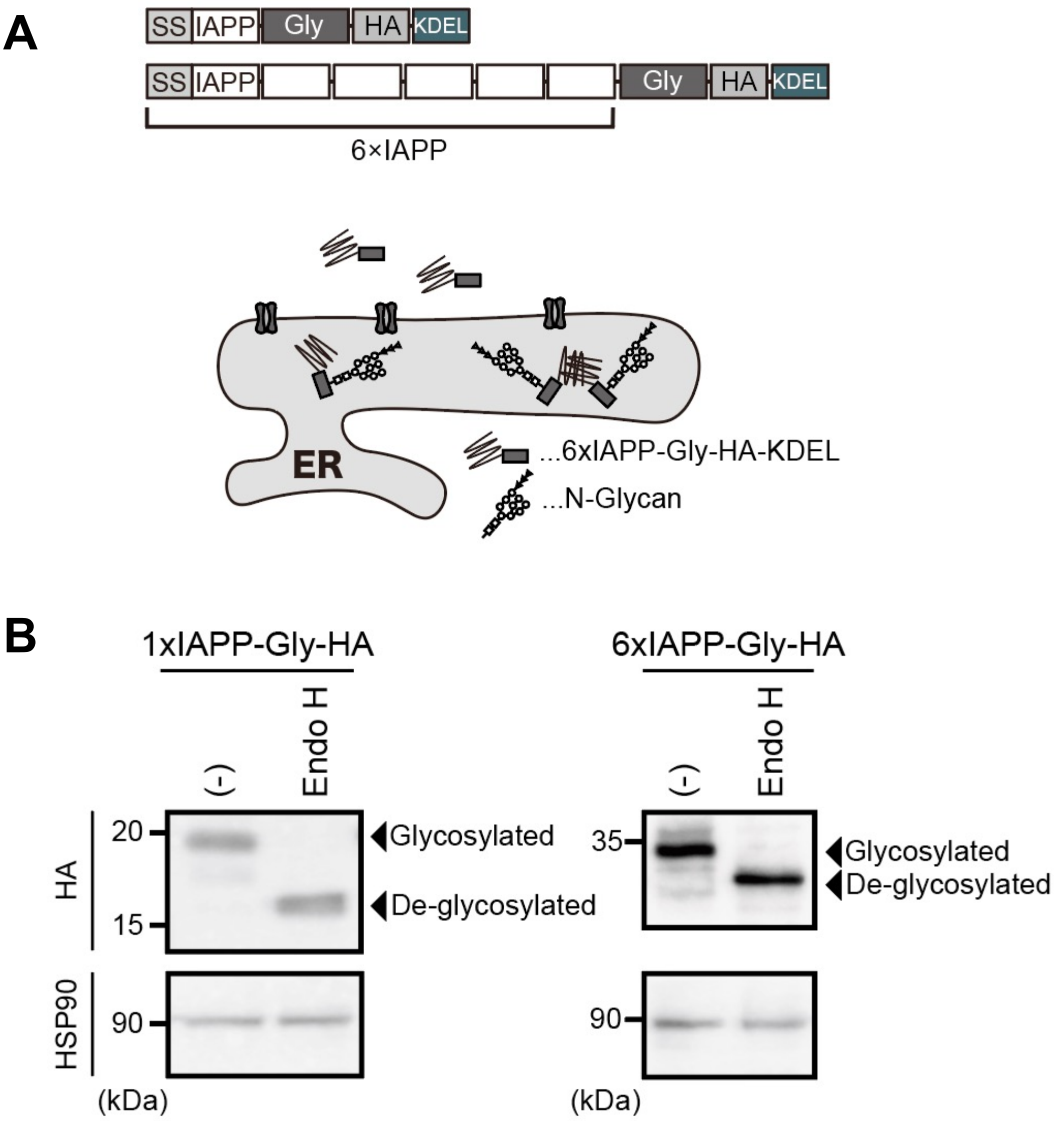

Figure 4. IAPP-Gly constructs are mainly glycosylated in the ER of mammalian cells

Schematic diagrams of the IAPP-Gly-HA-KDEL. Chimeric IAPP constructs fused with the glycosylation site of opsin would become glycosylated only when they reached and successfully matured inside the ER (A). Tet-On HeLa cells expressing 6x (or 1x) IAPP-Gly-HA-KDEL were cultured in medium containing Dox for 24 h and lysed with buffer containing 1% Triton X-100. The lysates were treated with endoglycosidase H for 18 h, and then subjected to SDS-PAGE and analyzed through immunoblotting with antibodies against HA, GFP, and HSP90. (B).

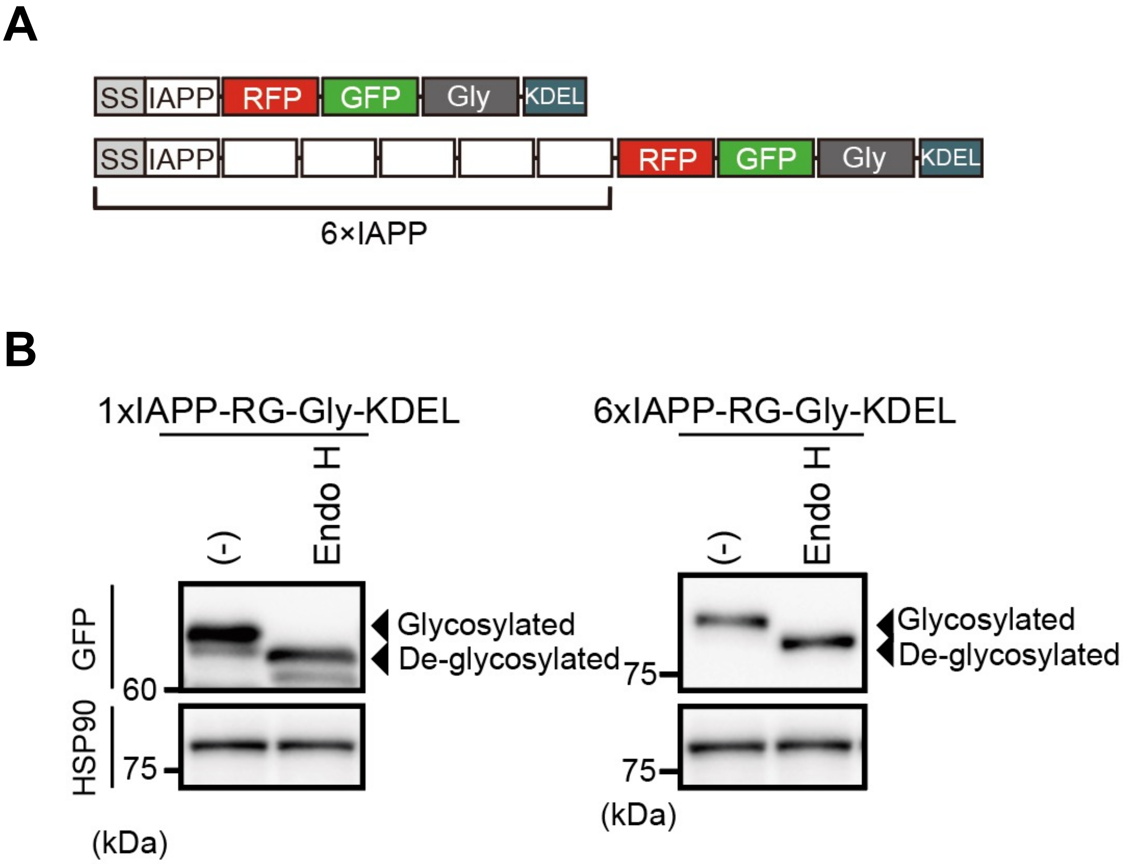

Figure 5. IAPP-Gly constructs are mainly glycosylated in the ER of mammalian cells.

Schematic diagrams of the IAPP-RG-Gly-KDEL(A). Tet-On HeLa cells expressing 1x (or 6x) IAPP-RG-Gly-KDEL and cultured in Dox-containing medium for 48 h. The lysates were treated with endoglycosidase H for 18 h, and then subjected to SDS-PAGE and analyzed through immunoblotting with antibodies against HA, GFP, and HSP90 (B).

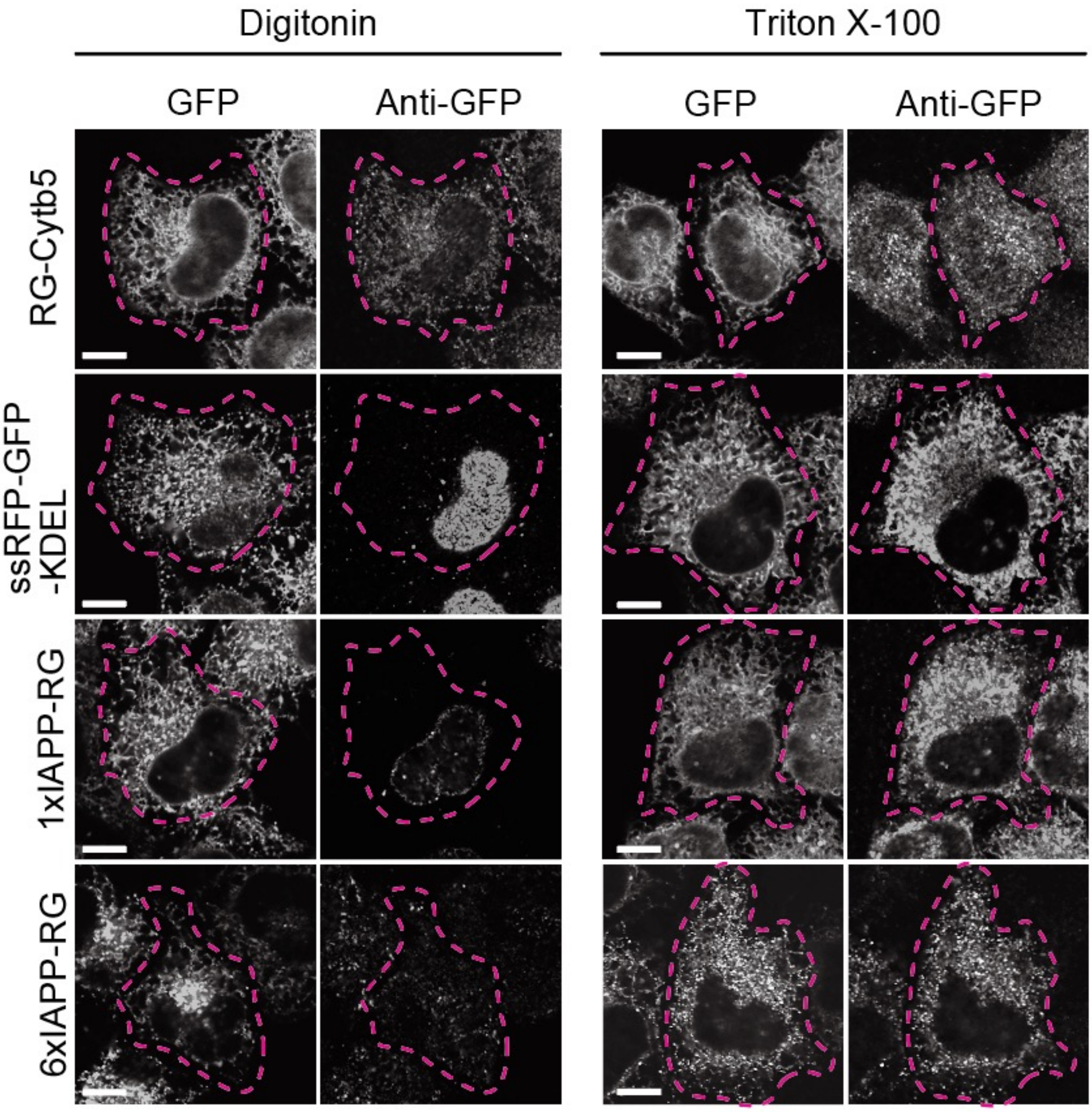

Figure 6. 1xIAPP-RG and 6xIAPP-RG are localized in Triton-sensitive membrane.

Tet-On HeLa cells expressing RG-Cytb5 (as an ER membrane marker), ssRFP-GFP-KDEL (as an ER luminal marker), or 1x (or 6x) IAPP-RG were cultured with Dox-containing medium for 48 h. After fixation, cells were treated with digitonin or Triton X-100 for permeabilization, then stained with antibodies against GFP. Scale bars represent 10 μm.

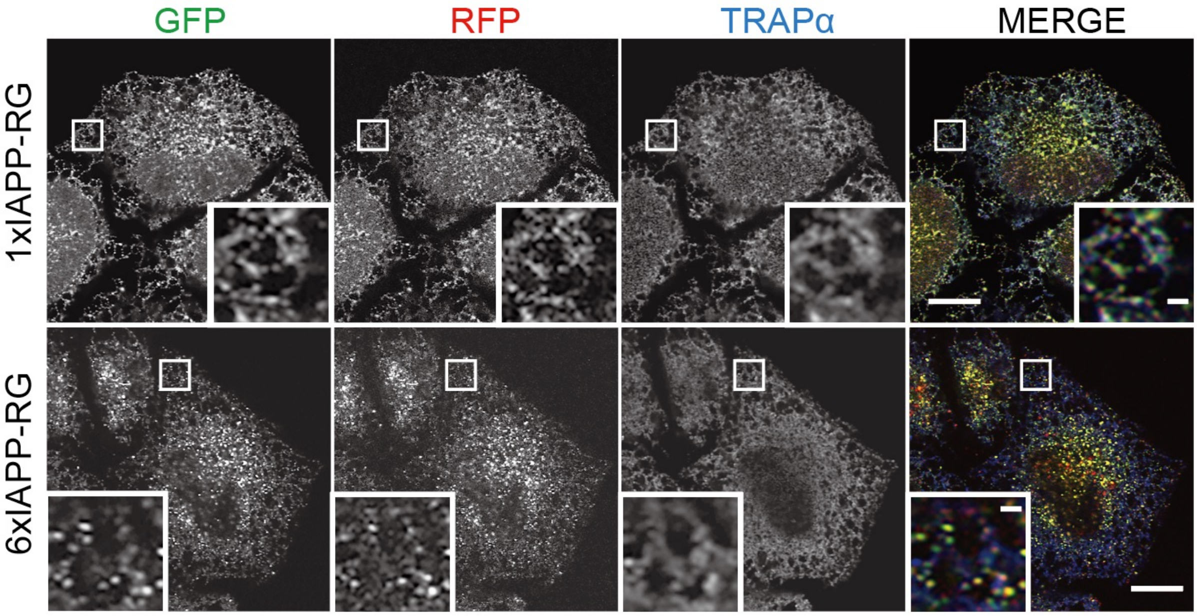

Figure 7. 1xIAPP and 6xIAPP are localized in the ER in mammalian cells.

Tet-On HeLa cells expressing 1x (or 6x) IAPP-RG were incubated in medium containing Dox for 48 h before fixation. Cells were stained with antibodies against TRAPα and analyzed through immunofluorescence microscopy. Scale bars represent 10 and 1 μm (inset).

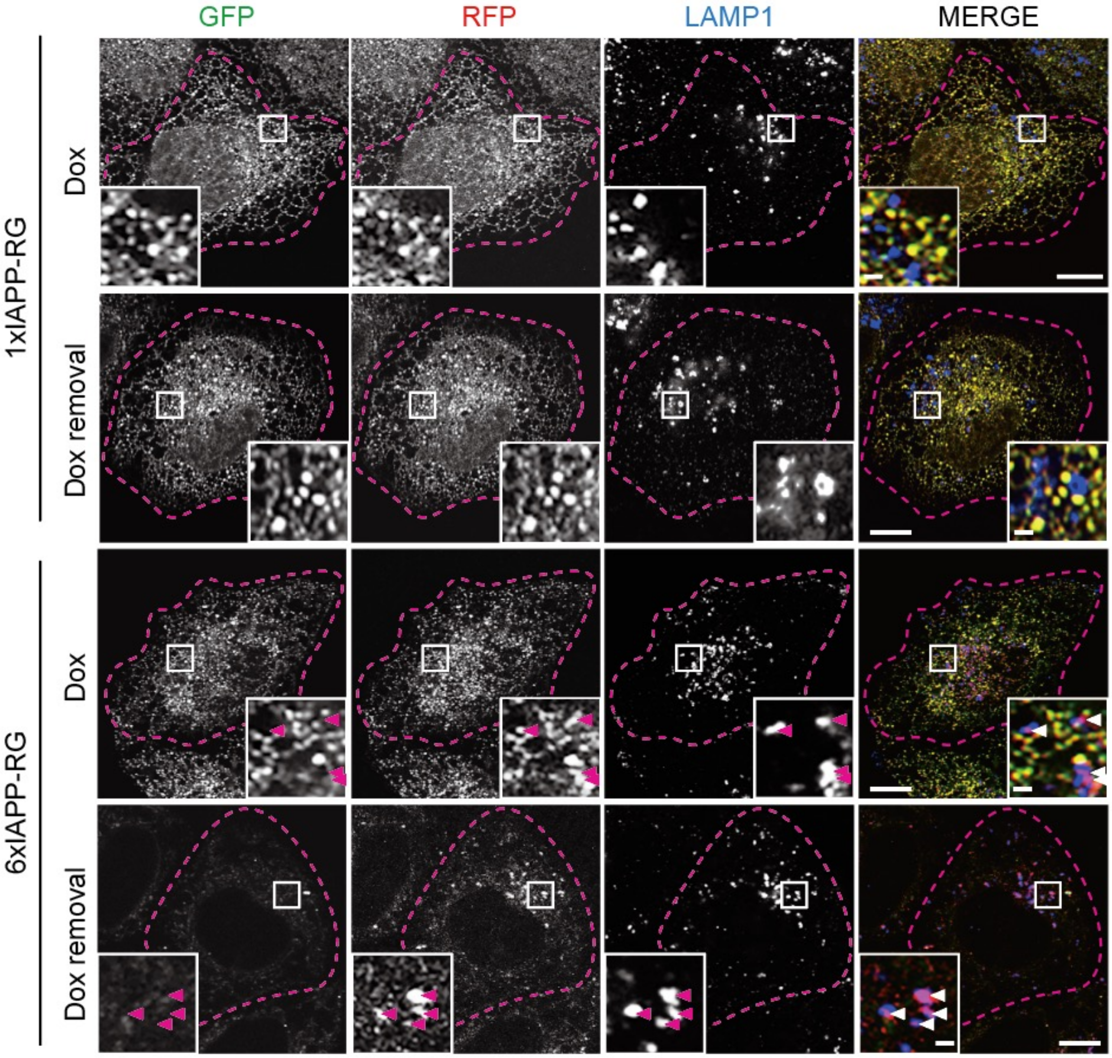

Figure 8. 6xIAPP, but not 1xIAPP, is delivered to lysosomes.

Tet-On HeLa cells expressing 6x (or 1x) IAPP-RFP-GFP-KDEL were incubated in medium containing doxycycline (Dox) for 24 h, and then cultured in medium with or without Dox for a further 24 h. After fixation, the cells were stained with antibodies against LAMP1 and analyzed by confocal microscopy. GFP-negative and RFP-positive signals accumulated in LAMP1-positive structures (arrowhead) are indicated. Scale bars represent 10 and 1 µm (inset).

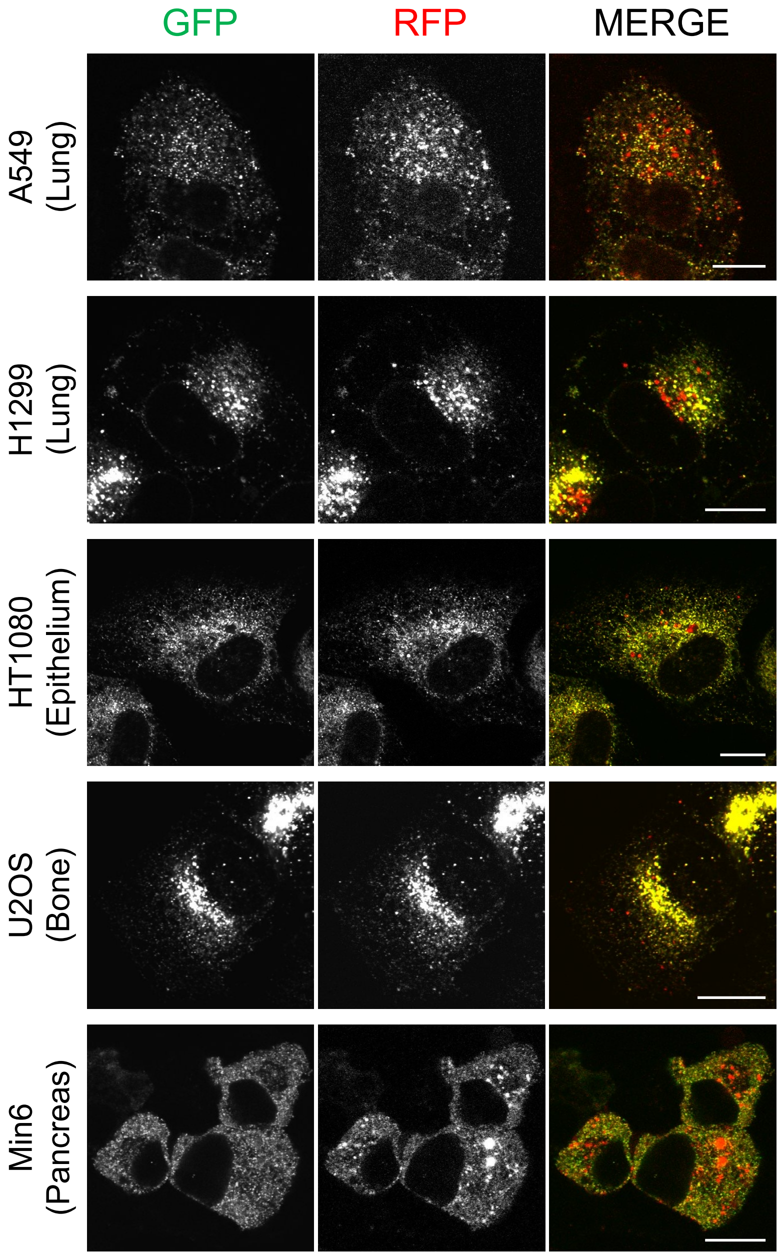

Figure 9. Lysosomal degradation of 6xIAPP-RG occurs in cell lines derived from several tissues .

Tet-On A549, H1299, HT1080, U2OS and Min6 cells expressing 6xIAPP-RG were incubated with Dox containing medium for 48 h before fixation by formaldehyde. Cells were analyzed through immunofluorescence microscopy. Scale bars represent 10 and 1 μm (inset).

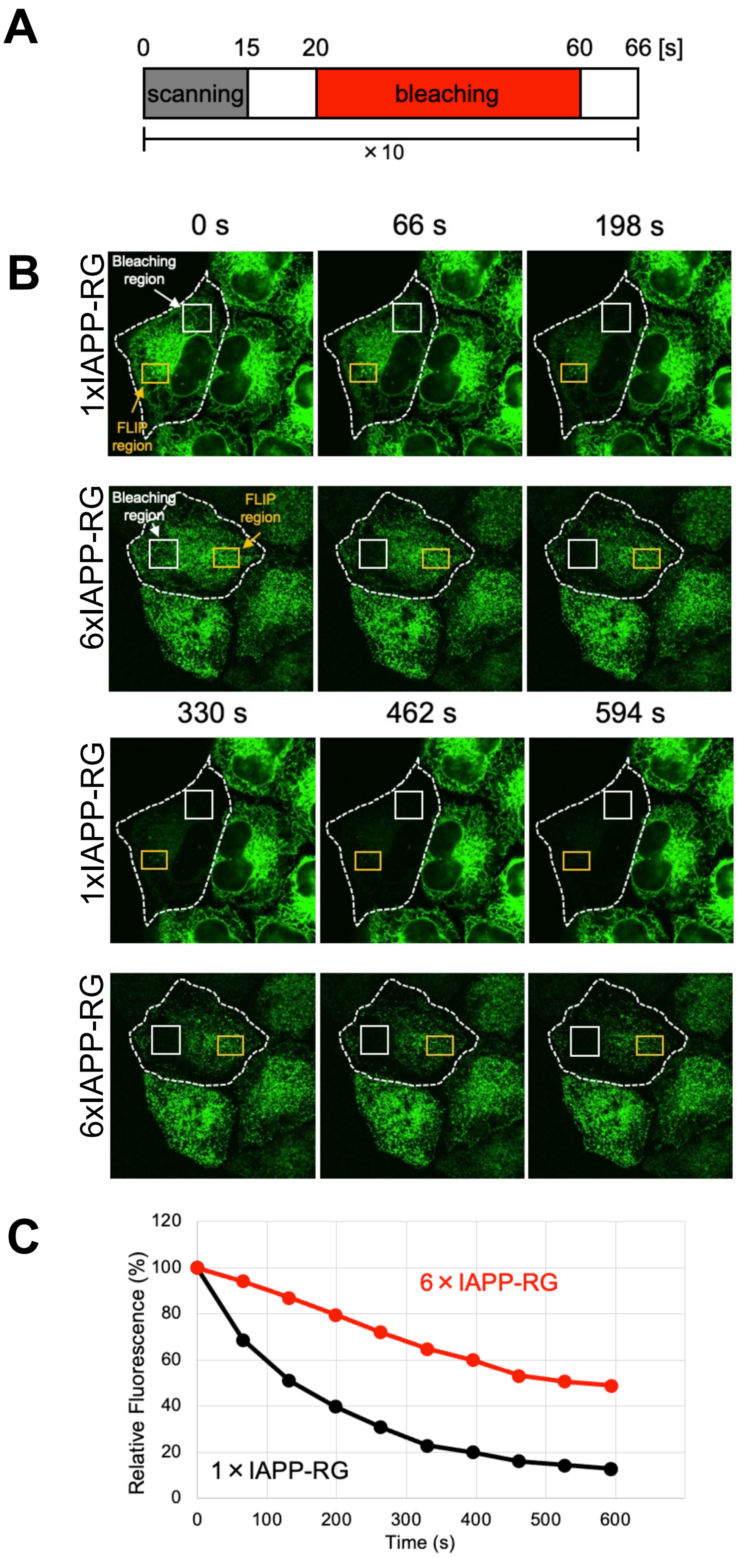

Figure 10. 6xIAPP forms large structures with low fluidity in mammalian cells.

Scanning protocol for Fluorescence loss in photobleaching (FLIP)(A).Tet-On HeLa cells expressing 1x or 6xIAPP-RG was treated with Dox for 24 h on the glass-bottom dish. Fluorescent images were taken at indicated time points. Regions for measuring fluorescence intensities (white rectangles) and bleaching (yellow rectangles) were shown.(B). Relative fluorescence intensities compared with the time 0 were calculated by using imageJ(C).

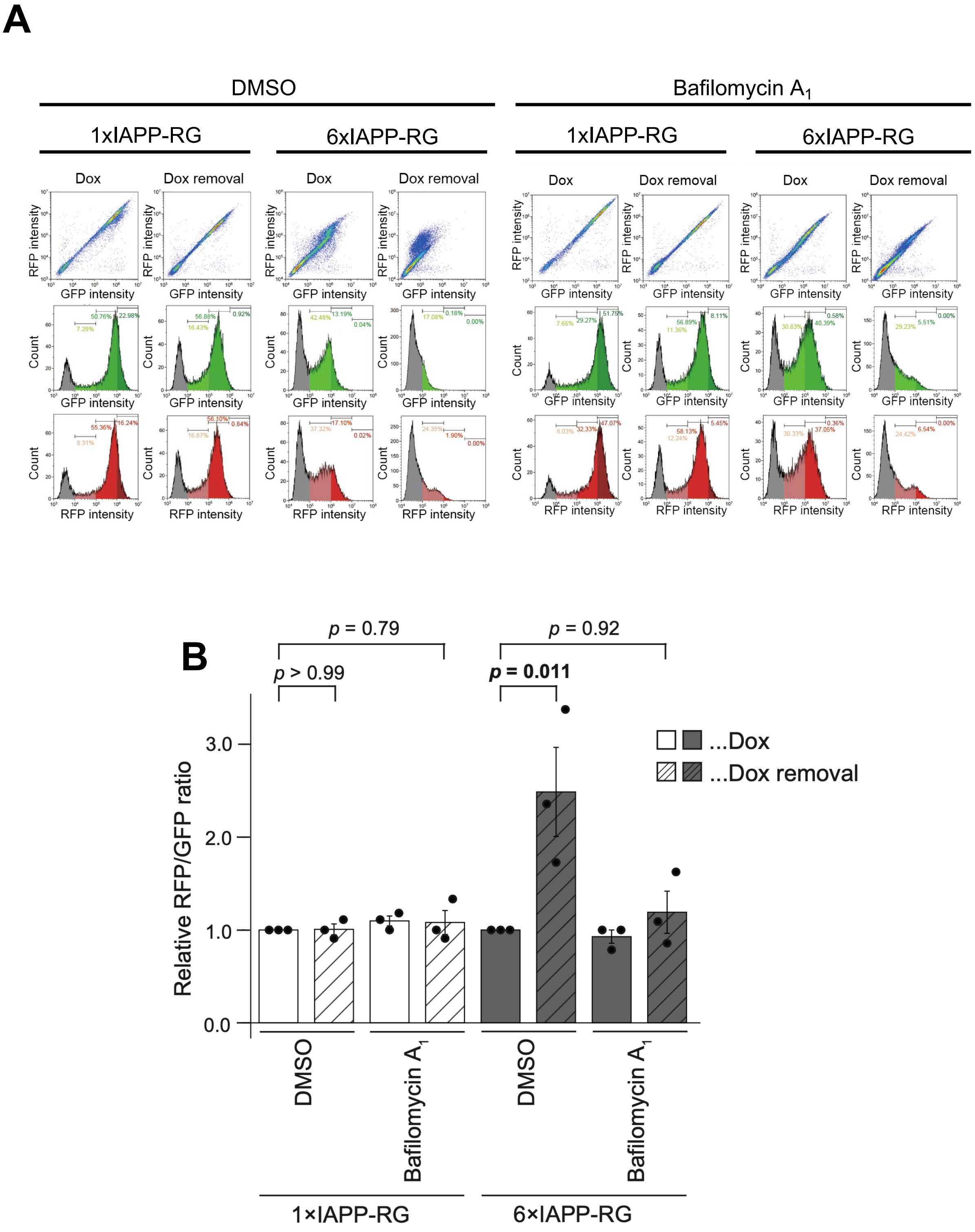

Figure 11. 6xIAPP, but not 1xIAPP, is delivered to lysosomes.

The cells treated with Dox as described above were trypsinized, and their green and red fluorescence intensities were measured using flow cytometry. Representative dot plots of GFP versus RFP intensities and corresponding histograms are shown (A). The fluorescence ratio was calculated in RFP-positive cells. Data represent the mean ± standard error (SE) of at least three independent experiments. Differences were statistically analyzed by Dunnett's multiple comparison test (B).

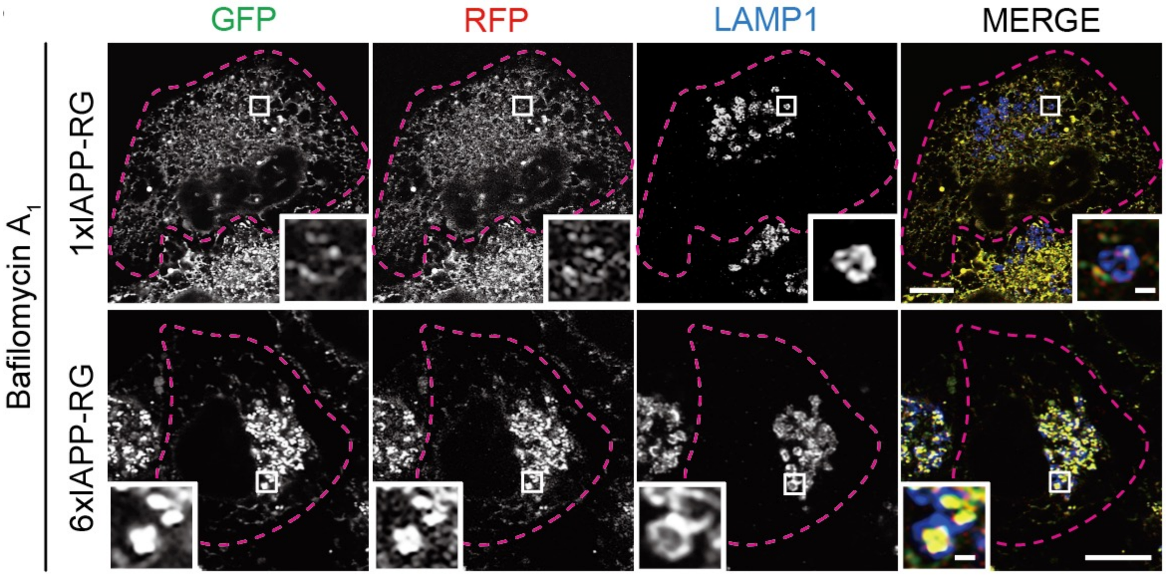

Figure 12. 6xIAPP-RG, but not 1xIAPP-RG, accumulates inside the lysosomes under lysosome inhibition conditions.

Tet-On HeLa cells expressing 1x (or 6x) IAPP-RG were incubated for 48 h with medium containing Dox, then treated with bafilomycin A_1 for 24 h before fixation by formaldehyde. Cells were stained with antibodies against LAMP1 and analyzed through immunofluorescence microscopy. Scale bars represent 10 and 1 μm (inset).

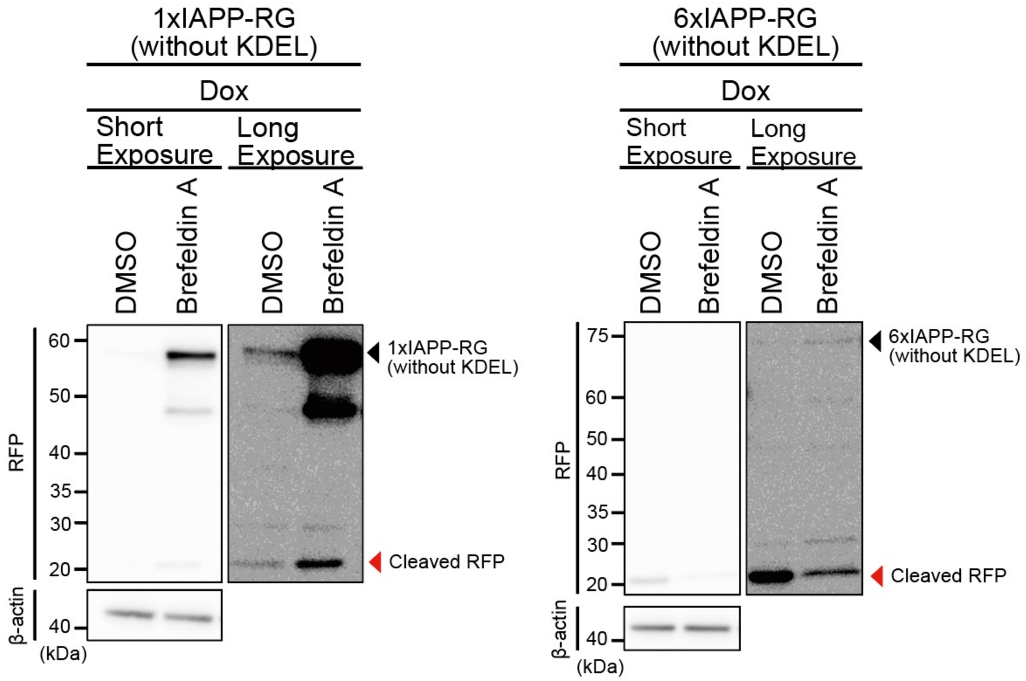

Figure 13. 6xIAPP-RG without KDEL is not suitable to monitor ER-phagy.

Tet-On HeLa cells expressing 6x (or 1x) IAPP-RFP-GFP without KDEL were incubated in medium containing Dox with or without brefeldin A for 24 h prior to immunoblotting using antibodies against RFP and b-actin.

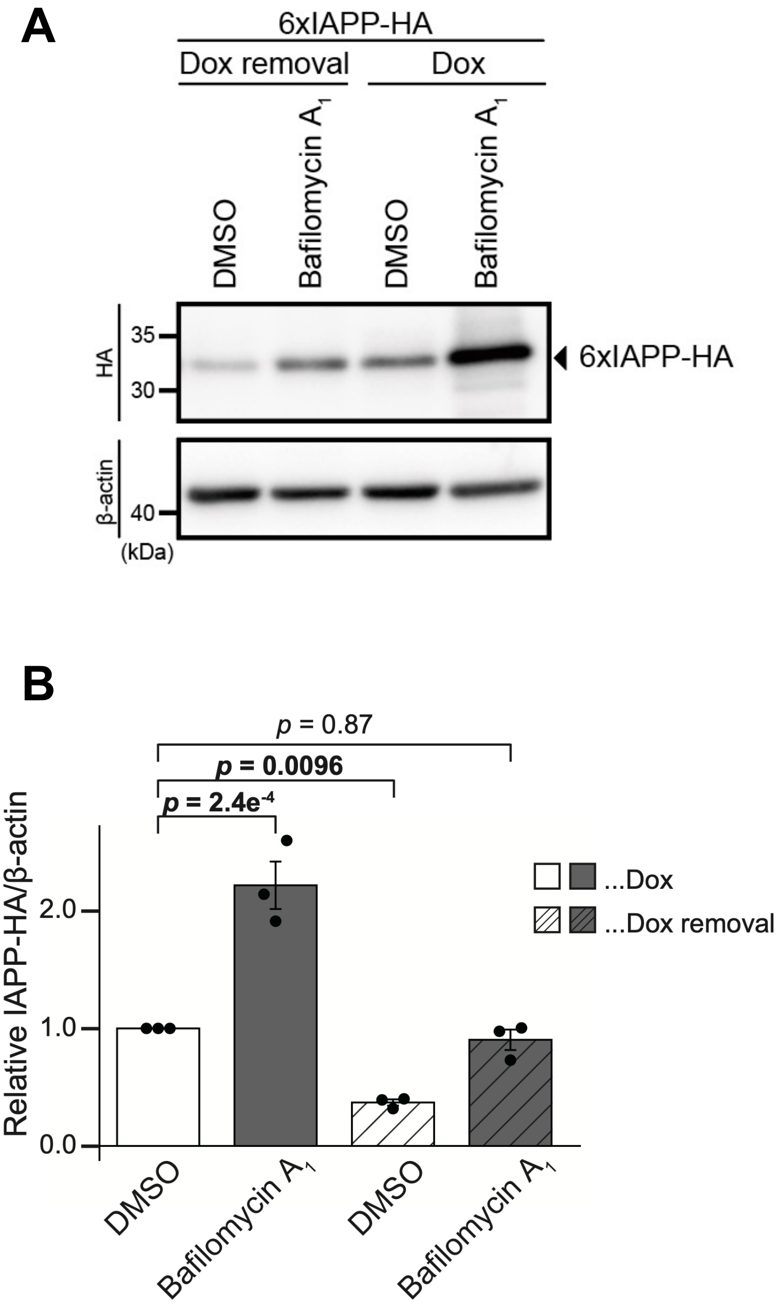

Figure 14. IAPP-HA constructs are degraded by lysosomes.

Tet-On Hela cells expressing 6xIAPP-HA were incubated in medium containing Dox for 24 h, then cultured in medium with or without Dox for a further 24 h. Bafilomycin A_1 treatment was conducted for 24 h before immunoblotting analysis (A). The IAPP-HA/β-actin band intensity ratio (normalized to the DMSO treatment) is shown. Data represent the mean ± SE of three independent experiments. Differences were statistically analyzed by Dunnett's multiple comparison test (B).

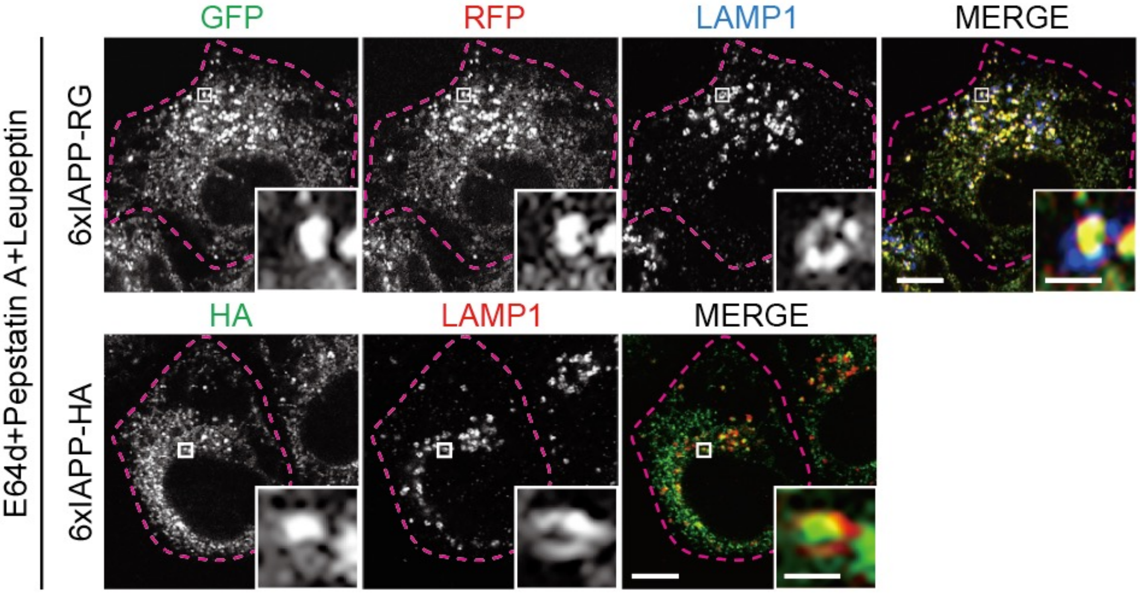

Figure 15. 6xIAPP is accumulated in lysosomes upon treatment with lysosomal protease inhibitors.

Tet-On HeLa cells expressing 6xIAPP-RG or 6xIAPP-HA were incubated with medium containing Dox, then treated with a lysosomal enzyme inhibitor cocktail containing E64d with pepstatin A and leupeptin for 24 h before fixation by formaldehyde. Cells were stained with antibodies against LAMP1 and HA, then analyzed through immunofluorescence microscopy. Scale bars represent 10 and 1 μm (inset).

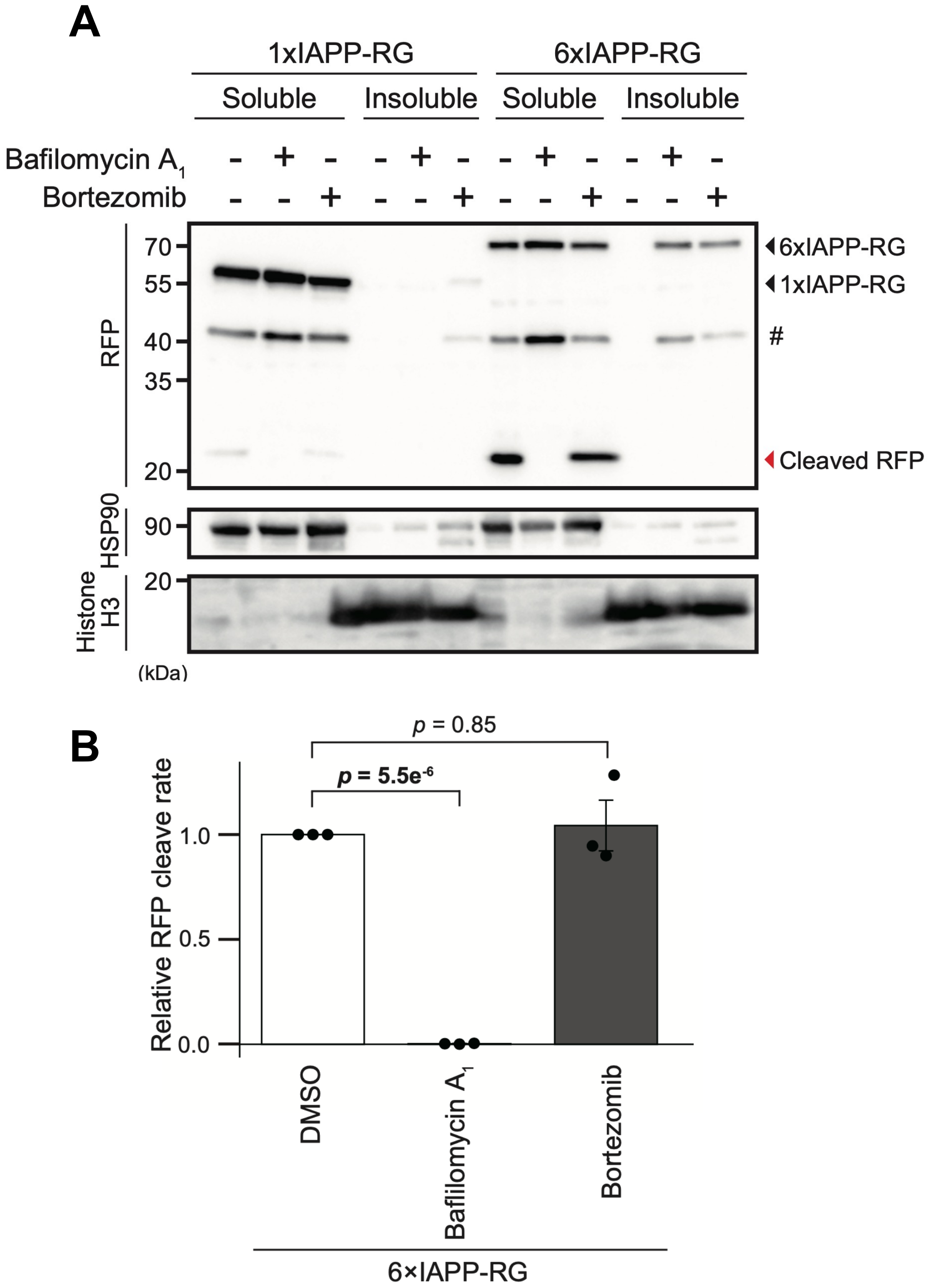

Figure 16. Proteasomal inhibition is not related to lysosomal degradation of 6xIAPP.

Tet-On HeLa cells expressing 1x (or 6x) IAPP-RG were cultured in medium containing Dox with dimethylsulfoxide (DMSO), bafilomycin A_1 or bortezomib for 24 h prior to immunoblotting analysis using antibodies against RFP, HSP90 and Histone H3. Cell lysates were centrifuged, and the supernatants were collected as the soluble fraction. The pellets containing the nuclear compartment were collected as the insoluble fraction. Each pellet was resuspended in an equal volume of lysis buffer. # indicates degradative products of IAPP-RG (A). The band intensities of cleaved RFP and 6xIAPP-RG were quantified, and the ratio of cleaved RFP/total amount of 6xIAPP (normalized to DMSO treatment) is shown. Data represent the mean ± SE of three independent experiments. Differences were statistically analyzed by Dunnett's multiple comparison test (B).

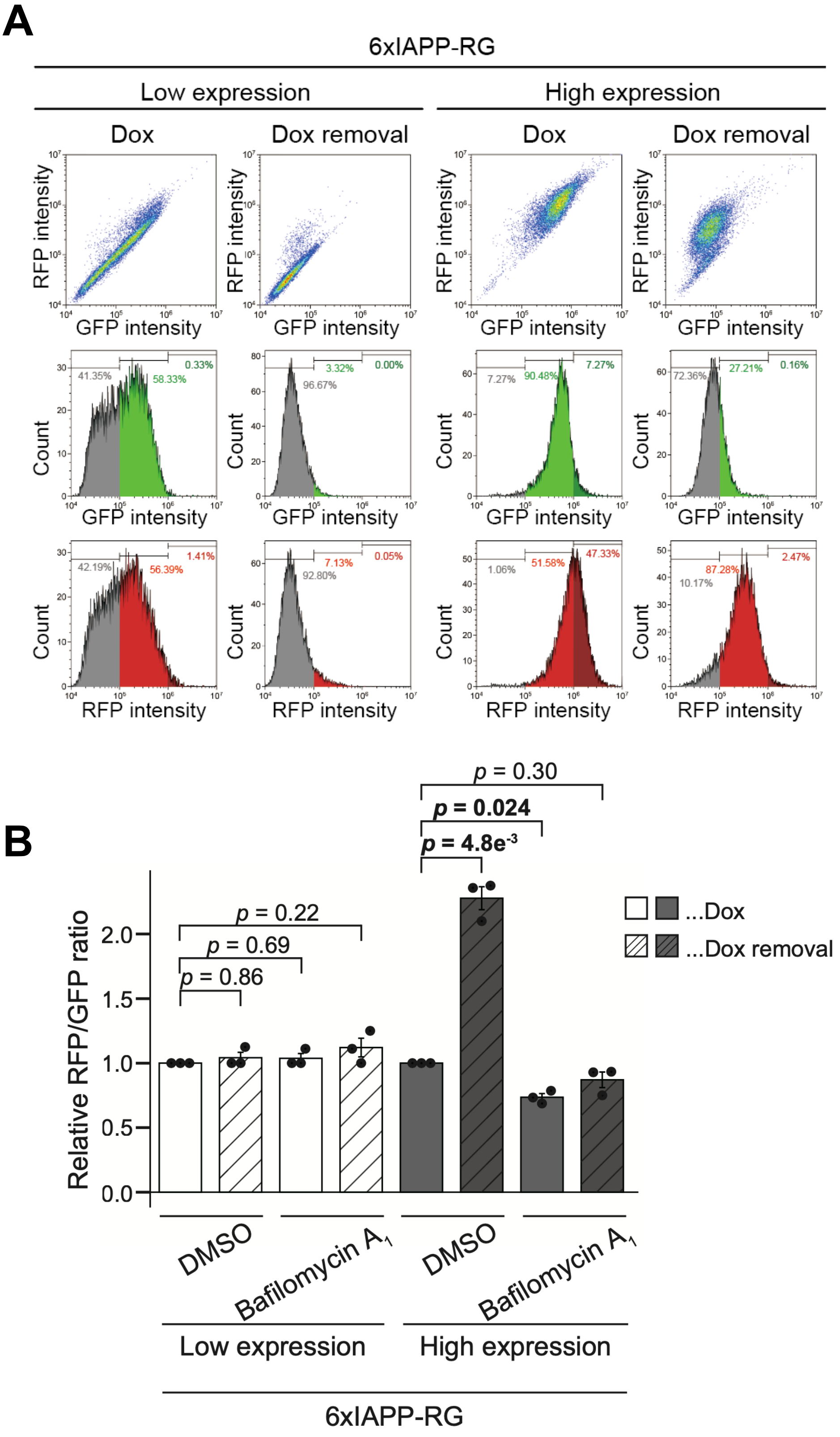

Figure 17. 6xIAPP forms two distinct populations for lysosomal or proteasomal degradation.

Tet-On HeLa cells with low or high expression of 6xIAPP-RG were cultured with Dox for 24 h, and then incubated in medium with or without Dox for another 24 h prior to analysis. All samples were treated with DMSO or bafilomycin A_1 for 24 h. The GFP and RFP fluorescence intensities of each cell are shown as dot plots (A). Data represent the mean ± SE of three independent experiments. Differences were statistically analyzed by Dunnett's multiple comparison test (B).

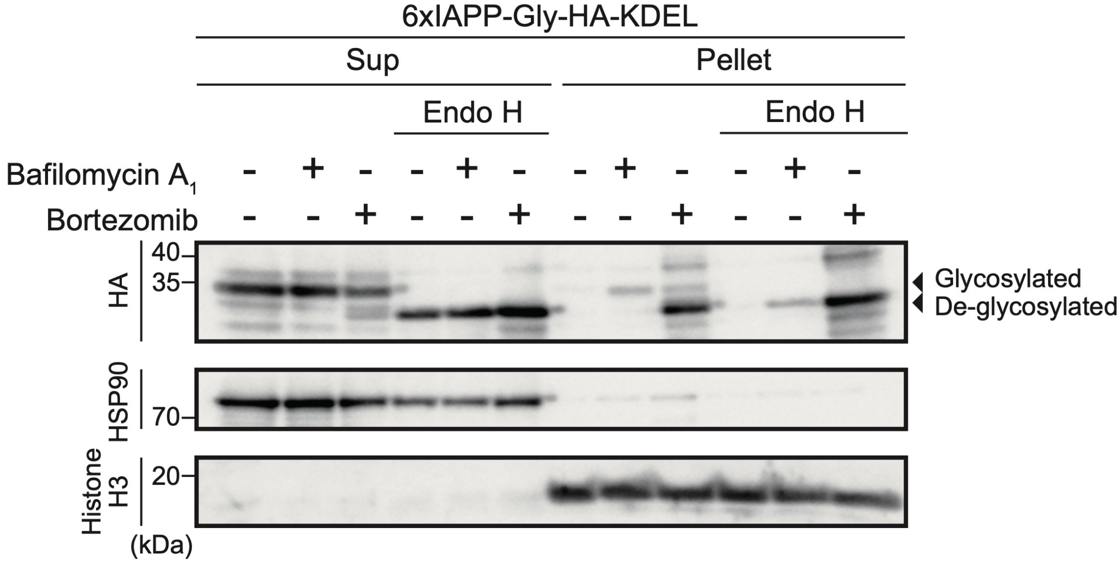

Figure 18. Lysosome inhibition leads to glycosylated 6xIAPP accumulation.

Tet-On HeLa cells expressing 6x (or 1x) IAPP-Gly-HA-KDEL were cultured in medium containing Dox for 24 h and treated with DMSO, bafilomycin A_1 or bortezomib for 24 h. The cells were lysed and centrifuged, and the supernatants were collected as the soluble fraction. Pellets containing the nuclear compartment were collected as the insoluble fraction. Each fraction was treated with endoglycosidase H prior to immunoblotting analysis using antibodies against RFP, HSP90 and Histone H3.

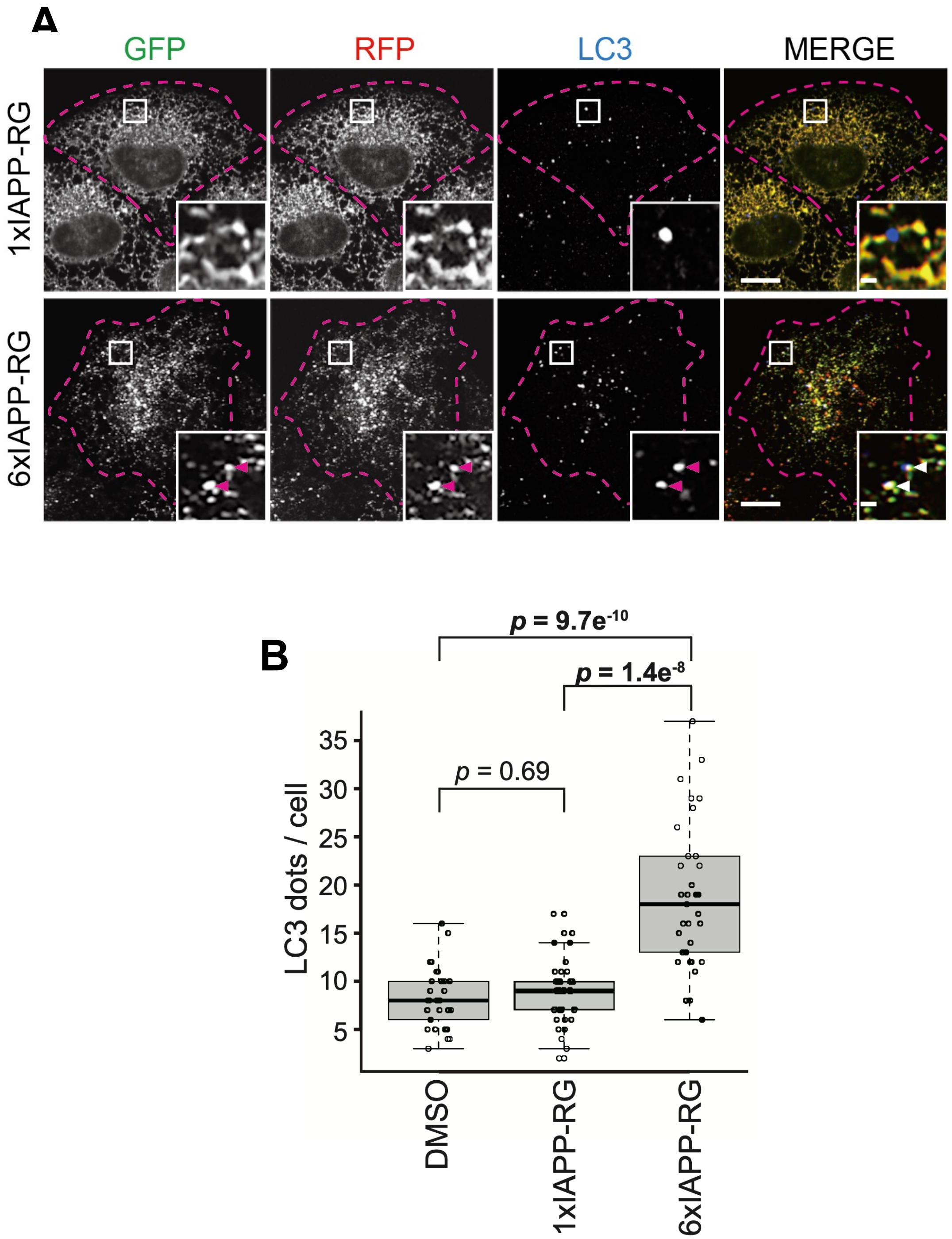

Figure 19. Dot structures of 6xIAPP-RG co-localized with endogenous LC3.

Tet-On HeLa cells expressing 1x (or 6x) IAPP-RG were incubated in medium containing Dox for 48 h before fixation. The cells were stained with antibodies against LC3 and analyzed through confocal microscopy. Scale bars represent 10 and 1 μm (inset) (A). Quantification of the number of LC3 puncta per cell. Solid bars indicate the median, boxes the interquartile range (25th–75th percentile), and whiskers the 0th–100th percentile range. Data were collected from 33 cells of each cell type. Differences were analyzed using one-way analysis of variance (ANOVA) and Sidak's multiple comparison test (B).

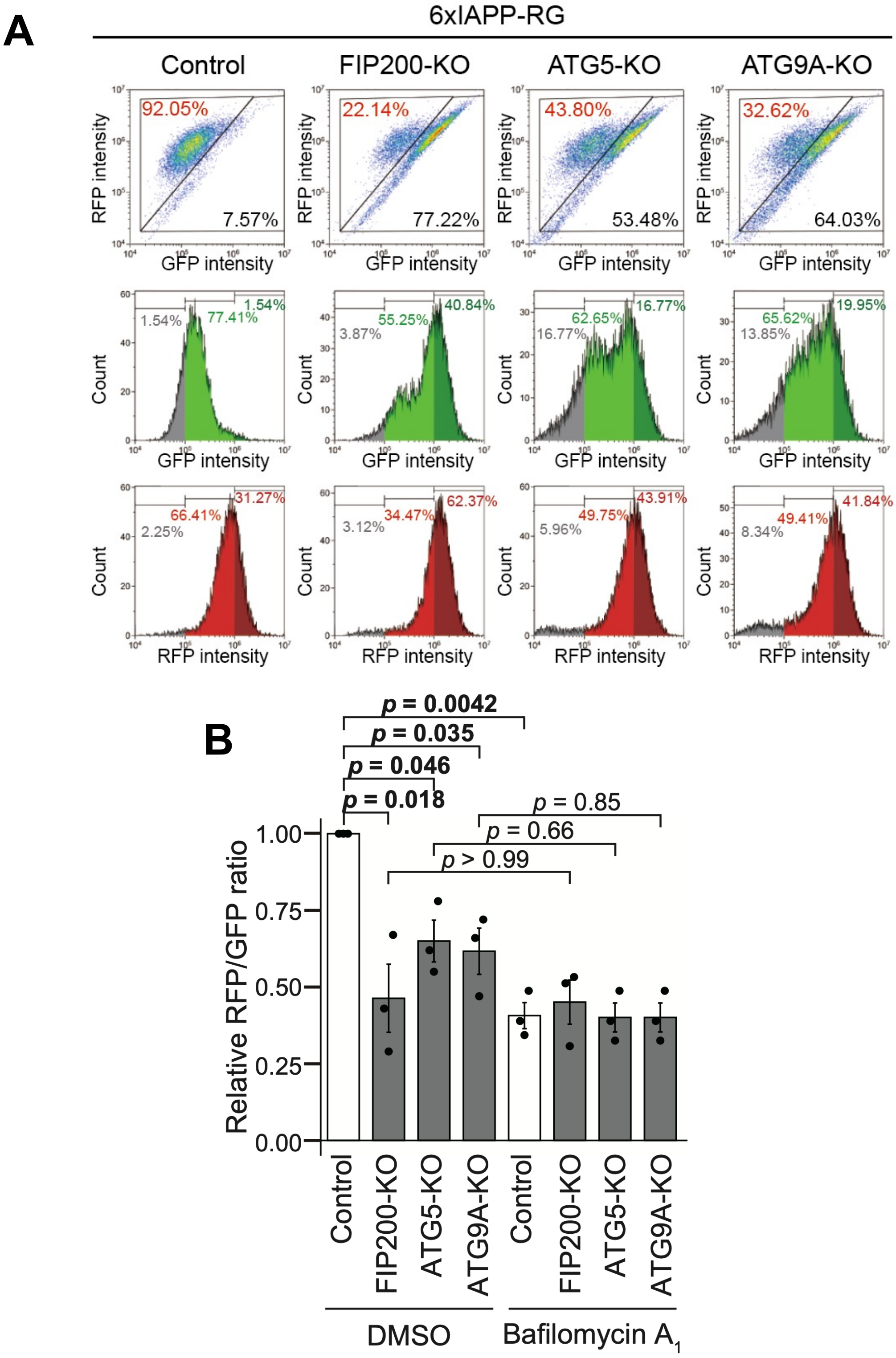

Figure 20. 6xIAPP-RG accumulated in autophagy-KO cells.

Tet-On HeLa cells stably expressing Cas9 and the indicated sgRNA were cultured in the presence of Dox for 24 h (A mixed population of wild-type [WT] and knockout [KO] cells is used). Following the removal of Dox, the cells were cultured with or without bafilomycin A_1 for 24 h prior to flow cytometry. Dot plots of GFP versus RFP fluorescence intensities are shown, with black letters indicating the lysosomal fraction (%) and red letters all other fractions (%) (A). The fluorescence ratio was calculated for RFP-positive cells. Data represent the mean ± SE of three independent experiments. Differences were analyzed using one-way ANOVA and Sidak's multiple comparison test (B).

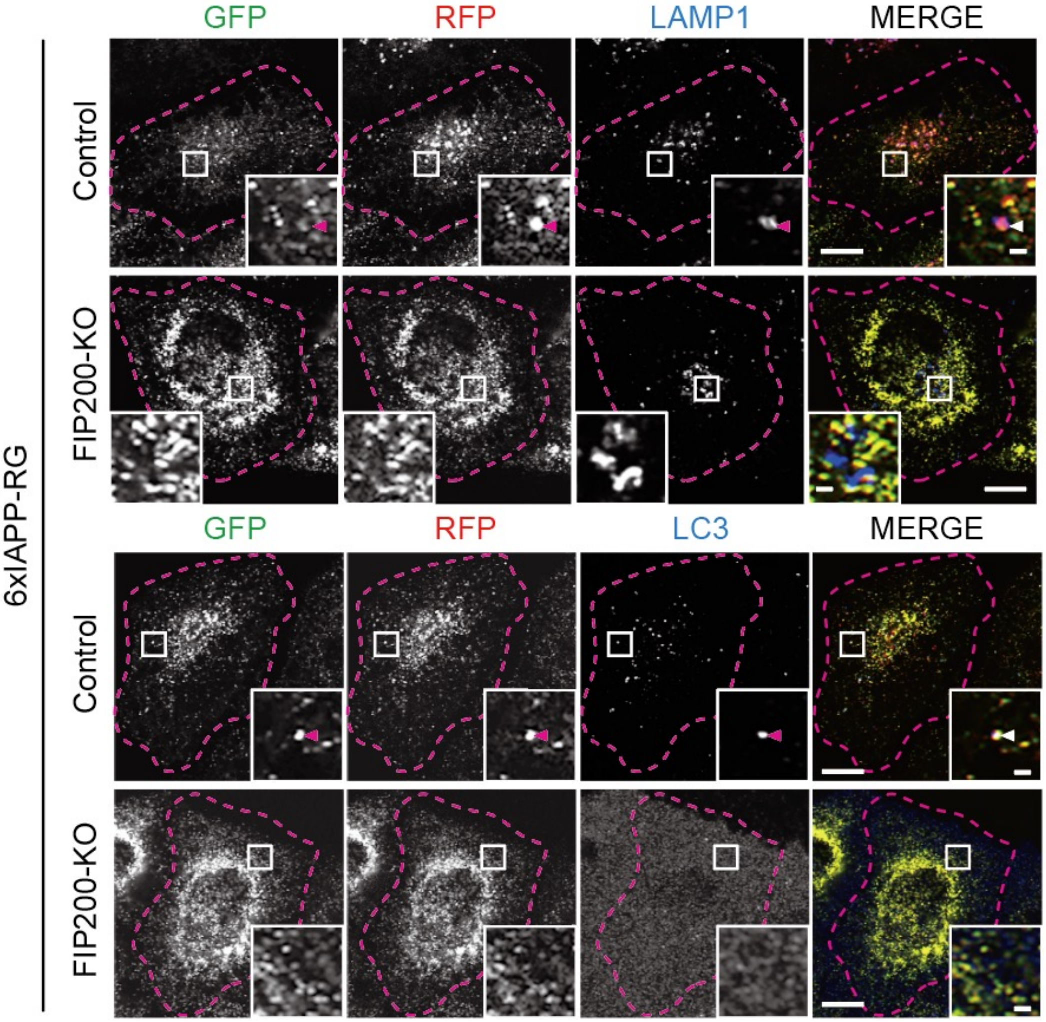

Figure 21. 6xIAPP-RFP-GFP-KDEL accumulated in autophagy-KO cells.

HeLa cells stably expressing Cas9 and sgRNA for FIP200 or non-target (control) sgRNA were treated with Dox for 24 h to induce expression of 6xIAPP-RFP-GFP-KDEL before fixation. Cells were stained with antibodies against LAMP1 or LC3 and analyzed through immunofluorescence microscopy. Scale bars represent 10 and 1 μm (inset).

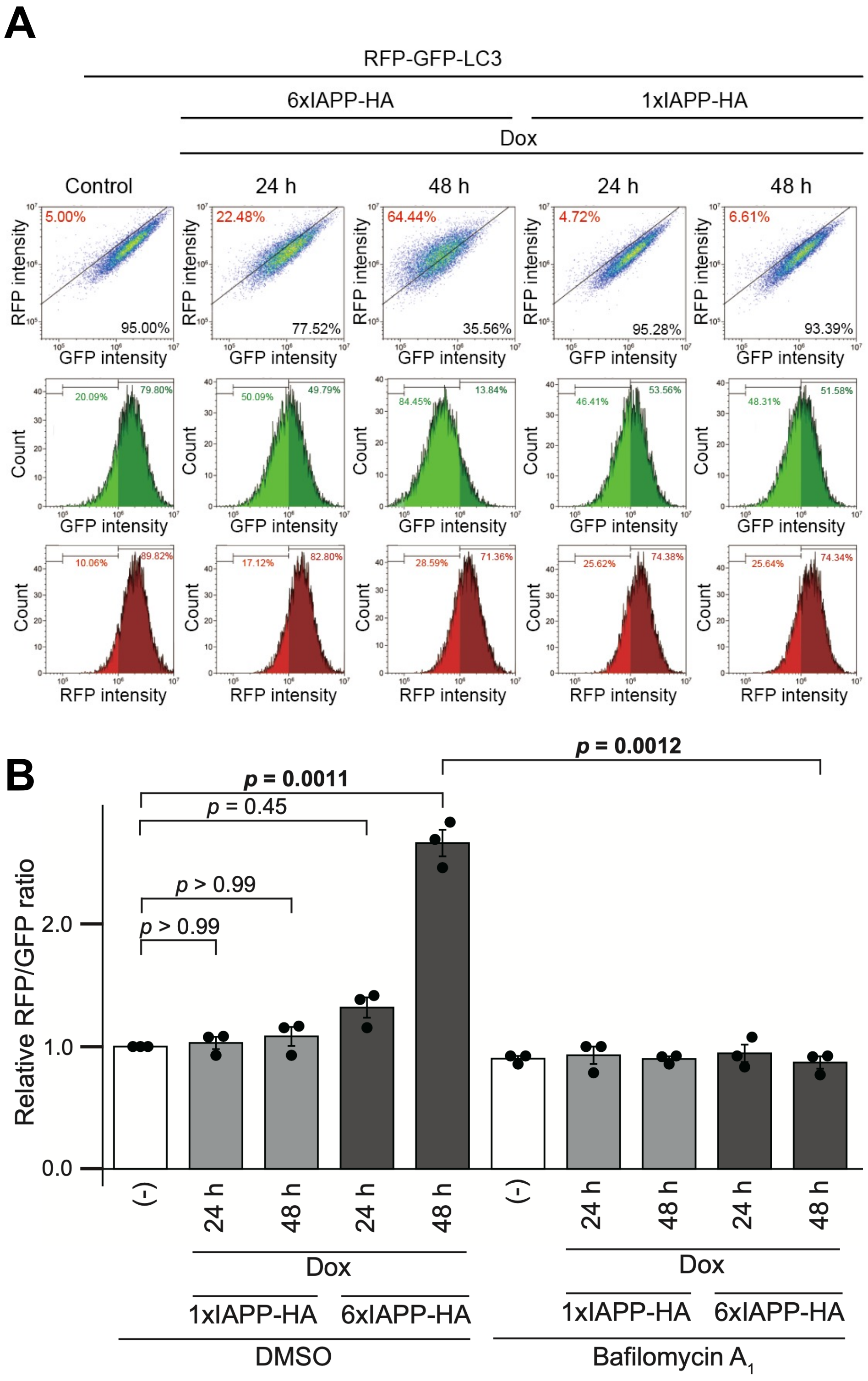

Figure 22. The expression of 6xIAPP, but not 1xIAPP, induces significant elevation of the fluorescence ratio of RFP-GFP-LC3.

HeLa cells stably expressing RFP-GFP-LC3 with 1x (or 6x) IAPP-HA (Tet-On) were cultured in medium, with or without Dox, for 24 or 48 h. All samples were treated with DMSO or bafilomycin A_1 for 24 or 48 h, then subjected to flow cytometric analysis. The GFP and RFP fluorescence intensities were analyzed through flow cytometry (A). The fluorescence ratio was calculated for RFP-positive cells. Data represent the mean ± SE of three independent experiments. Differences were analyzed using one-way ANOVA and Sidak's multiple comparison test (B).

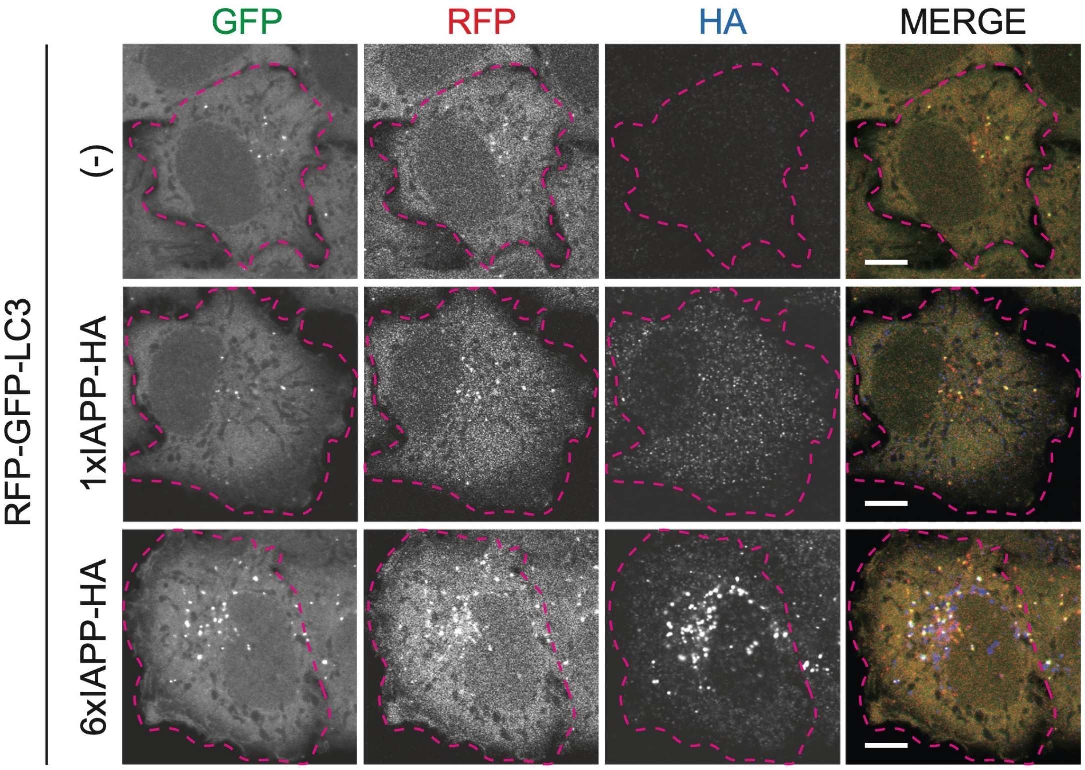

Figure 23. The expression of 6xIAPP, but not 1xIAPP, induces significant elevation of the fluorescence ratio of RFP-GFP-LC3.

HeLa cells stably expressing RFP-GFP-LC3 with 1x (or 6x) IAPP-HA (Tet-On) treated with Dox as described above were fixed and stained with antibodies against HA-tag, and then analyzed through immunofluorescence microscopy. Scale bars represent 10 μm.

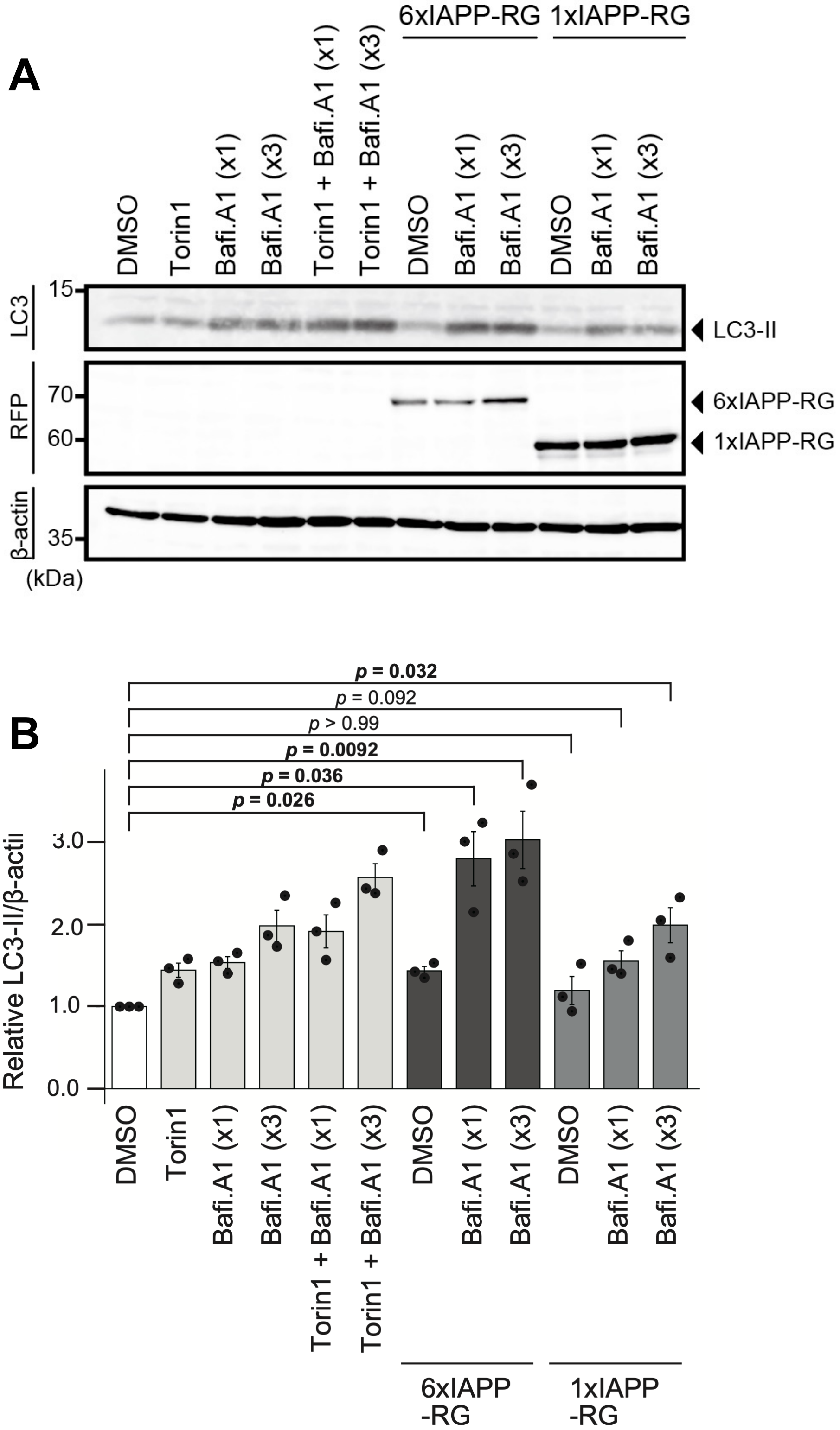

Figure 24. Endogenous LC3-II accumulated after the induction of 6xIAPP.

WT HeLa cells or Tet-On HeLa cells, expressing 1x (or 6x) IAPP-RG cultured with Dox for 24 h, were treated with Torin 1, bafilomycin A_1, or both for 2 h prior to immunoblotting (A). The ratio of LC3-II to β-actin is shown. Data represent the mean ± SE of three independent experiments. Differences were statistically analyzed by Dunnett's multiple comparison test (B).

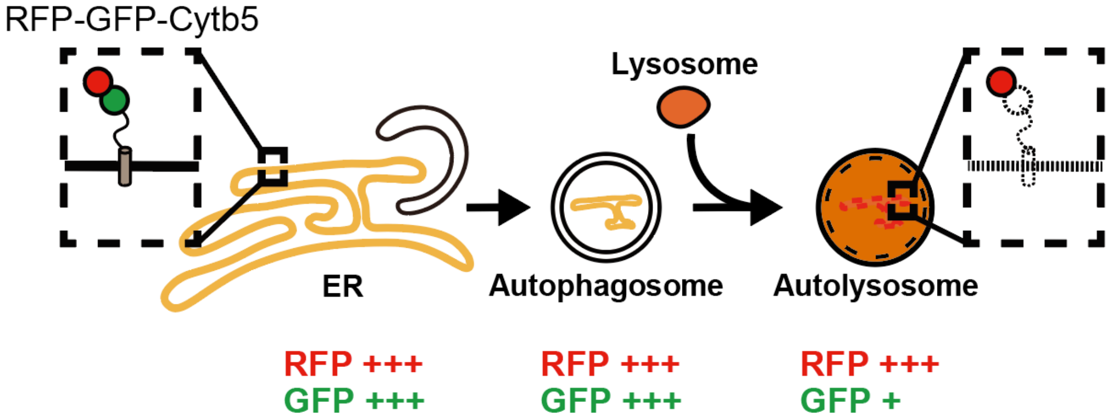

Figure 25. Schematic diagram of RG-Cytb5.

RG-Cytb5, an ER membrane protein, is co-degraded through bulk ER-phagy.

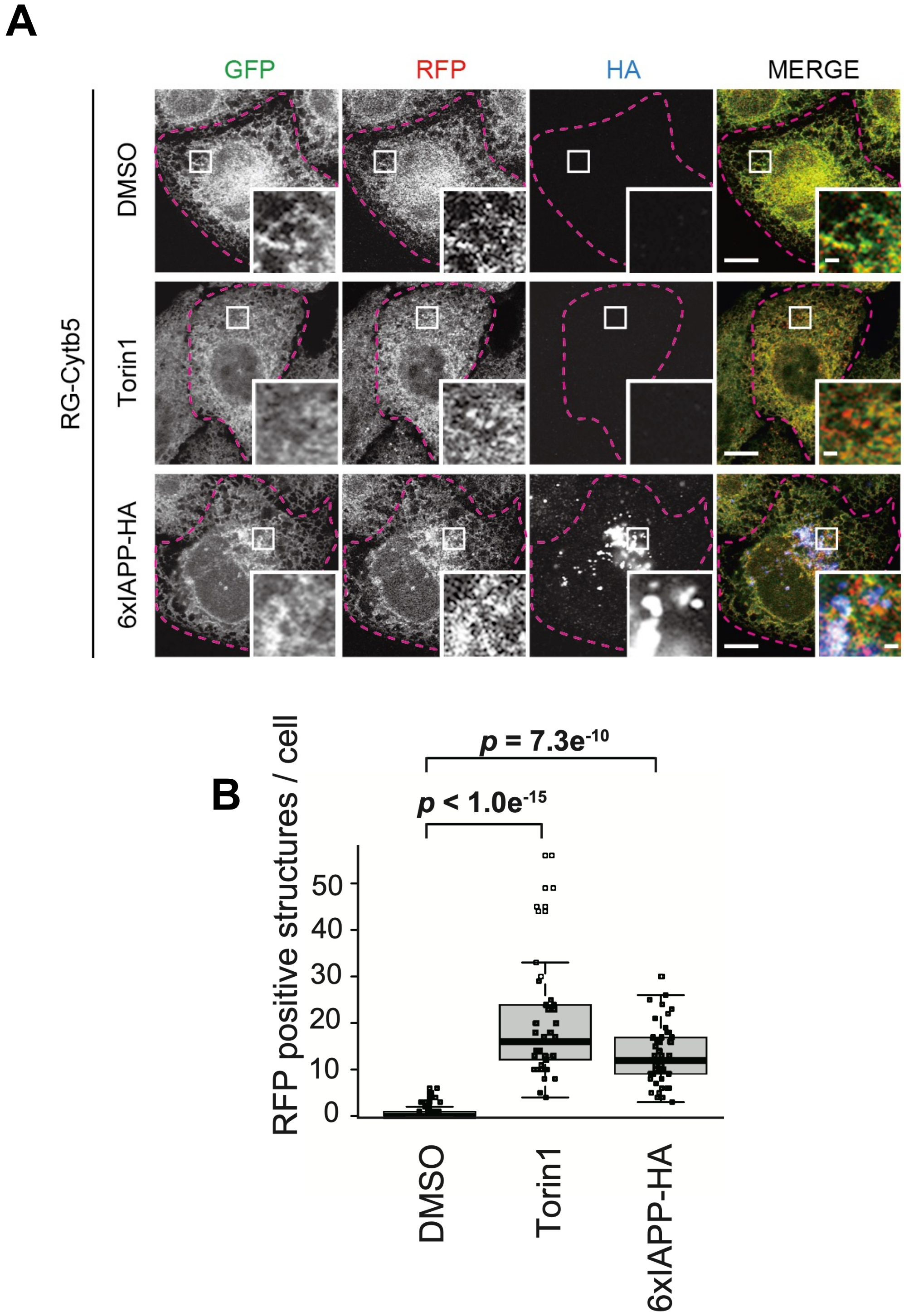

Figure 26. 6xIAPP induces lysosomal degradation of an ER protein.

HeLa cells stably expressing RFP-GFP-Cytb5 were incubated with Dox to induce 6xIAPP-HA-KDEL expression, or with Torin 1, for 24 h. After fixation, cells were stained with antibodies against HA and analyzed through immunofluorescence microscopy. GFP-negative and RFP-positive signals (arrowhead) are indicated. Scale bars represent 10 and 1 µm (inset) (A). Quantification of the number of GFP negative, RFP positive puncta per cell. Solid bars indicate the median, boxes the interquartile range (25th–75th percentile), and whiskers the 0th–100th percentile range. Data were collected from 45 cells of each cell type Differences were statistically analyzed by Dunnett's multiple comparison test. (B).

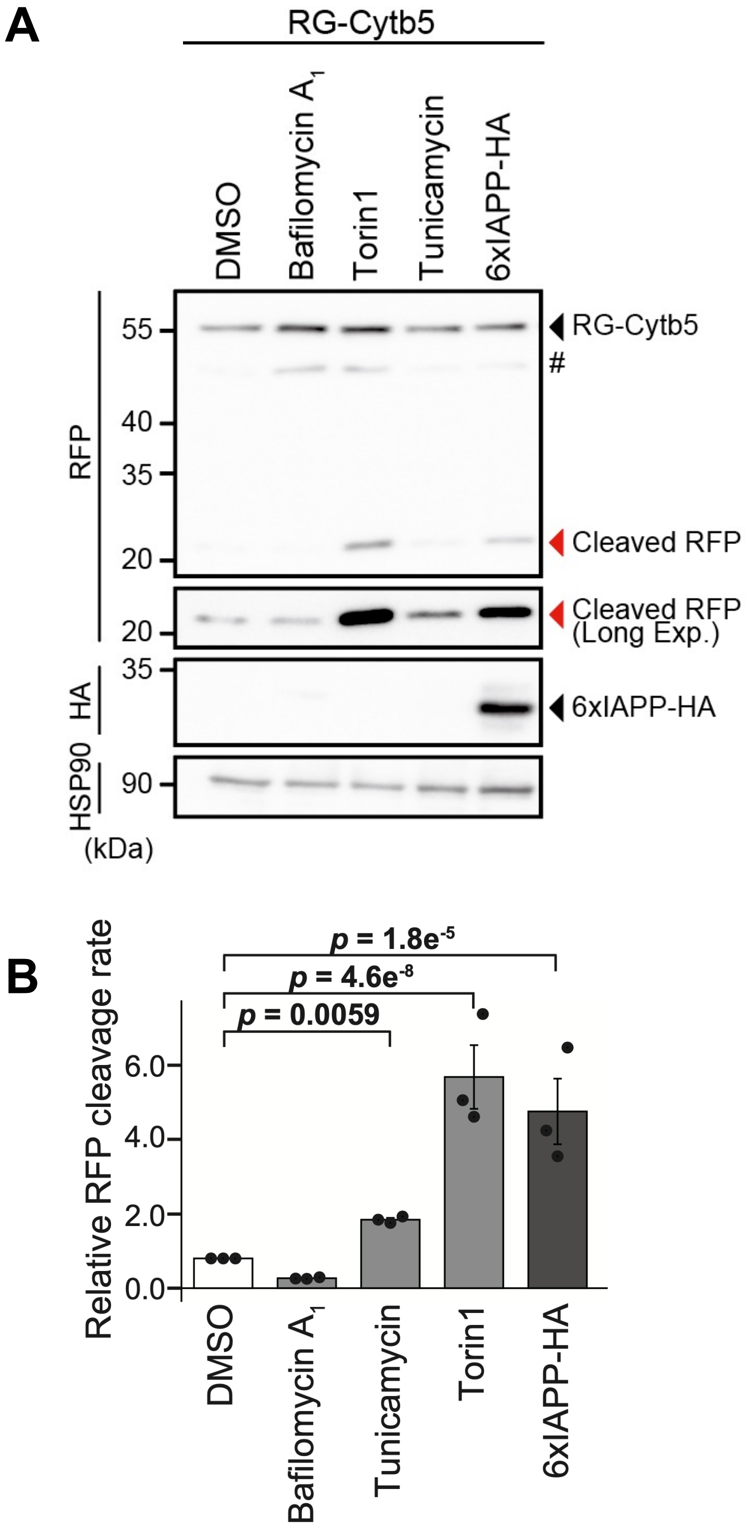

Figure 27. 6xIAPP induces lysosomal degradation of an ER protein.

HeLa cells stably expressing RG-Cytb5 were treated with the indicated compounds or Dox for induction of 6xIAPP-HA expression for 24 h. Cell lysates were analyzed through immunoblotting using antibodies against RFP, HA, or endogenous HSP90 (loading control). # indicates degradative products of RG-Cytb5 (A). The cleaved RFP/RG-Cytb5 band intensity ratio (normalized to the WT) is shown. Data represent the mean ± SE of three independent experiments. Differences were statistically analyzed by Dunnett's multiple comparison test (B).

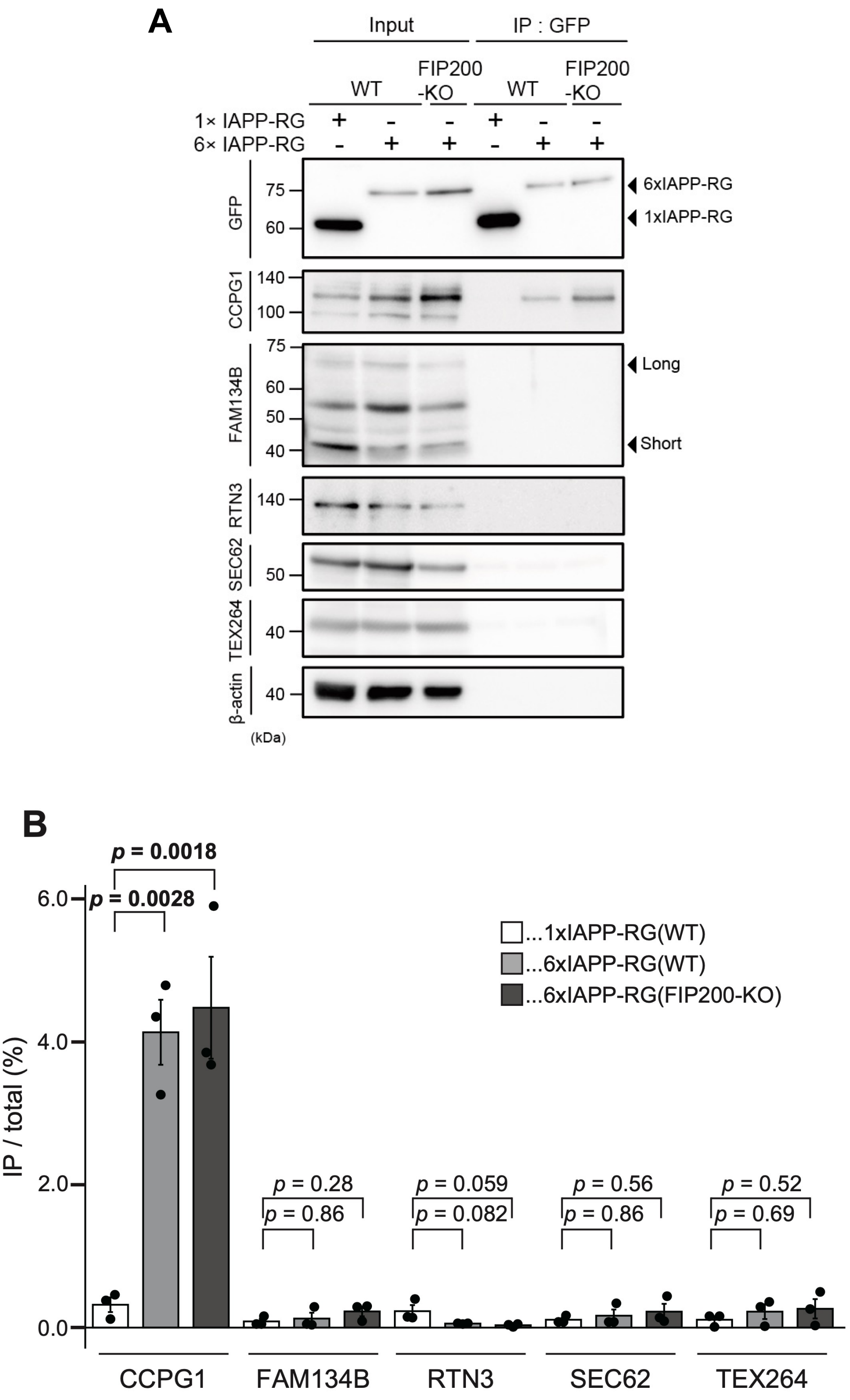

Figure 28. 6xIAPP-RFP-GFP-KDEL selectively interacts with CCPG1 in mammalian cells.

Tet-On HeLa cells (WT and FIP200-KO) expressing 1xIAPP-RFP-GFP-KDEL or 6xIAPP-RFP-GFP-KDEL were cultured with Dox for 48 h prior to IP. Inputs (5% of total) and immunoprecipitants (80% of total) were analyzed through immunoblotting using the indicated antibodies (A). The IP product/Input band intensity ratio is shown. Data represent the mean ± SE of independent experiments. Differences were statistically analyzed by Dunnett's multiple comparison test. (B).

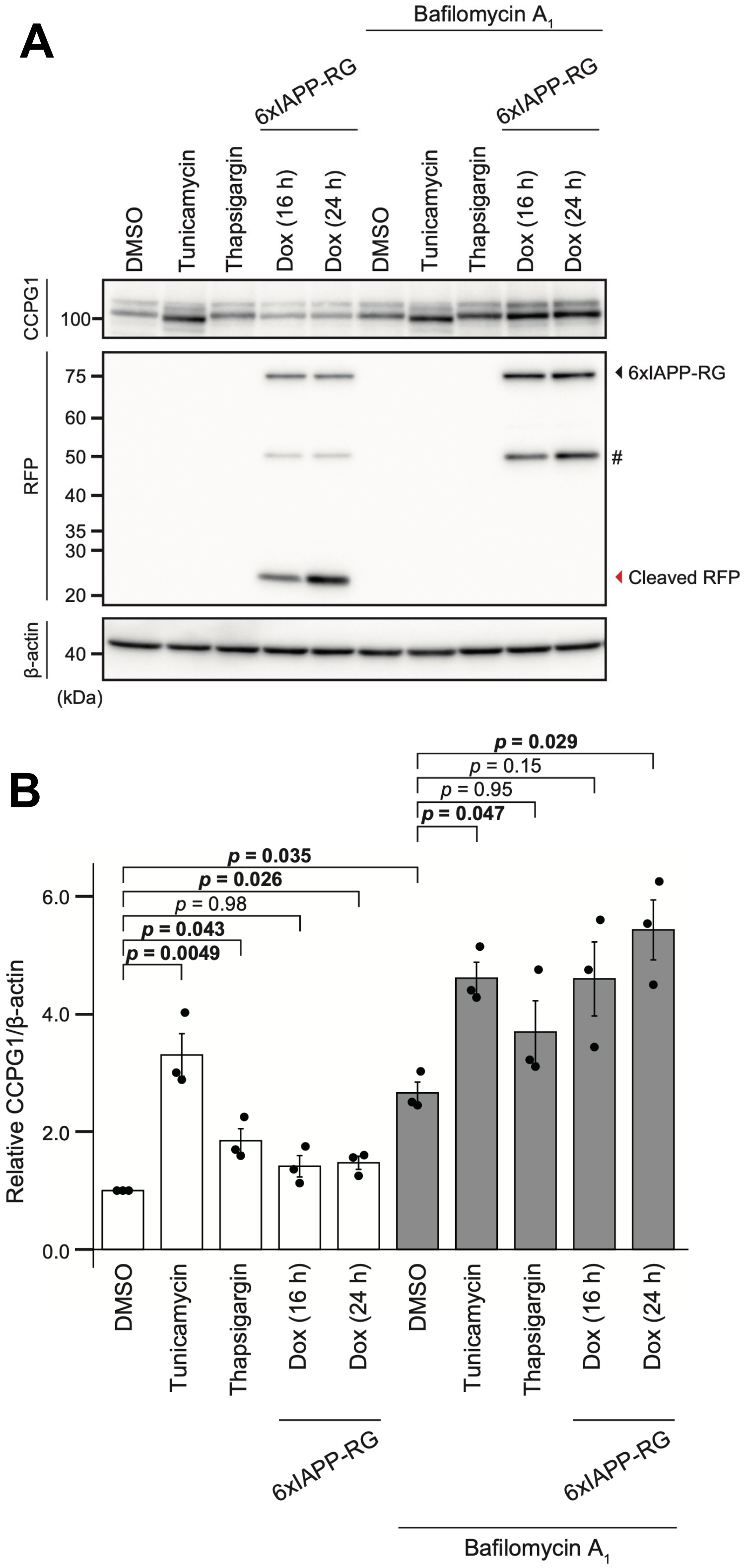

Figure 29. Induction of 6xIAPP elevates protein level of CCPG1.

Tet-On HeLa cells highly expressing 6xIAPP-RG were treated with tunicamycin or thapsigargin for 16 h, or Dox for 16–24 h, with or without bafilomycin A_1. Cells were lysed with buffer containing 1% Triton X-100, then analyzed through immunoblotting using antibodies against CCPG1, RFP, and β-actin (loading control). # indicates degradative products of 6xIAPP-RG (A). Band intensities were quantified and are shown as mean ± SE. Differences were analyzed using one-way ANOVA and Sidak's multiple comparison test (B).

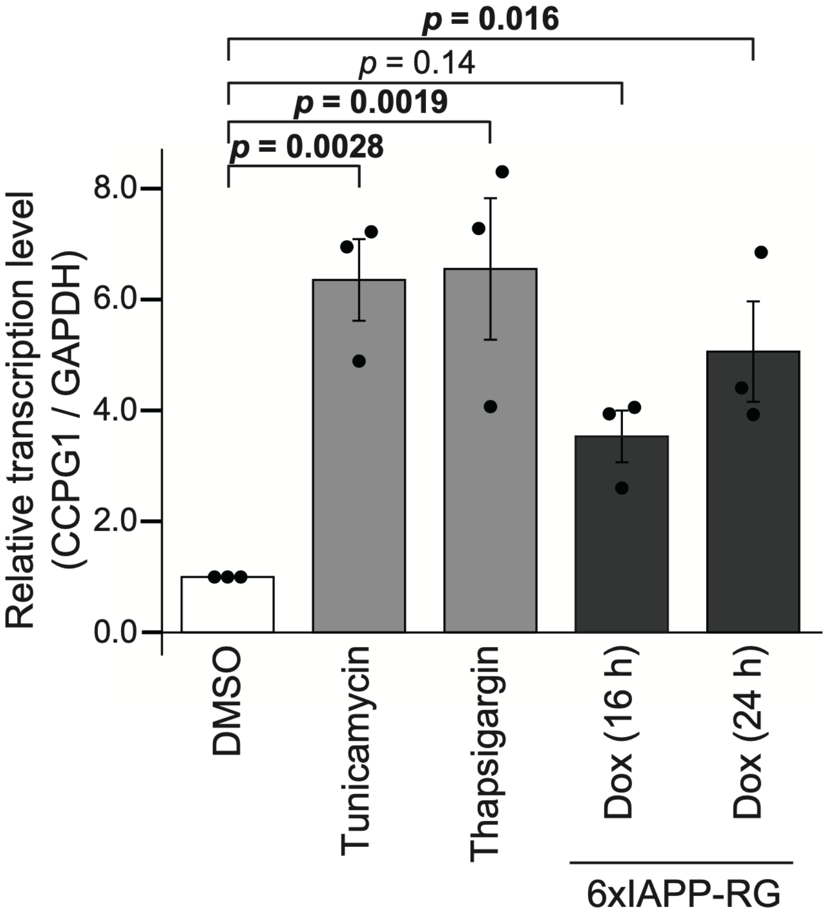

Figure 30. The expression of 6xIAPP promotes transcription of CCPG1.

Tet-On HeLa cells highly expressing 6xIAPP-RG were treated with each of the ER stressors for 16 h, or Dox to induce 6xIAPP-RG for 16–24 h. Quantitative real-time PCR was performed for endogenous CCPG1 and GAPDH (loading control). Data represent the mean ± SE of three independent experiments. Differences were statistically analyzed by Dunnett's multiple comparison test.

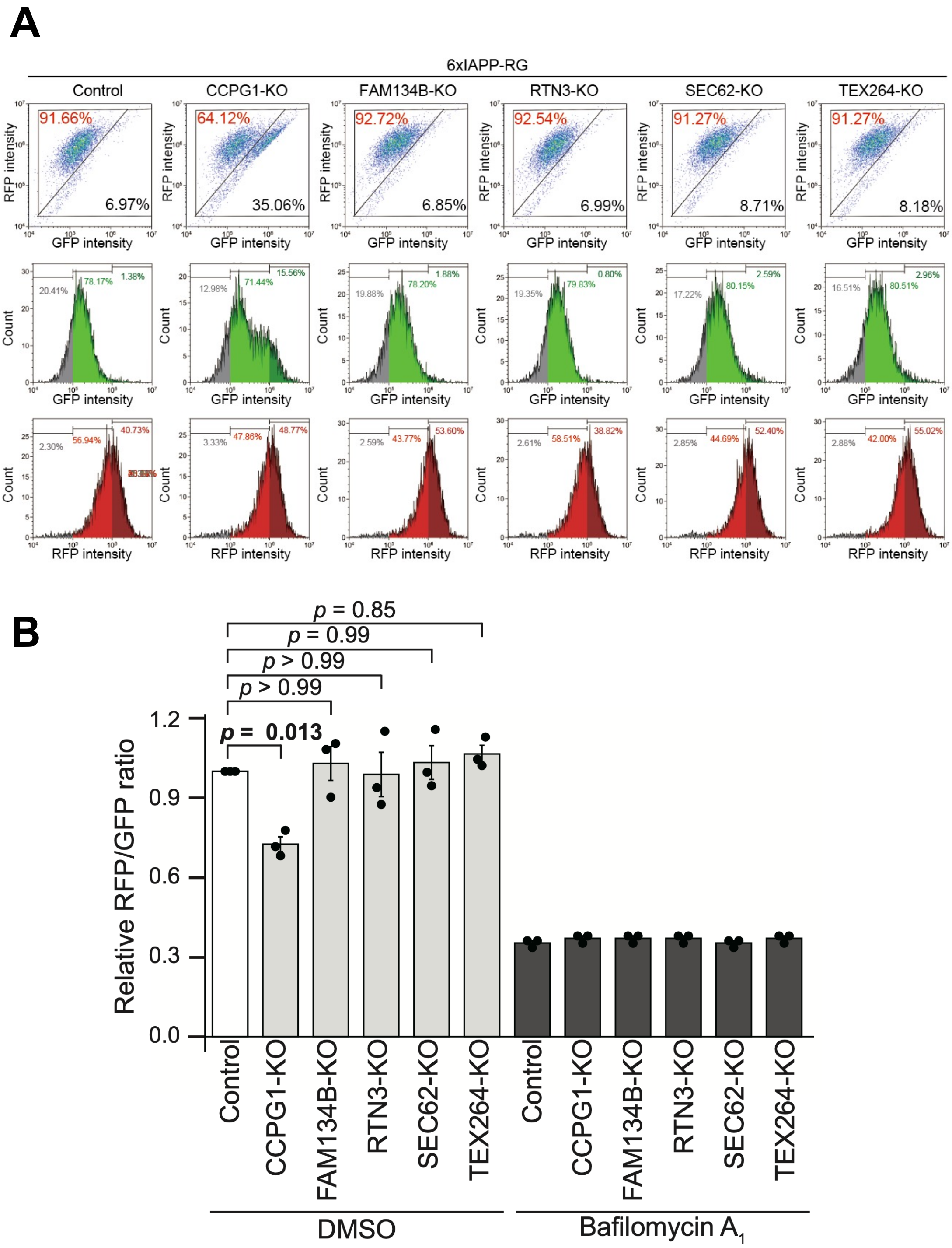

Figure 31. Among ER-phagy receptors, CCPG1 is responsible for the degradation of 6xIAPP.

Tet-On HeLa cells expressing 6xIAPP-RG (a high-expression clone) were treated with Cas9 and each indicated sgRNA sequence using a lentivirus system. After antibiotic selection for at least 7 days, the cells were incubated with medium containing Dox for 24 h, and then cultured in Dox-free medium with or without bafilomycin A_1 for a further 24 h. The cells were trypsinized, and green and red fluorescence intensities were then measured through flow cytometry. Representative dot plots of GFP versus RFP intensities and corresponding histograms are shown (A). The fluorescence ratio was calculated for RFP-positive cells. Data represent the mean ± SE of three independent experiments. Differences were statistically analyzed by Dunnett's multiple comparison test (B).

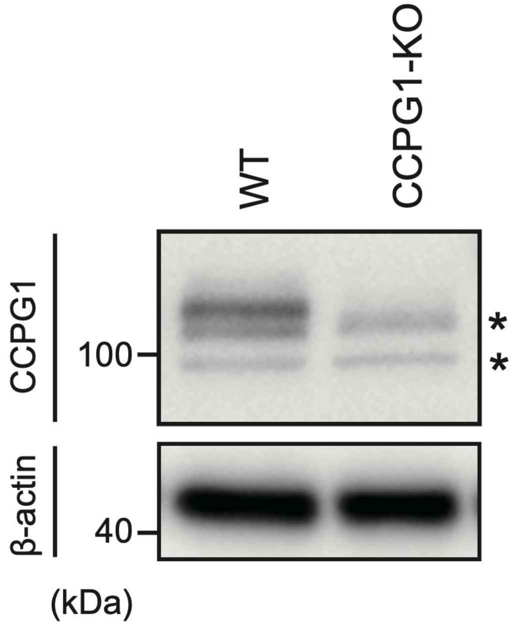

Figure 32. Establishment of clonal CCPG1-KO HeLa cells.

WT cells and clonal CCPG1-KO cells generated using CRISPR were analyzed through immunoblotting using antibodies against endogenous CCPG1 and β-actin (loading control). * indicates non-specific bands.

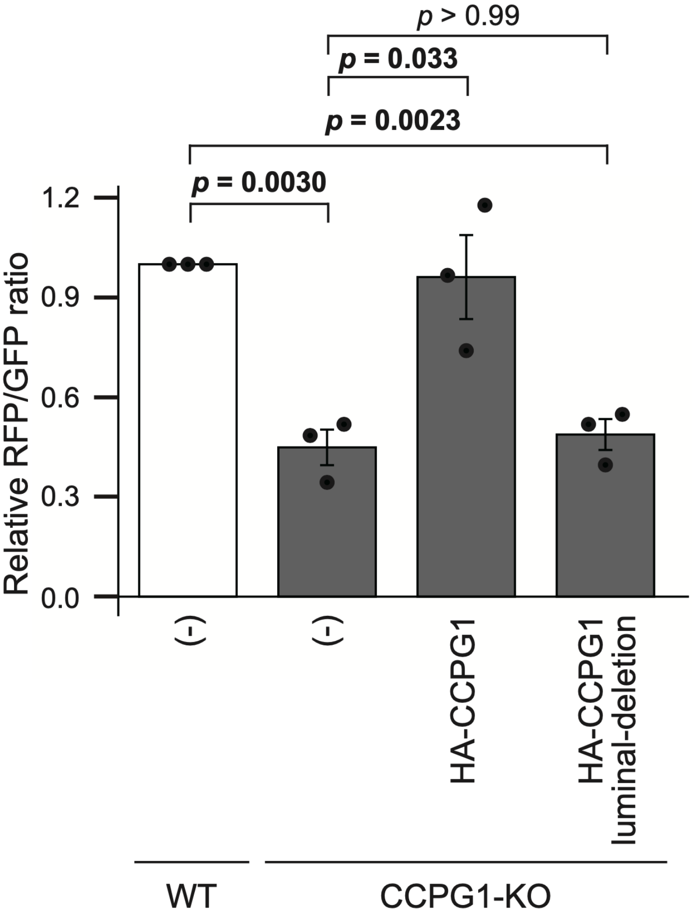

Figure 33. Lysosomal degradation of 6xIAPP-RFP-GFP-KDEL occurs in a manner dependent on the ER-luminal region of CCPG1.

WT and CCPG1-KO HeLa cells expressing 6xIAPP-RFP-GFP-KDEL, with or without exogenous HA-CCPG1 (full-length or luminal deletion mutant), were incubated in medium containing Dox and then subjected to flow cytometry. After 24 h of incubation in Dox-containing medium, the cells were incubated with Dox-free medium for a further 24 h. The fluorescence ratio was calculated for RFP-positive cells. Data represent the mean ± SE of three independent experiments. Differences were statistically analyzed by one-way ANOVA and Sidak's multiple comparison test.

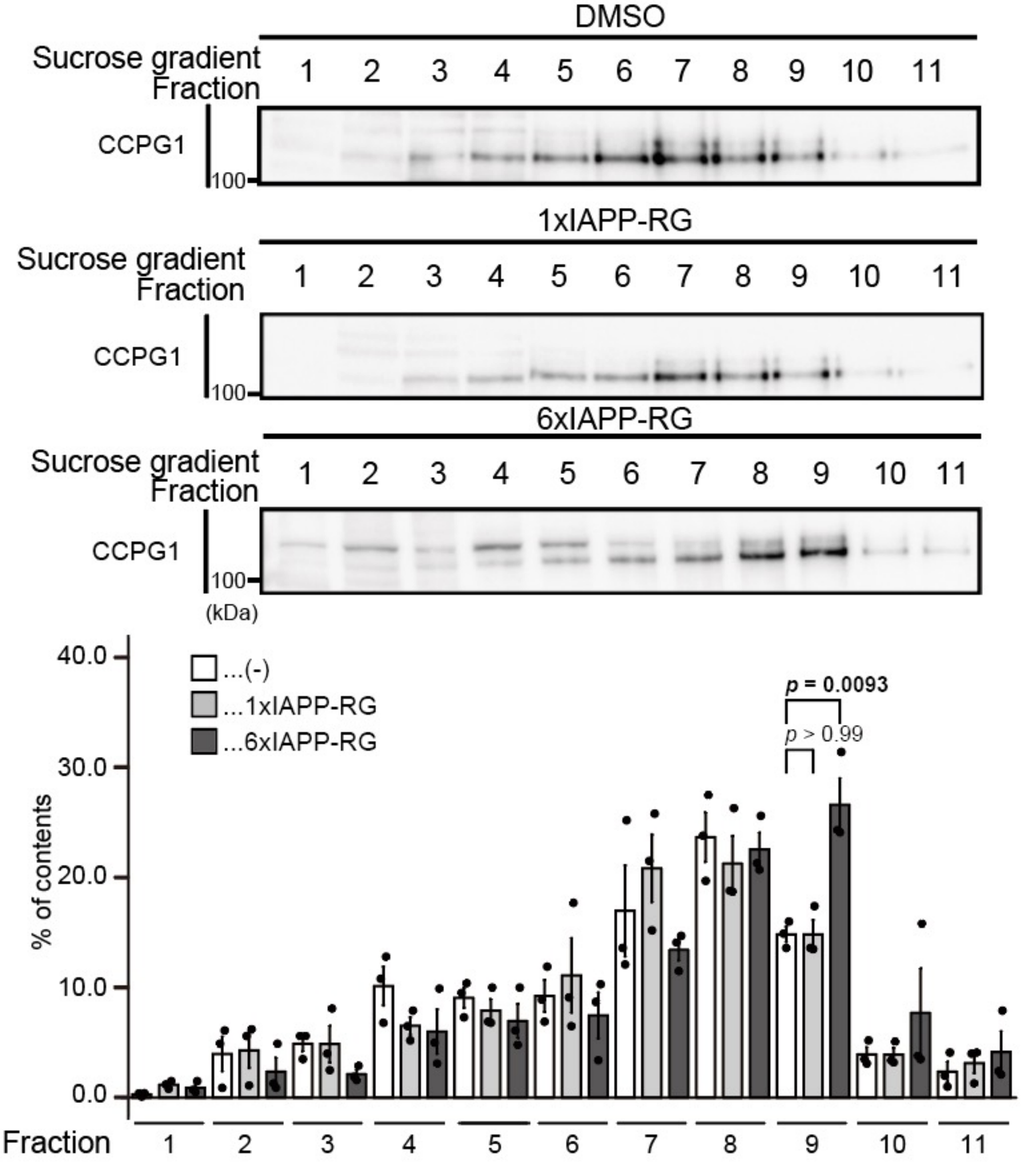

Figure 34. CCPG1 forms large molecular complexes in 6xIAPP-expressing cells.

Tet-On HeLa cells expressing 6x (or 1x) IAPP-RFP-GFP-KDEL were cultured with Dox for 48 h and lysed with CHAPS buffer. The lysates were fractionated on a discontinuous 10–50% sucrose gradient. Eleven fractions were collected, subjected to SDS-PAGE and analyzed through immunoblotting with antibodies against CCPG1. The band intensities were quantified using ImageJ (NIH, Bethesda, MD, USA). Data are represented as mean ± SE. Statistical analysis was performed by comparing each IAPP-RFP-GFP-KDEL to DMSO-treated samples. Differences were statistically analyzed by Dunnett's multiple comparison test.

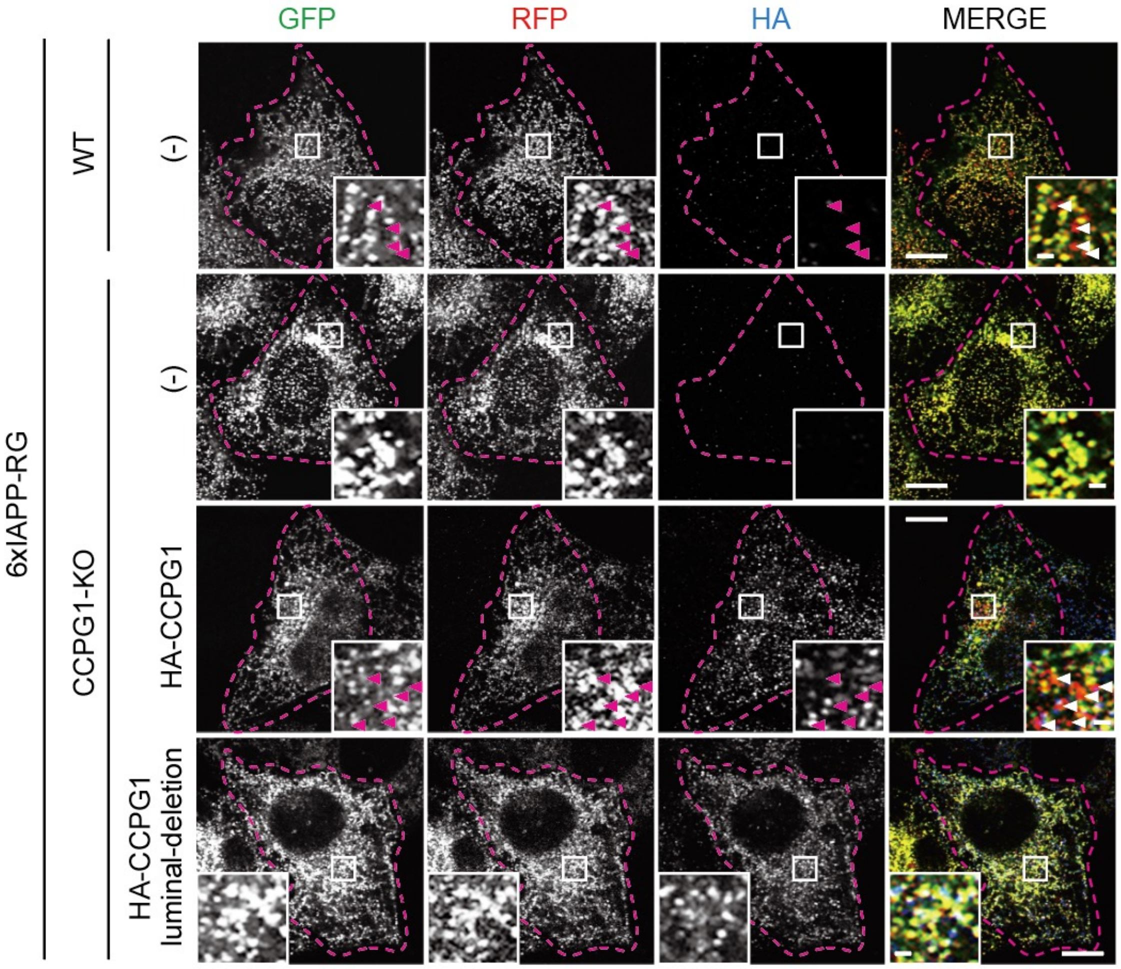

Figure 35. Lysosomal degradation of 6xIAPP-RFP-GFP-KDEL occurs in a manner dependent on the ER-luminal region of CCPG1.

WT and CCPG1-KO HeLa cells expressing 6xIAPP-RFP-GFP-KDEL, with or without exogenous HA-CCPG1 (full-length or luminal deletion mutant), were incubated in medium containing Dox and then subjected to immunofluorescence (IF). Cells treated with Dox as described above were fixed and stained with antibodies against HA-tag, and then analyzed using immunofluorescence microscopy. GFP-negative and RFP-positive signals (arrowhead) are indicated. Scale bars represent 10 and 1 μm (inset) .

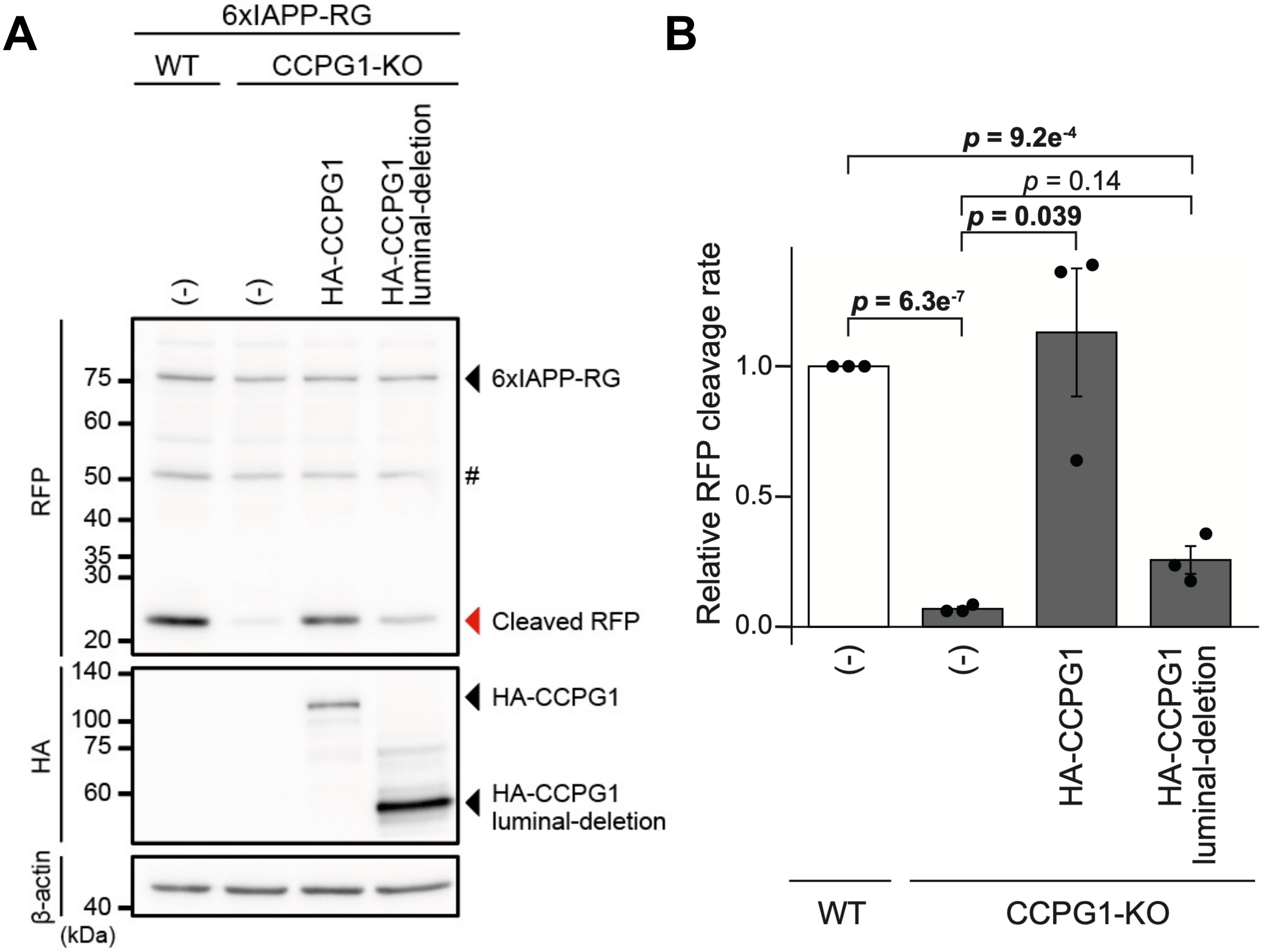

Figure 36. Lysosomal degradation of 6xIAPP-RFP-GFP-KDEL occurs in a manner dependent on the ER-luminal region of CCPG1.

WT and CCPG1-KO HeLa cells expressing 6xIAPP-RFP-GFP-KDEL, with or without exogenous HA-CCPG1 (full-length or luminal deletion mutant), were incubated in medium containing Dox and then subjected to immunoblotting. Lysates of each treatment were analyzed through immunoblotting using antibodies against RFP, HA, and β-actin (loading control) (A). The cells treated with Dox as described above were analyzed through immunoblotting. The band intensities of cleaved RFP and 6xIAPP-RFP-GFP-KDEL were quantified, and the ratio of cleaved RFP to 6xIAPP-RFP-GFP-KDEL (normalized to the WT) is shown. Data represent the mean ± SE of three independent experiments. Differences were statistically analyzed by one-way ANOVA and Sidak's multiple comparison test (B).

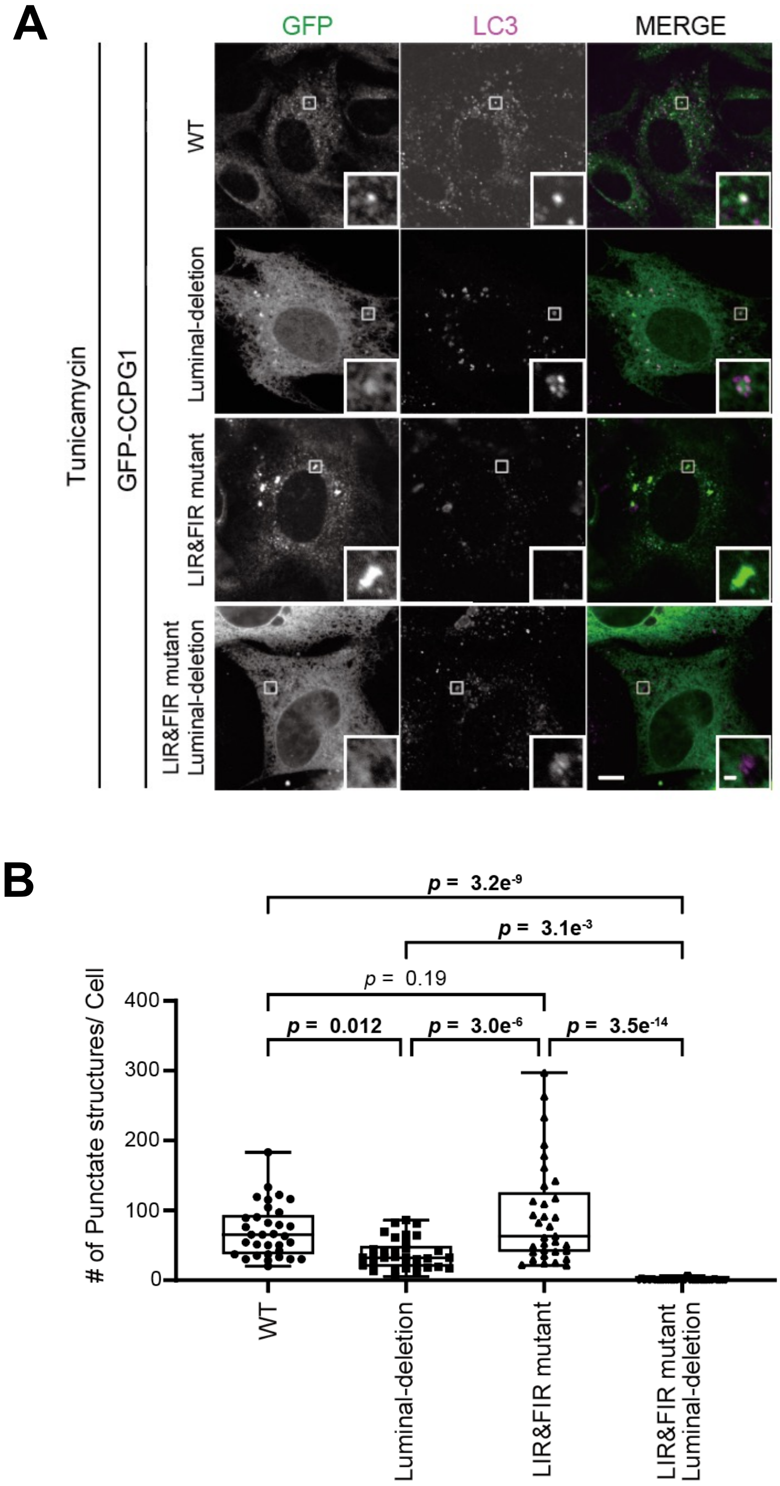

Figure 37. Mouse embryonic fibroblasts (MEFs) stably expressing GFP-CCPG1 and mutants were cultured under tunicamycin treatment and immunostained with anti-LC3 antibody. Scale bars represent 10 and 1 µm (insets) (A). Quantification of the number of CCPG1 puncta per cell. Solid bars indicate the median, boxes the interquartile range (25th–75th percentile), and whiskers the 0th–100th percentile range. Differences were analyzed using ANOVA and Sidak's multiple comparison test. Data were collected from 33 cells of each cell type (B).

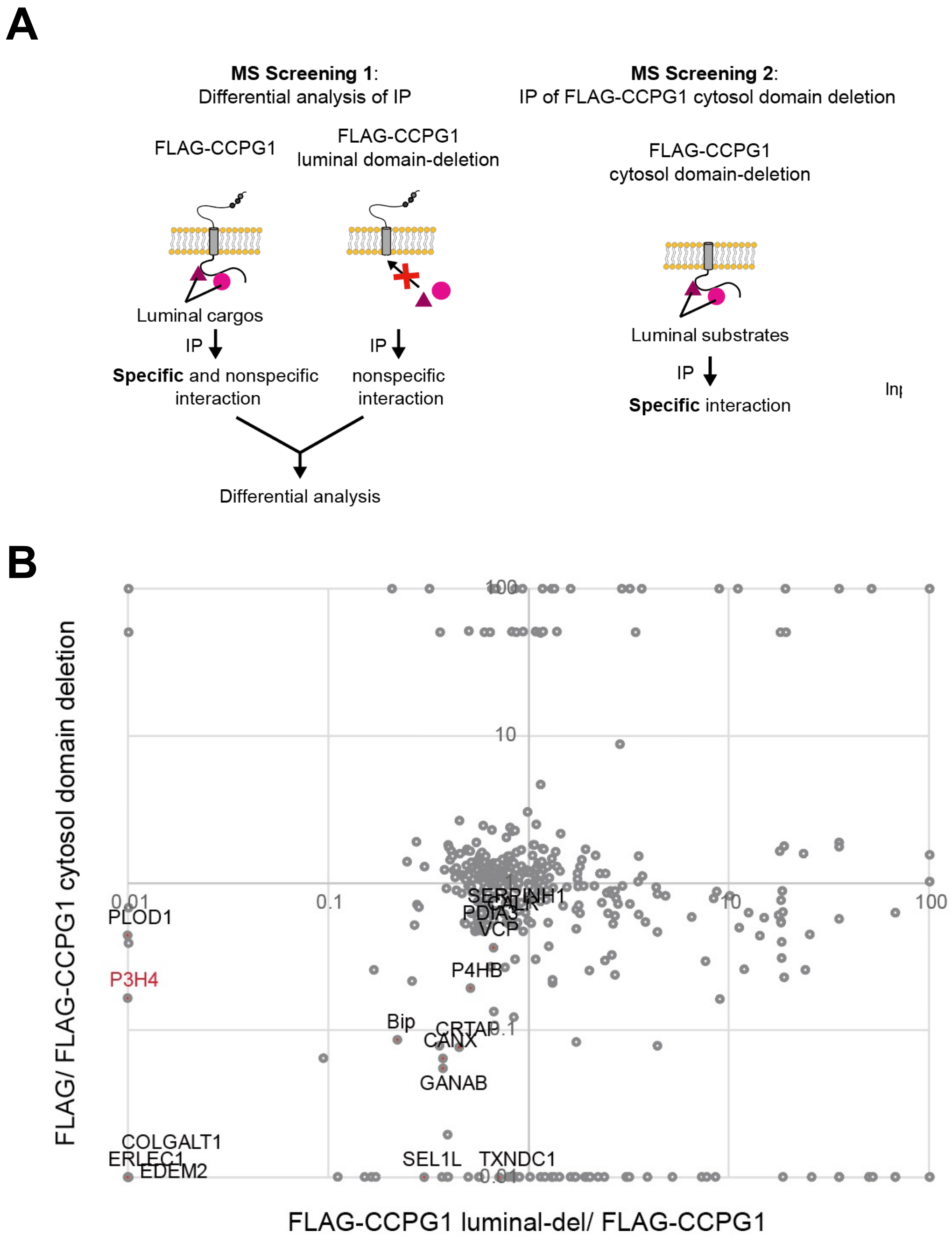

Figure 38. Strategy used to identify endogenous CCPG1 luminal domain-interacting proteins (A). Results of differential interactome screening. Two independent IP and MS analyses were conducted for each LC-MS/MS sample (B).

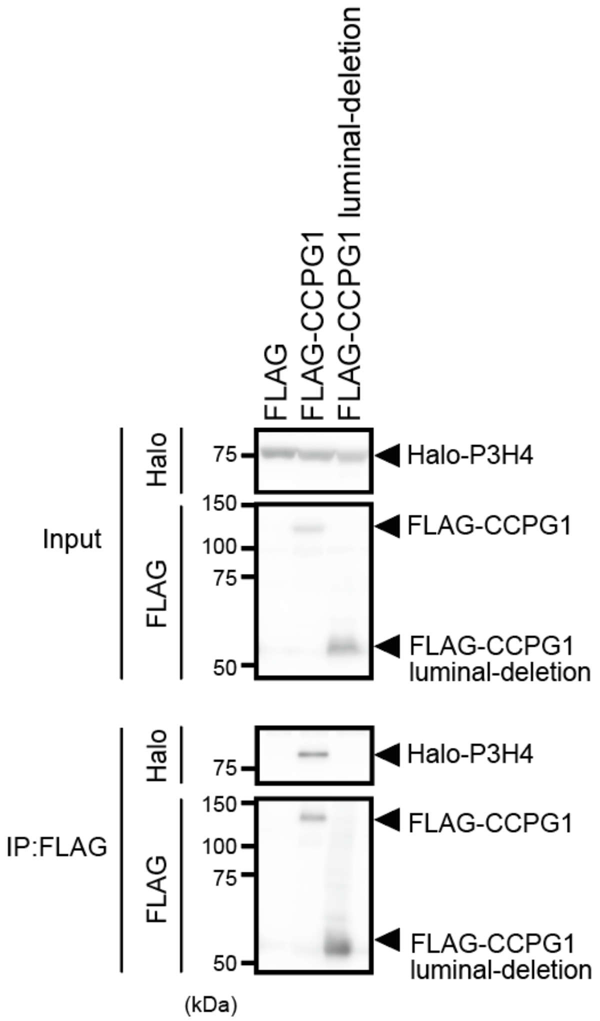

Figure 39. HEK293T cells transiently expressing ssHalo-P3H4 and WT, or mutated FLAG-CCPG1, were subjected to IP with anti-FLAG antibody and detection with anti-Halo and anti-FLAG antibodies.

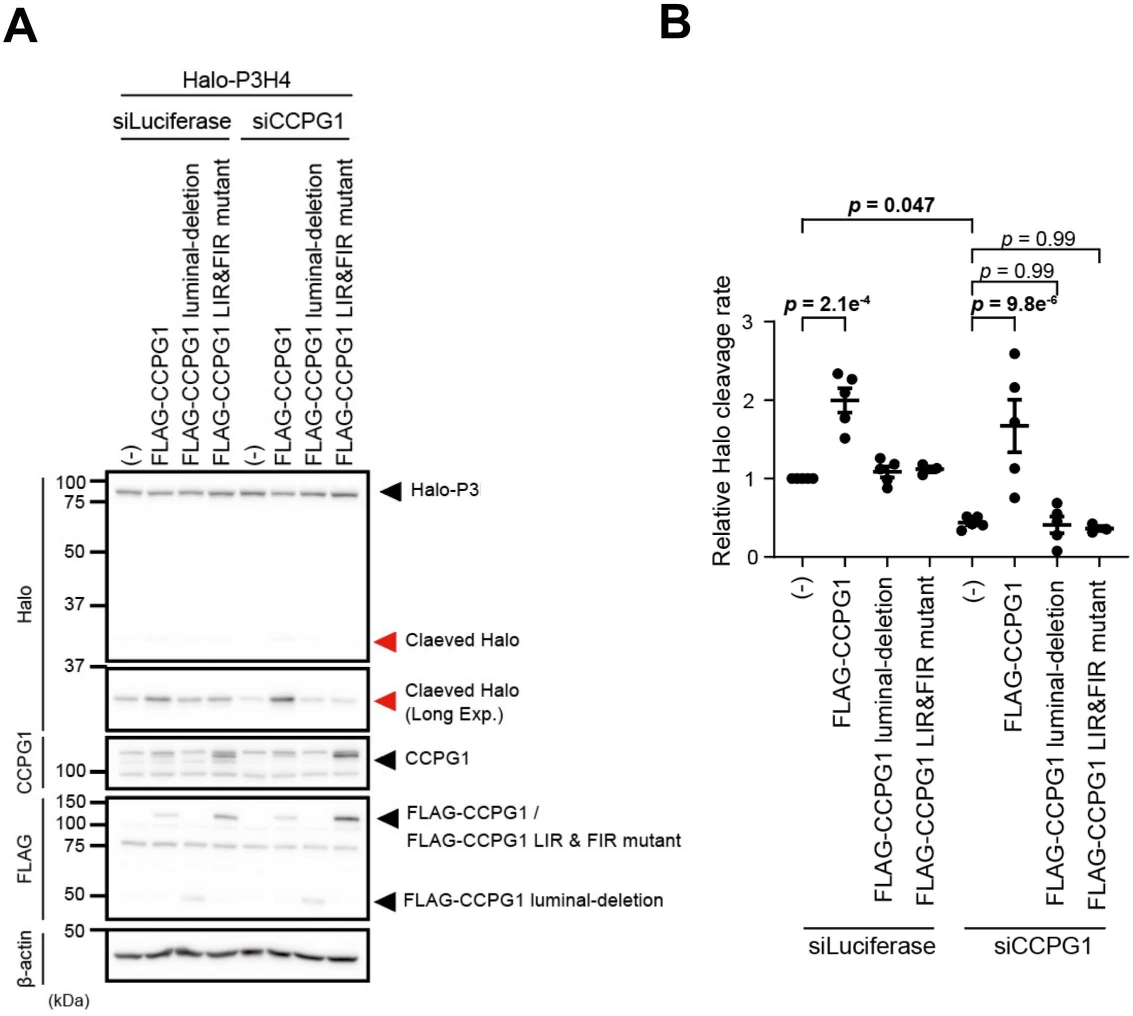

Figure 40. HeLa cells stably expressing ssHalo-P3H4 were transfected with the indicated siRNAs. After 3 days, cells were pulse-labeled for 1 h with 100 nM tetramethylrhodamine-conjugated ligand in nutrient-rich medium. The cells were incubated for 24 h and then collected. Cell lysates were analyzed through immunoblotting using the indicated antibodies (A). The band intensities of cleaved Halo and Halo-P3H4 were quantified, and the ratio of Halo to Halo-P3H4 (normalized to the WT) is shown. Data represent the mean ± SEM of five independent experiments. Differences were statistically analyzed by one-way ANOVA and Sidak's multiple comparison test (B).

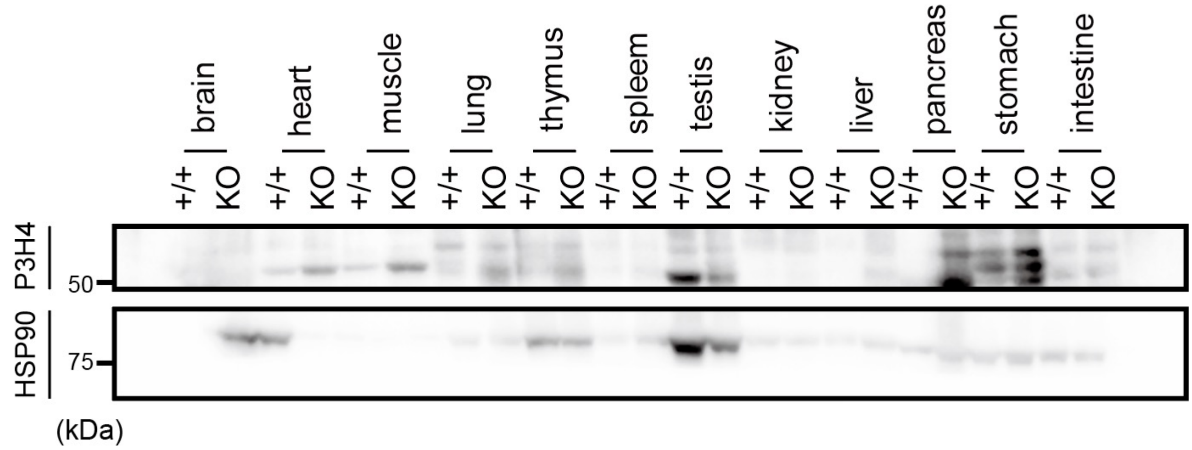

Figure 41. Immunoblotting of endogenous P3H4 in post-nuclear supernatants of the indicated organs from Atg5+/+;NSE-Atg5 (+/+) and Atg5−/−;NSE-Atg5 (KO) mice.

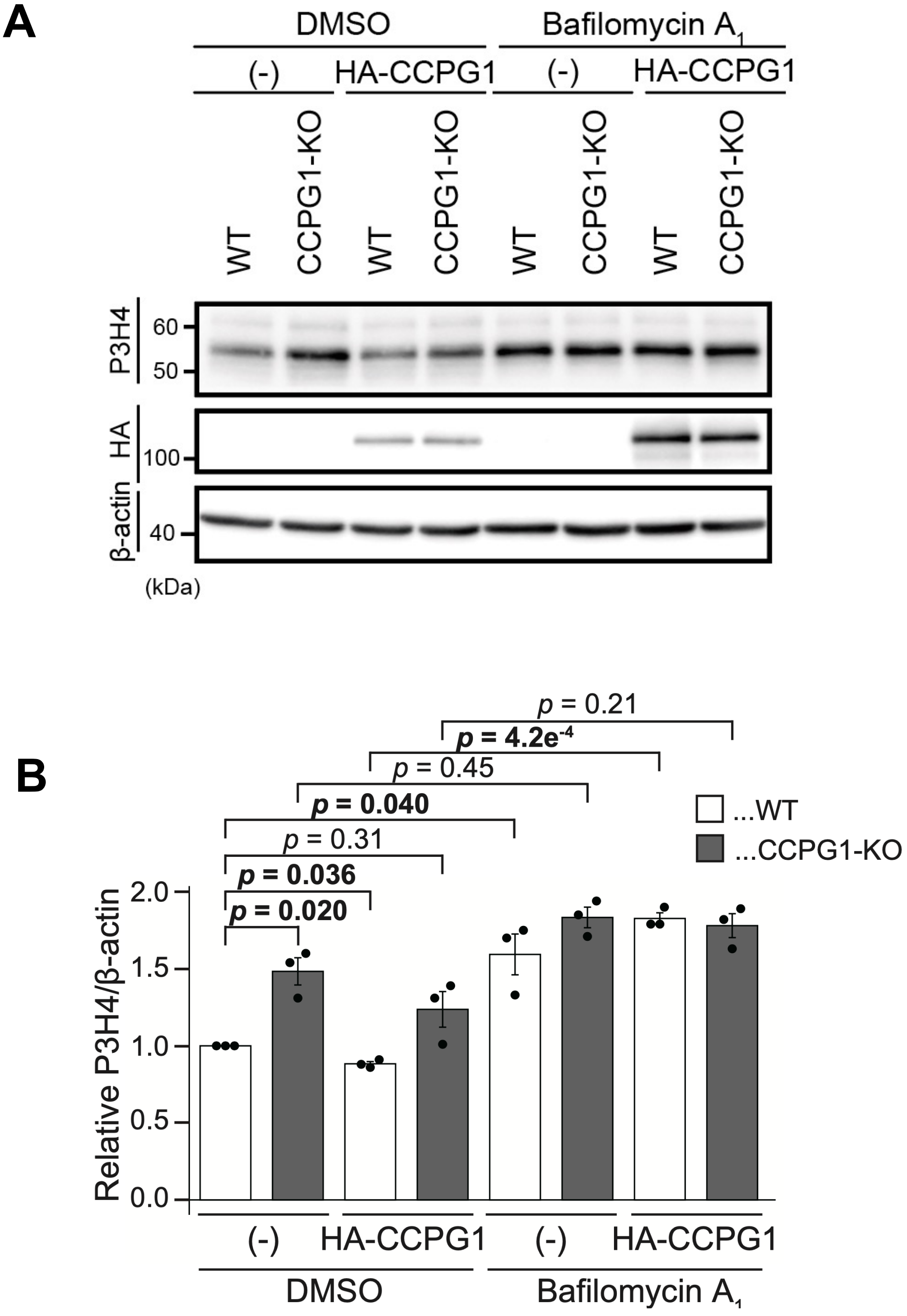

Figure 42. P3H4 accumulated in CCPG1-KO cells.

WT or CCPG1-KO cells with or without exogenous HA-CCPG1 were treated with DMSO or bafilomycin A_1 for 24 h. And then lysed with lysis buffer. Each cell lysate was analyzed through immunoblotting using antibodies against P3H4, HA-tag or β-actin (loading control). * indicates non-specific band (E). Band intensities were quantified and the ratio of P3H4 to β-actin (normalized to the WT) is shown. Data represent the mean ± SE. Differences were analyzed using one-way ANOVA and Sidak's multiple comparison test

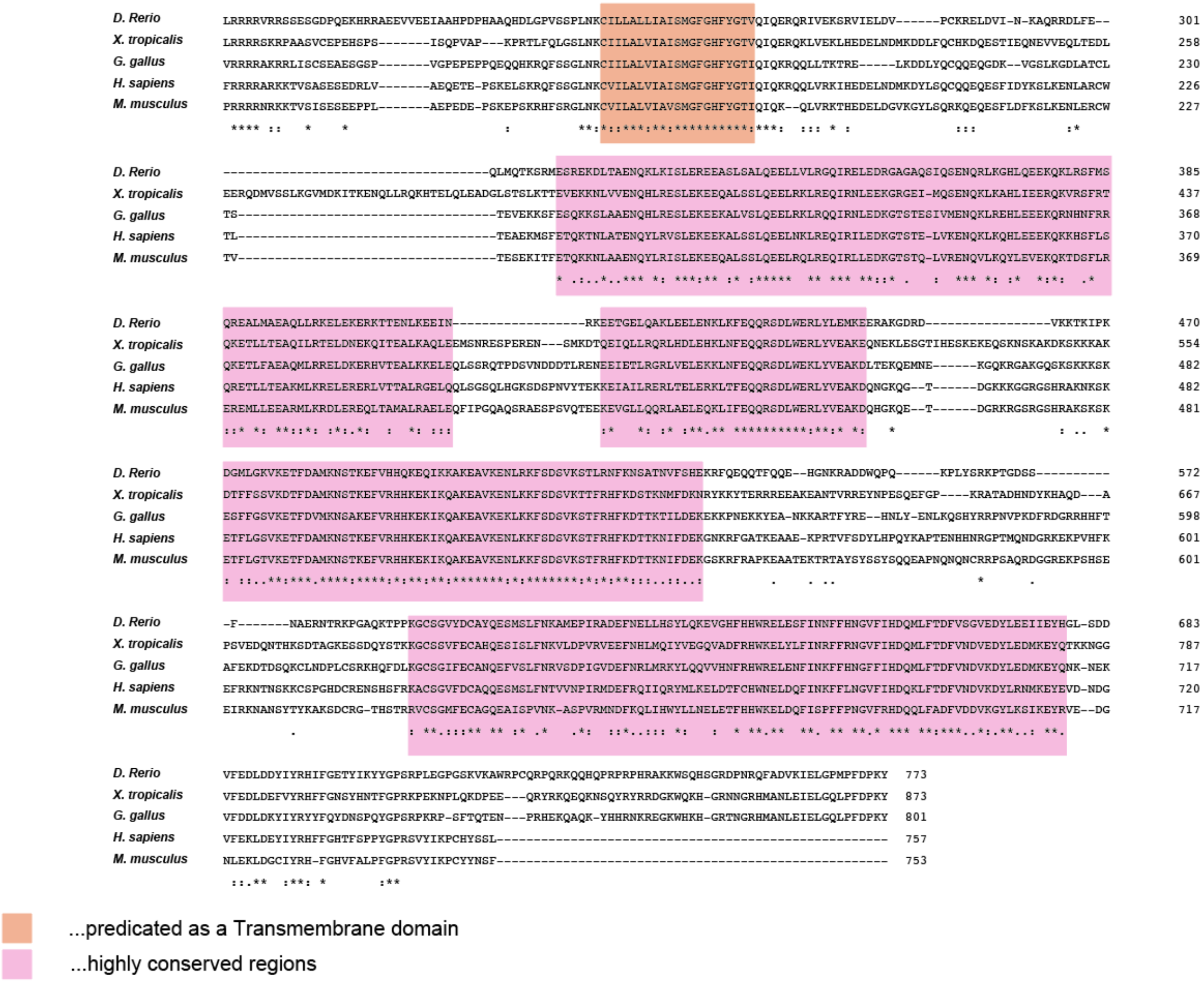

```
D. Rerio      LRRRRVRRSSESGDPQEKHRRAEEVVEEIAAHPDPHAAQHDLGPVSSPLNKCILLALLIAISMGFGHFYGTVQIQERQRIVEKSRVIELDV------PCKRELDVI-N-KAQRRDLFE--    301
X. tropicalis LRRRRSKRPAASVCEPEHSPS-------ISQPVAP---KPRTLFQLGSLNKCIILALVIAISMGFGHFYGTVQIQERQKLVEKLHEDELNDMKDDLFQCHKDQESTIEQNEVVEQLTEDL    258
G. gallus     VRRRRAKRRLISCSEAESGSP-------VGPEPEPPQEQQHKRQFSSGLNRCIILALVIAISMGFGHFYGTIQIQKRQQLLTKTRE-----LKDDLYQCQQEQGDK--VGSLKGDLATCL    230
H. sapiens    FRRRRARKKTVSASESEDRLV-------AEQETE-PSKELSKRQFSSGLNKCVILALVIAISMGFGHFYGTIQIQKRQQLVRKIHEDELNDMKDYLSQCQQEQESFIDYKSLKENLARCW    226
M. musculus   PRRRRNRKKTVSISESEEPPL-------AEPEDE-PSKEPSKRHFSRGLNKCVILALVIAVSMGFGHFYGTIQIQK--QLVRKTHEDELDGVKGYLSQRKQEQESFLDFKSLKENLERCW    227
               **** ::   *    *                     :         **:*::***:**:**********:***:  ::: * :              :::            :*

D. Rerio      ------------------------------------QLMQTKSRMESREKDLTAENQKLKISLEREEASLSALQEELLVLRGQIRELEDRGAGAQSIQSENQRLKGHLQEEKQKLRSFMS    385
X. tropicalis EERQDMVSSLKGVMDKITKENQLLRQKHTELQLEADGLSTSLKTTEVEKKNLVVENQHLRESLEKEEQALSSLQEELRKLREQIRNLEEKGRGEI-MQSENQKLKAHLIEERQKVRSFRT    437
G. gallus     TS-----------------------------------TEVEKKSFESQKKSLAAENQHLRESLEKEEKALVSLQEELRKLRQQIRNLEDKGTSTESIVMENQKLREHLEEEKQRNHNFRR    368
H. sapiens    TL-----------------------------------TEAEKMSFETQKTNLATENQYLRVSLEKEEKALSSLQEELNKLREQIRILEDKGTSTE-LVKENQKLKQHLEEEKQKKHSFLS    370
M. musculus   TV-----------------------------------TESEKITFETQKKNLAAENQYLRISLEKEEQALSSLQEELRQLREQIRLLEDKGTSTQ-LVRENQVLKQYLEVEKQKTDSFLR    369
                                                           * .:..*..*** *: ***:** :* :*****  ** *** **::* .   :  *** *: :*  *:*:  .*

D. Rerio      QREALMAEAQLLRKELEKERKTTENLKEEIN------------------RKEETGELQAKLEELENKLKFEQQRSDLWERLYLEMKEERAKGDRD-----------------VKKTKIPK    470
X. tropicalis QKETLLTEAQILRTELDNEKQITEALKAQLEEMSNRESPEREN---SMKDTQEIQLLRQRLHDLEHKLNFEQQRSDLWERLYVEAKEQNEKLESGTIHESKEKEQSKNSKAKDKSKKKAK    554
G. gallus     QKETLFAEAQMLRRELDKERHVTEALKKELEQLSSRQTPDSVNDDDTLRENEEIETLRGRLVELEKKLNFEQQRSDLWEKLYVEAKDLTEKQEMNE------KGQKRGAKGQSKSKKKSK    482
H. sapiens    QRETLLTEAKMLKRELERERLVTTALRGELQQLSGSQLHGKSDSPNVYTEKKEIAILRERLTELERKLTFEQQRSDLWERLYVEAKDQNGKQG--T------DGKKKGGRGSHRAKNKSK    482
M. musculus   EREMLLEEARMLKRDLEREQLTAMALRAELEQFIPGQAQSRAESPSVQTEEKEVGLLQQRLAELEQKLIFEQQRSDLWERLYVEAKDQHGKQE--T------DGRKRGSRGSHRAKSKSK    481
              ::* *: **::*: :*:.*:  :  *: :::                    :*   *: :* :**.** **********:**:* *:   *                      : ..  *

D. Rerio      DGMLGKVKETFDAMKNSTKEFVHHQKEQIKKAKEAVKENLRKFSDSVKSTLRNFKNSATNVFSHEKRFQEQQTFQQE--HGNKRADDWQPQ------KPLYSRKPTGDSS----------    572
X. tropicalis DTFFSSVKDTFDAMKNSTKEFVRHHKEKIKQAKEAVKENLKKFSDSVKTTFRHFKDSTKNMFDKNRYKKYTERRREEAKEANTVRREYNPESQEFGP----KRATADHNDYKHAQD---A    667
G. gallus     ESFFGSVKETFDVMKNSAKEFVRHHKEKIKQAKEAVKEKLKKFSDSVKSTFRHFKDTTKTILDEKEKKPNEKKYEA-NKKARTFYRE--HNLY-ENLKQSHYRRPNVPKDFRDGRRHHFT    598
H. sapiens    ETFLGSVKETFDAMKNSTKEFVRHHKEKIKQAKEAVKENLKKFSDSVKSTFRHFKDTTKNIFDEKGNKRFGATKEAAE-KPRTVFSDYLHPQYKAPTENHHNRGPTMQNDGRKEKPVHFK    601
M. musculus   ETFLGTVKETFDAMKNSTKEFVRHHKEKIKQAKEAVKENLKKFSDSVKSTFRHFKDTTKNIFDEKGSKRFRAPKEAATEKTRTAYSYSSYSQQEAPNQNQNCRRPSAQRDGGREKPSHSE    601
              : ::..**:***.****:****:*:**:**:*******:*:*******:*:*:**:::..::..:         .    . ..                   *      .

D. Rerio      -F-------NAERNTRKPGAQKTPPKGCSGVYDCAYQESMSLFNKAMEPIRADEFNELLHSYLQKEVGHFHHWRELESFINNFFHNGVFIHDQMLFTDFVSGVEDYLEEIIEYHGL-SDD    683
X. tropicalis PSVEDQNTHKSDTAGKESSDQYSTKKGCSSVFECAHQESISLFNKVLDPVRVEEFNHLMQIYVEGQVADFRHWKELYLFINRFFRNGVFIHDQMLFTDFVNDVEDYLEDMKEYQTKKNGG    787
G. gallus     AFEKDTDSQKCLNDPLCSRKHQFDLKGCSGIFECANQEFVSLFNRVSDPIGVDEFNRLMRKYLQQVVHNFRHWRELENFINKFFHNGFFIHDQMLFTDFVNDVKDYLEDMKEYQNK-NEK    717
H. sapiens    EFRKNTNSKKCSPGHDCRENSHSFRKACSGVFDCAQQESMSLFNTVVNPIRMDEFRQIIQRYMLKELDTFCHWNELDQFINKFFLNGVFIHDQKLFTDFVNDVKDYLRNMKEYEVD-NDG    720
M. musculus   EIRKNANSYTYKAKSDCRG-THSTRRVCSGMFECAGQEAISPVNK-ASPVRMNDFKQLIHWYLLNELETFHHWKELDQFISPFFPNGVFRHDQQLFADFVDDVKGYLKSIKEYRVE--DG    717
                       .               : **.:::** ** :* .*   .*:  ::*..::: *:   :  * **.**  **. ** **.* *** **:***..*:.**..: **.

D. Rerio      VFEDLDDYIYRHIFGETYIKYYGPSRPLEGPGSKVKAWRPCQRPQRKQQHQPRPRPHRAKKWSQHSGRDPNRQFADVKIELGPMPFDPKY    773
X. tropicalis VFEDLDEFVYRHFFGNSYHNTFGPRKPEKNPLQKDPEE---QRYRKQEQKNSQYRYRRDGKWQKH-GRNNGRHMANLEIELGQLPFDPKY    873
G. gallus     VFDDLDKYIYRYYFQYDNSPQYGPSRPKRP-SFTQTEN---PRHEKQAQK-YHHRNKREGKWHKH-GRTNGRHMANLEIELGQLPFDPKY    801
H. sapiens    VFEKLDEYIYRHFFGHTFSPPYGPRSVYIKPCHYSSL-----------------------------------------------------    757
M. musculus   NLEKLDGCIYRH-FGHVFALPFGPRSVYIKPCYYNSF-----------------------------------------------------    753
               ::.**  :**: *       :**
```

🟧 ...predicated as a Transmembrane domain

🟪 ...highly conserved regions

Figure 43. Sequence alignment of the ER luminal region of CCPG1 among vertebrate orthologs.

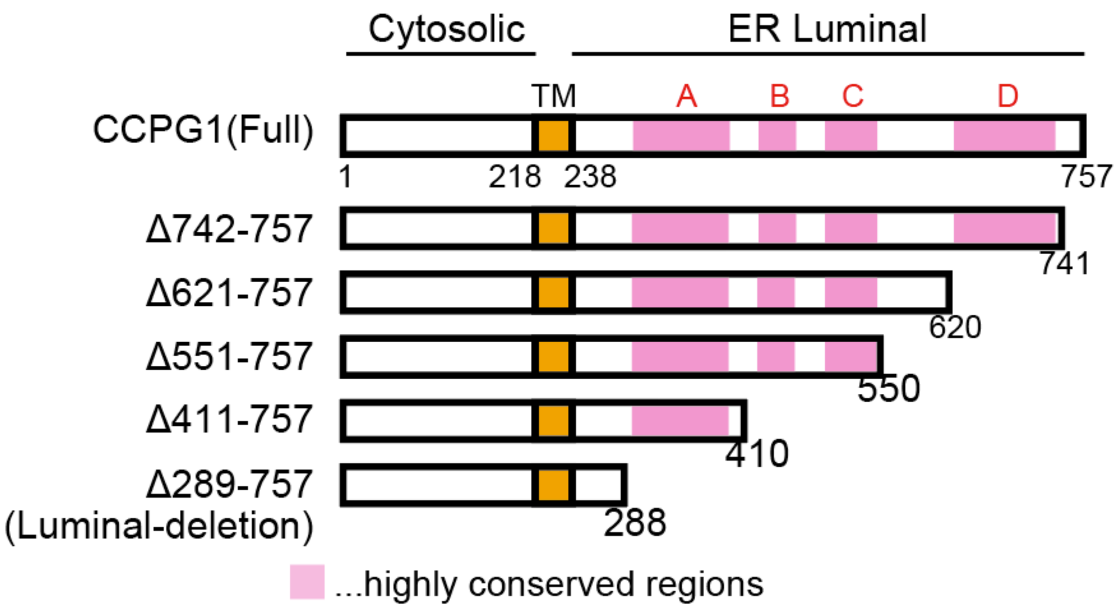

Figure 44. Diagram of the truncated mutants of CCPG1.

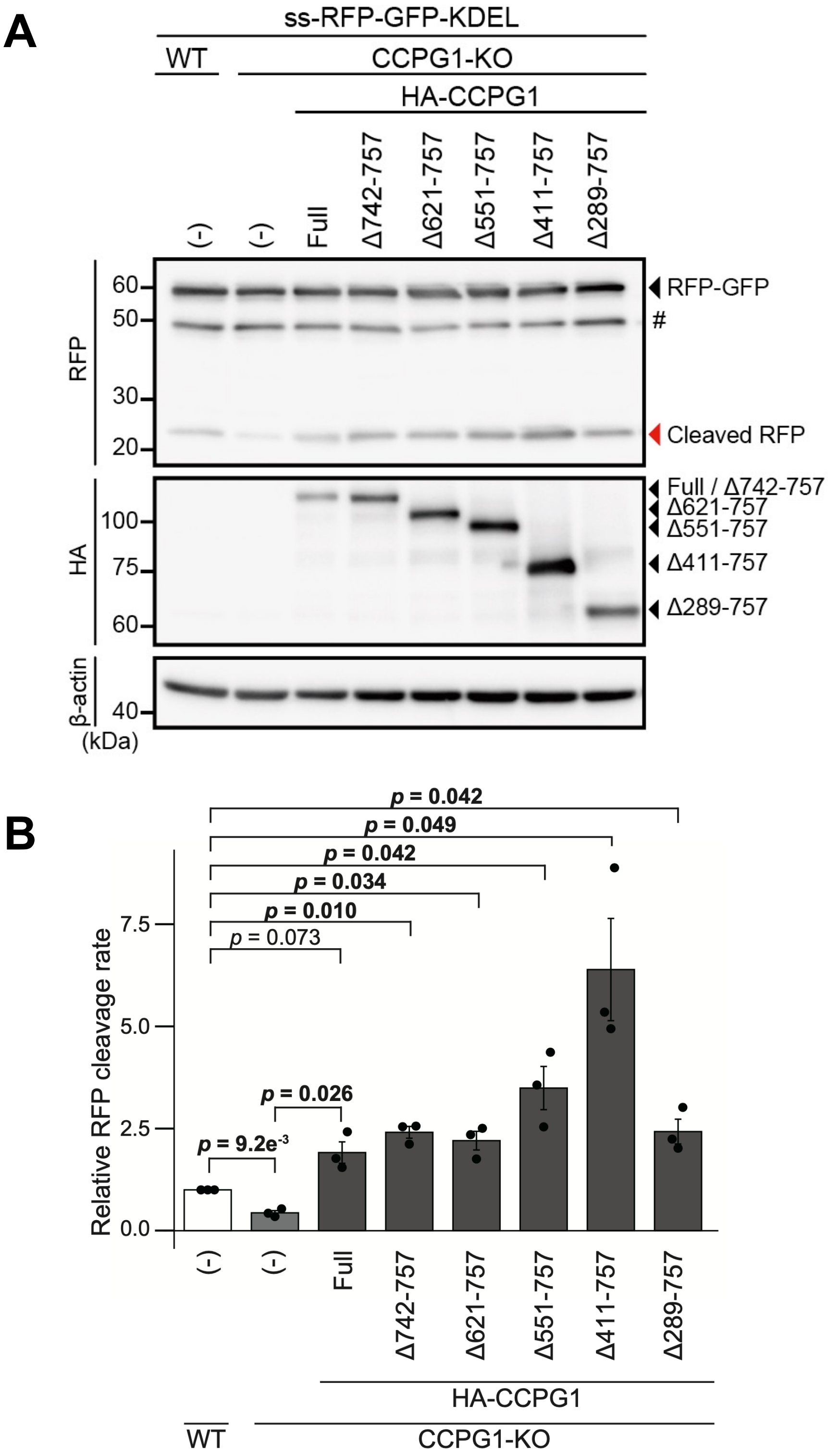

Figure 45. Overexpression of the ER luminal deletion mutant of CCPG1 restores bulk ER-phagy.

WT and CCPG1-KO HeLa cells co-expressing ER luminal deletion mutants (Δ742–757, Δ621–757, Δ551–757, Δ411–757, and Δ289–757) of CCPG1 (constitutive) and ss-RFP-GFP-KDEL (Tet-On) were incubated with Dox for 48 h and then subjected to immunoblotting (A). The band intensities of cleaved RFP and RFP-GFP were quantified using ImageJ, and the ratio of cleaved RFP to RFP-GFP (normalized to the WT) is shown. Data represent the mean ± SE of three independent experiments. Differences were analyzed using one-way ANOVA and Sidak's multiple comparison test (B).

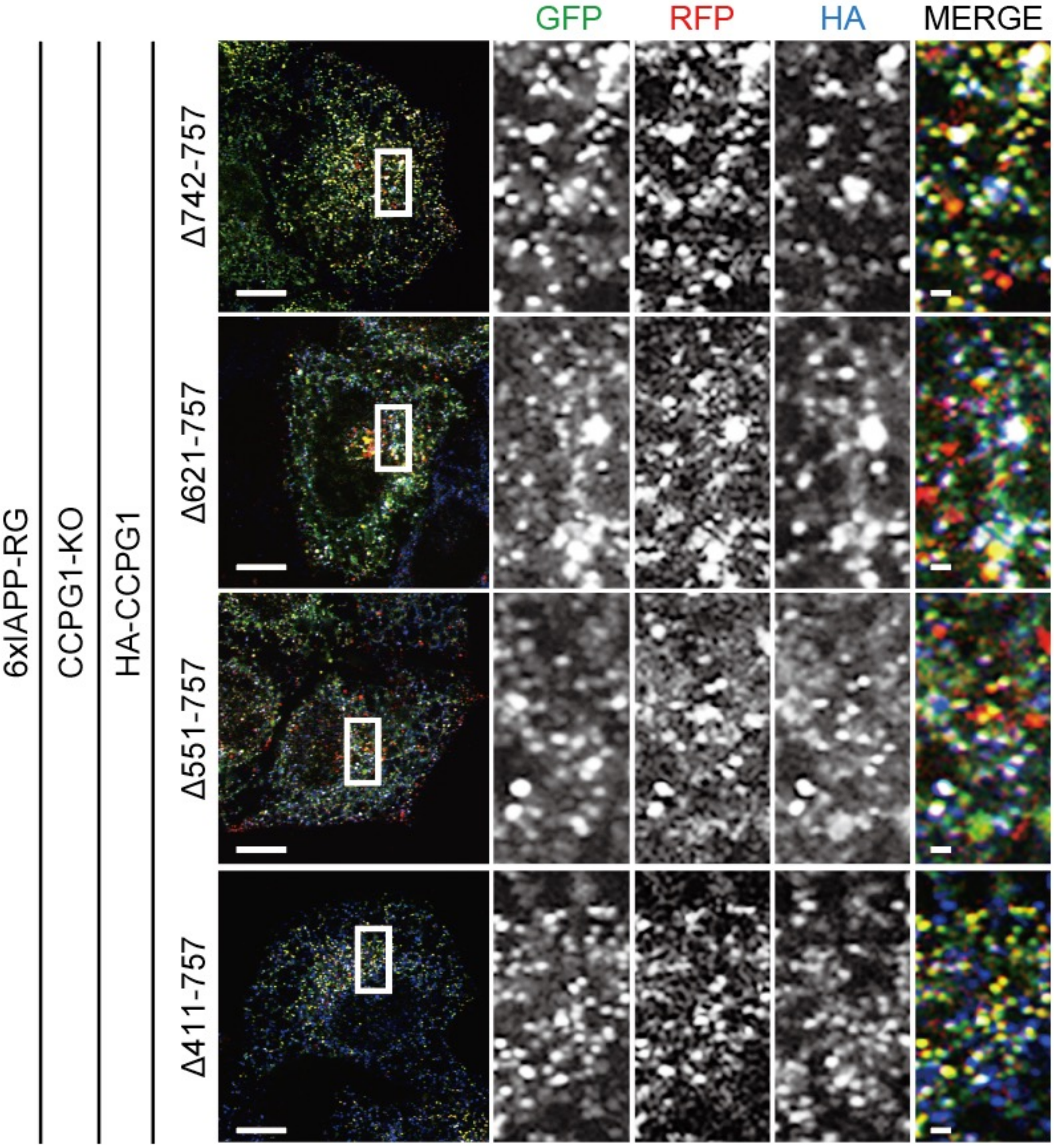

Figure 46. The ER luminal region of CCPG1 at 411–757 aa is required for lysosomal degradation of 6xIAPP.

CCPG1 KO HeLa cells co-expressing the indicated CCPG1 mutants (constitutive) and 6xIAPP-RFP-GFP-KDEL (Tet-On) were incubated with medium containing Dox for 48 h and subjected to IF and immunoblotting. Cells were stained with antibodies against HA-tag and analyzed through immunofluorescence microscopy. Scale bars represent 10 and 1 μm (inset).

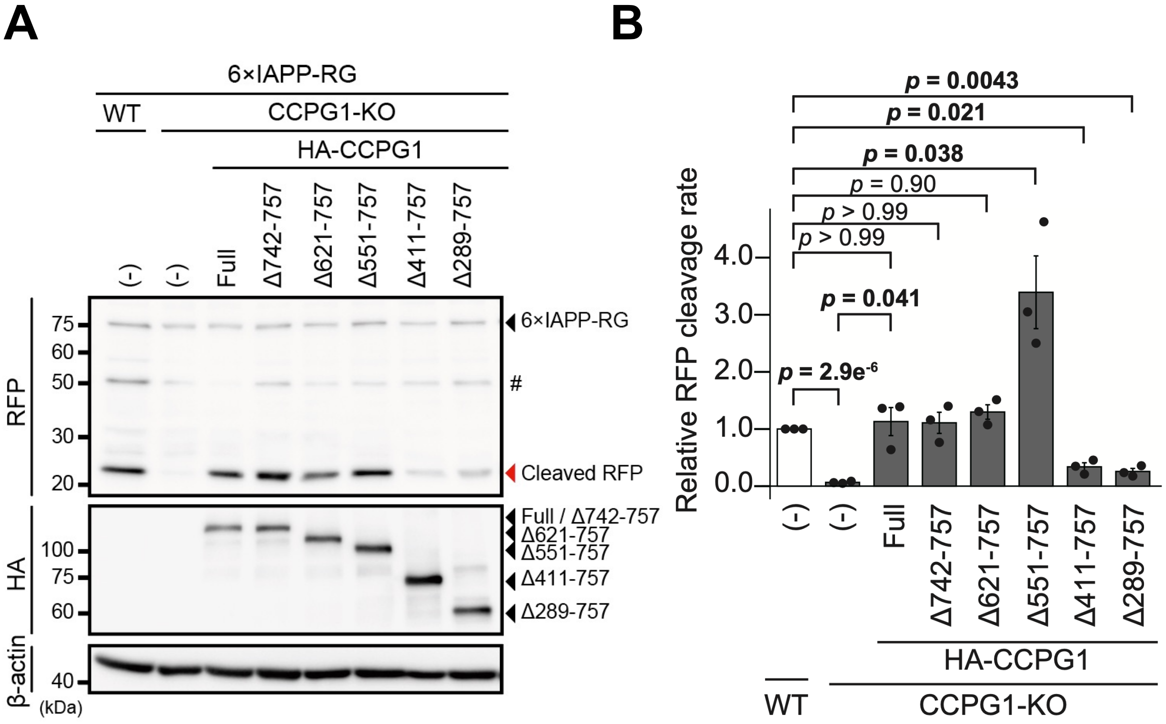

Figure 47. The ER luminal region of CCPG1 at 411–757 aa is required for lysosomal degradation of 6xIAPP.

Cell lysates were analyzed through immunoblotting with antibodies against RFP, HA-tag, and β-actin (loading control) (A). The band intensities of cleaved RFP and 6xIAPP-RFP-GFP-KDEL were quantified and the ratio of cleaved RFP to 6xIAPP-RFP-GFP-KDEL (normalized to the WT) is shown. Data represent the mean ± SE of three independent experiments. Differences were analyzed using one-way ANOVA and Sidak's multiple comparison test (B).

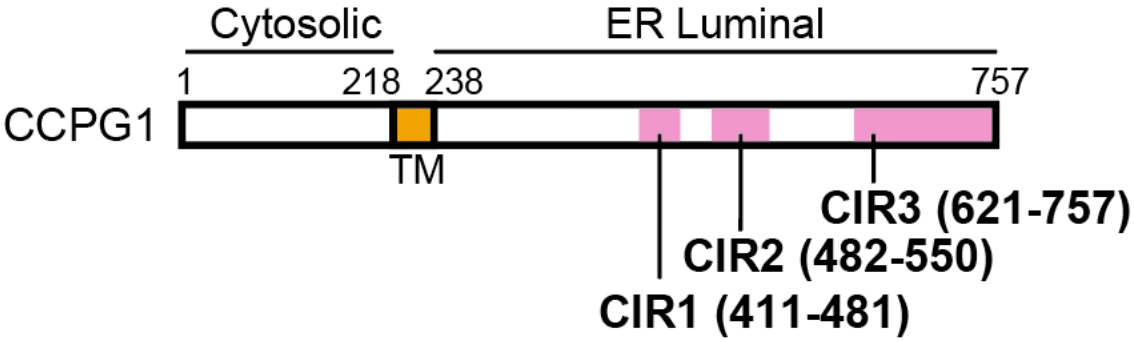

Figure 48. Diagram of cargo interacting region (CIR) mutants of CCPG1.

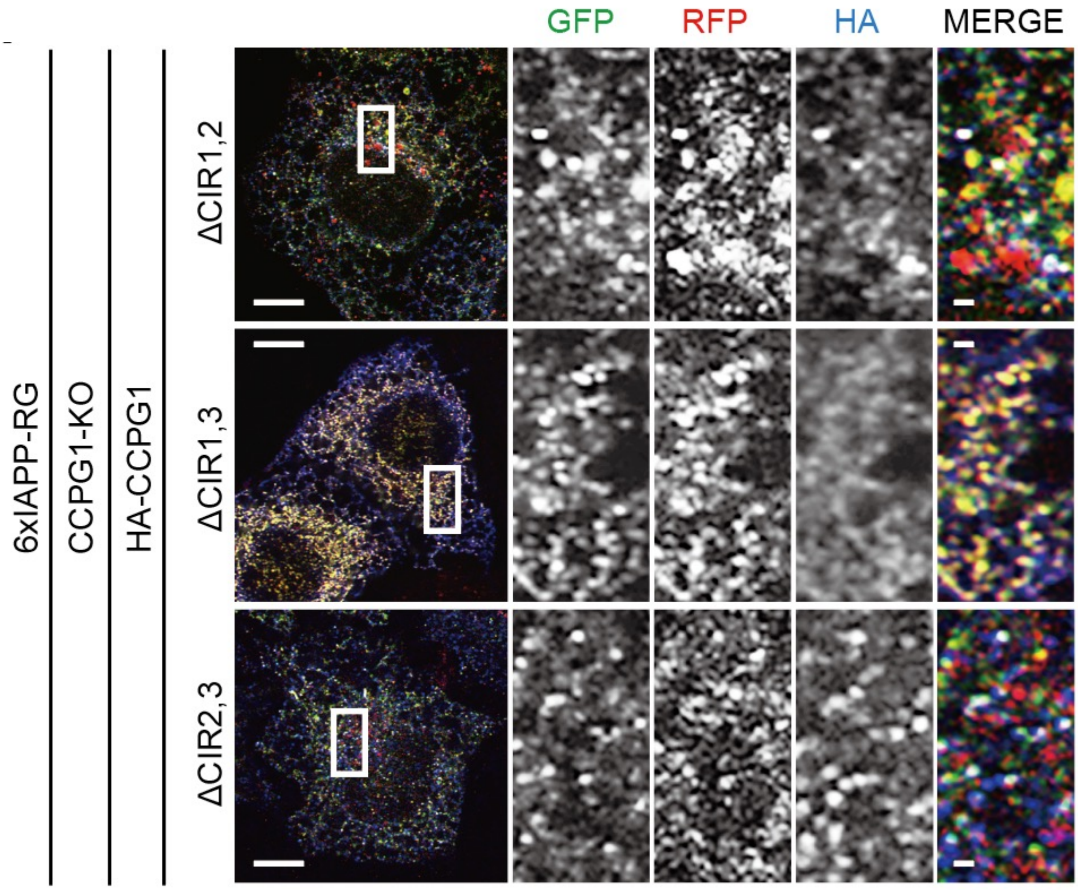

Figure 49. Both CIR1 and CIR3 of CCPG1 are required for lysosomal degradation of 6xIAPP.

Tet-On WT HeLa cells and CCPG1 KO HeLa cells co-expressing the indicated CIR mutants of CCPG1 (stably) and 6xIAPP-RFP-GFP-KDEL (Tet-On) were cultured with Dox for 48 h and then subjected to IF and immunoblotting. Cells were stained with antibodies against HA-tag and analyzed through immunofluorescence microscopy. Scale bars represent 10 and 1 µm (inset).

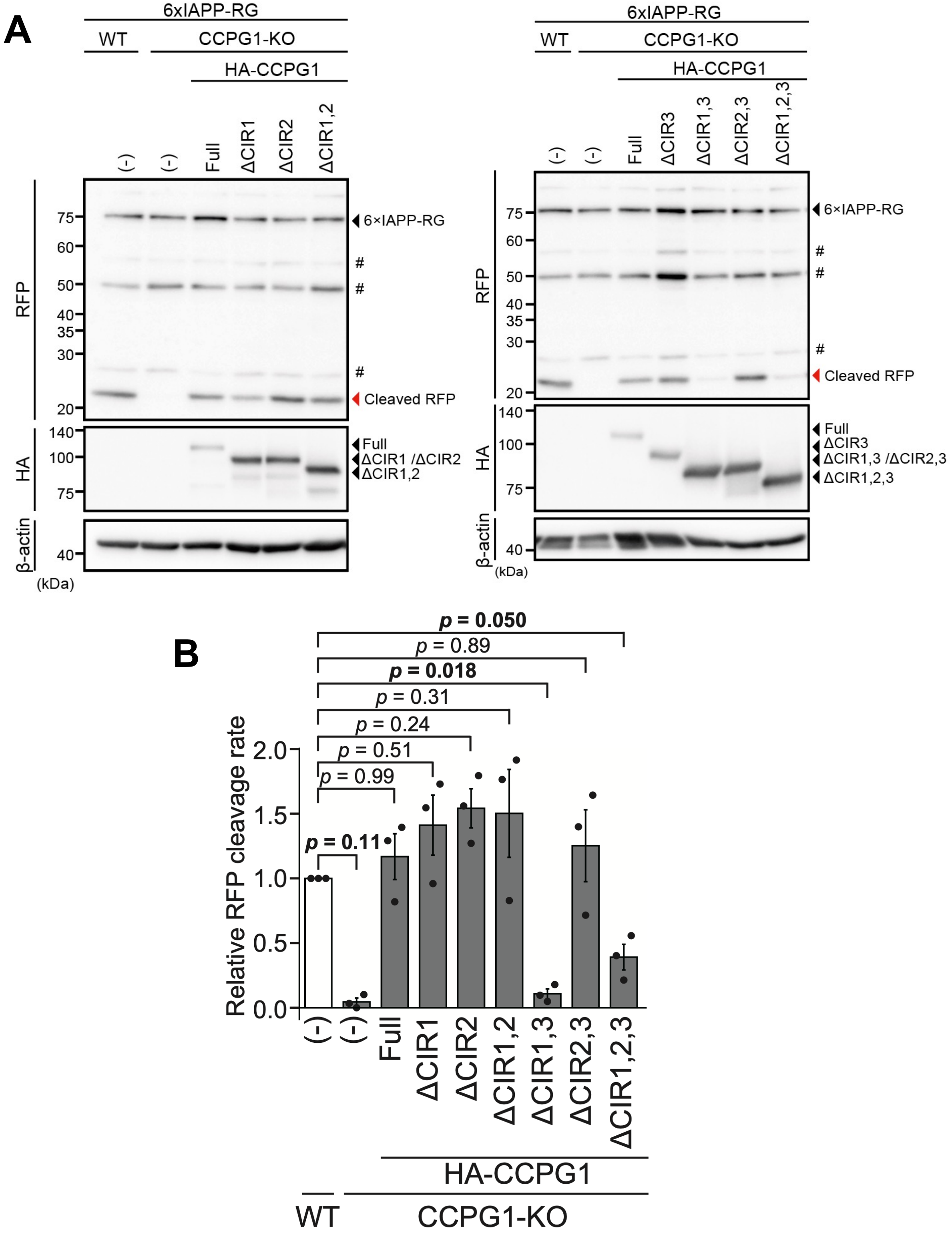

Figure 50. Both CIR1 and CIR3 of CCPG1 are required for lysosomal degradation of 6xIAPP.

Cell lysates were analyzed through immunoblotting using antibodies against RFP, HA-tag, and β-actin (loading control) (A). Band intensities of cleaved RFP and 6xIAPP-RFP-GFP-KDEL were quantified and the ratio of cleaved RFP to 6xIAPP-RFP-GFP-KDEL (normalized to the WT) is shown. Data represent the mean ± SE of three independent experiments. Differences were statistically analyzed by Dunnett's multiple comparison test (B)

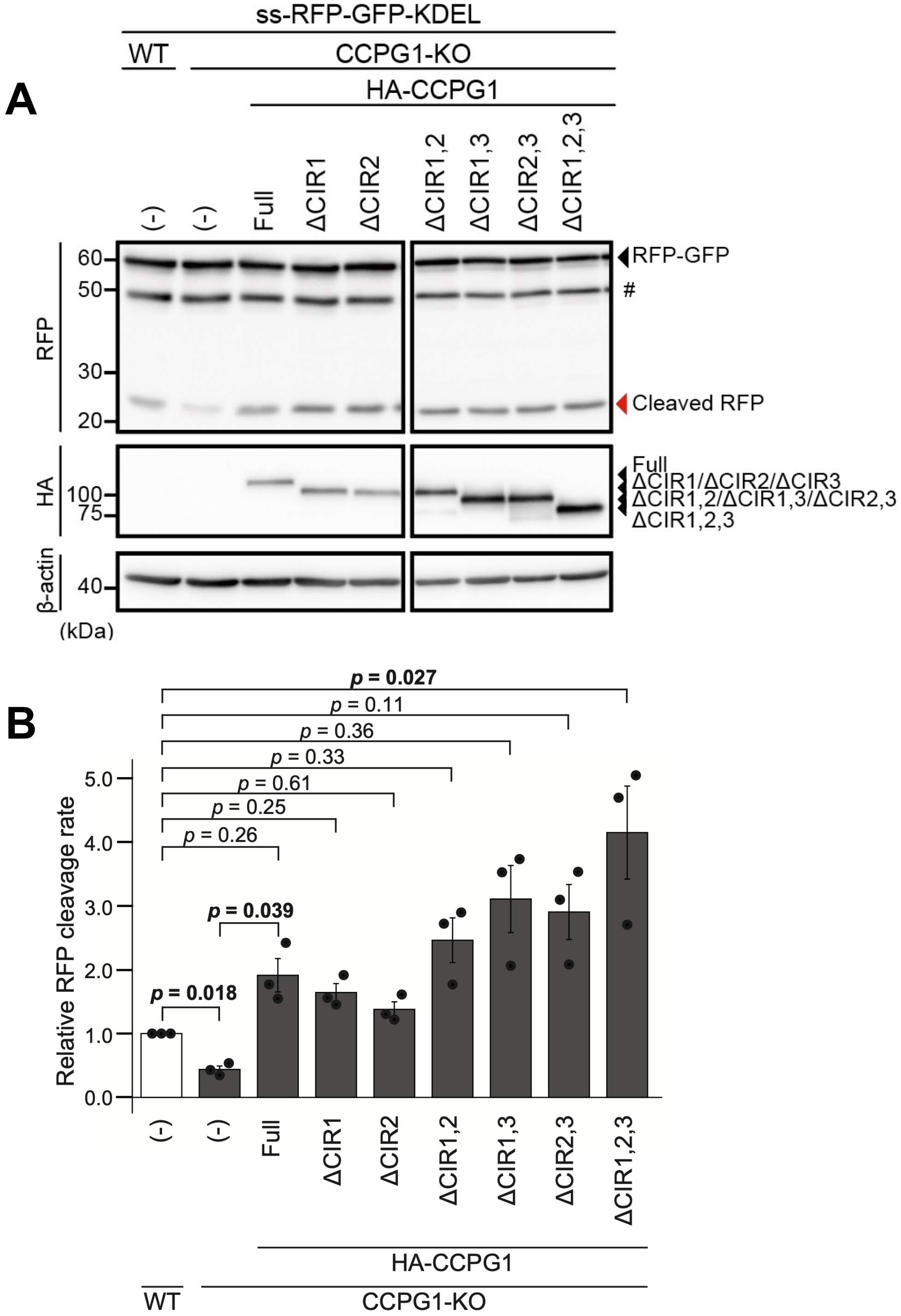

Figure 51. Overexpression of the ER luminal deletion mutant of CCPG1 restores bulk ER-phagy.

WT and CCPG1-KO HeLa cells co-expressing ER luminal deletion mutants (ΔCIR1, ΔCIR2, ΔCIR1,2, ΔCIR1,3, ΔCIR2,3, and ΔCIR1,2,3) of CCPG1 (constitutive) and ss-RFP-GFP-KDEL (Tet-On) were incubated with Dox for 48 h and then subjected to immunoblotting (A). The band intensities of cleaved RFP and RFP-GFP were quantified using ImageJ, and the ratio of cleaved RFP to RFP-GFP (normalized to the WT) is shown. Data represent the mean ± SE of three independent experiments. Differences were analyzed using one-way ANOVA and Sidak's multiple comparison test (B).

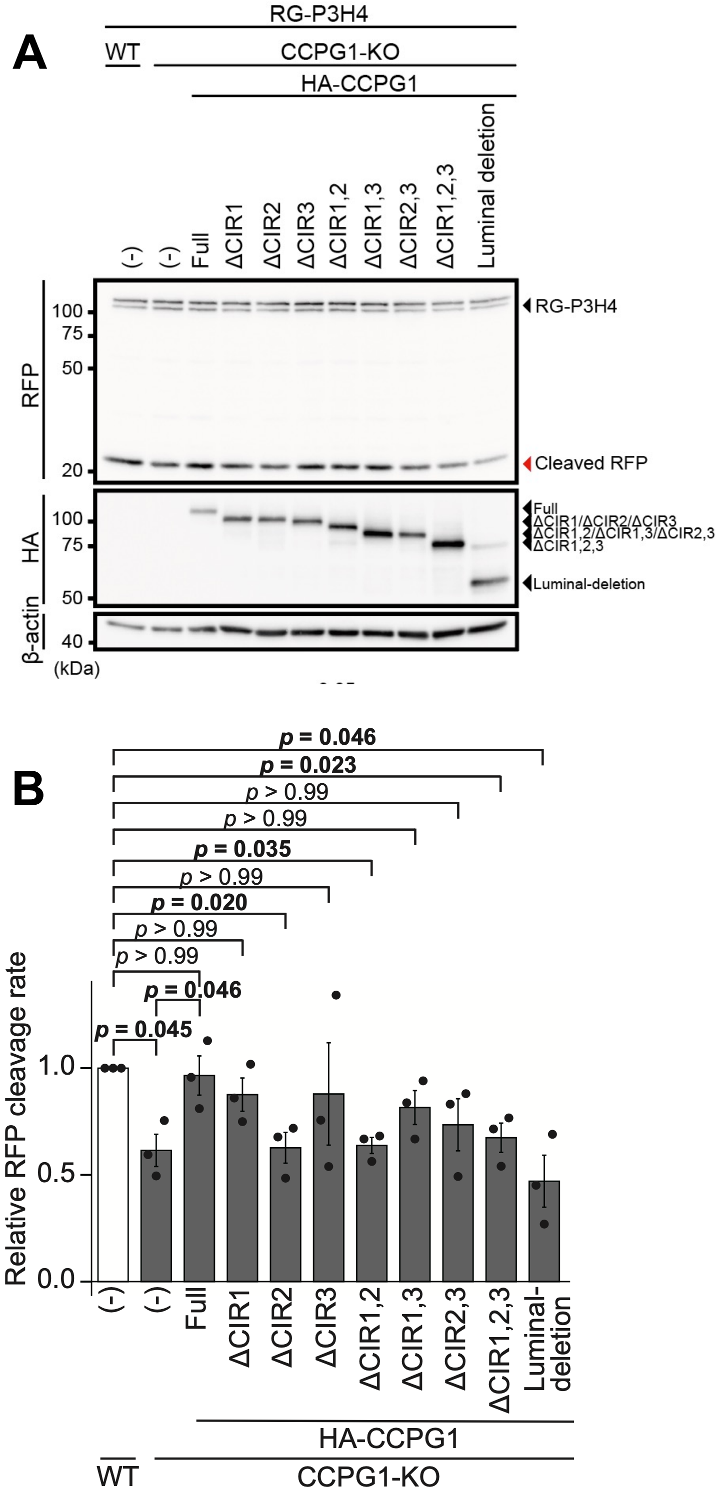

Figure 52. CIR2 of CCPG1 is required for lysosomal degradation of P3H4.

Tet-On WT HeLa cells and CCPG1 KO HeLa cells co-expressing full-length or CIR-mutant CCPG1 (constitutive) and SS-RFP-GFP-P3H4 (Tet-On) were cultured with Dox for 48 h, and then subjected to IF and immunoblotting. Cell lysates were analyzed through immunoblotting using antibodies against RFP, HA-tag, and β-actin (loading control) (A). The band intensities of cleaved RFP and SS-RFP-GFP-P3H4 were quantified, and the ratio of cleaved RFP to SS-RFP-GFP-P3H4 (normalized to the WT) is shown. Data represent the mean ± SE of three independent experiments. Differences were analyzed using one-way ANOVA and Sidak's multiple comparison test (B).

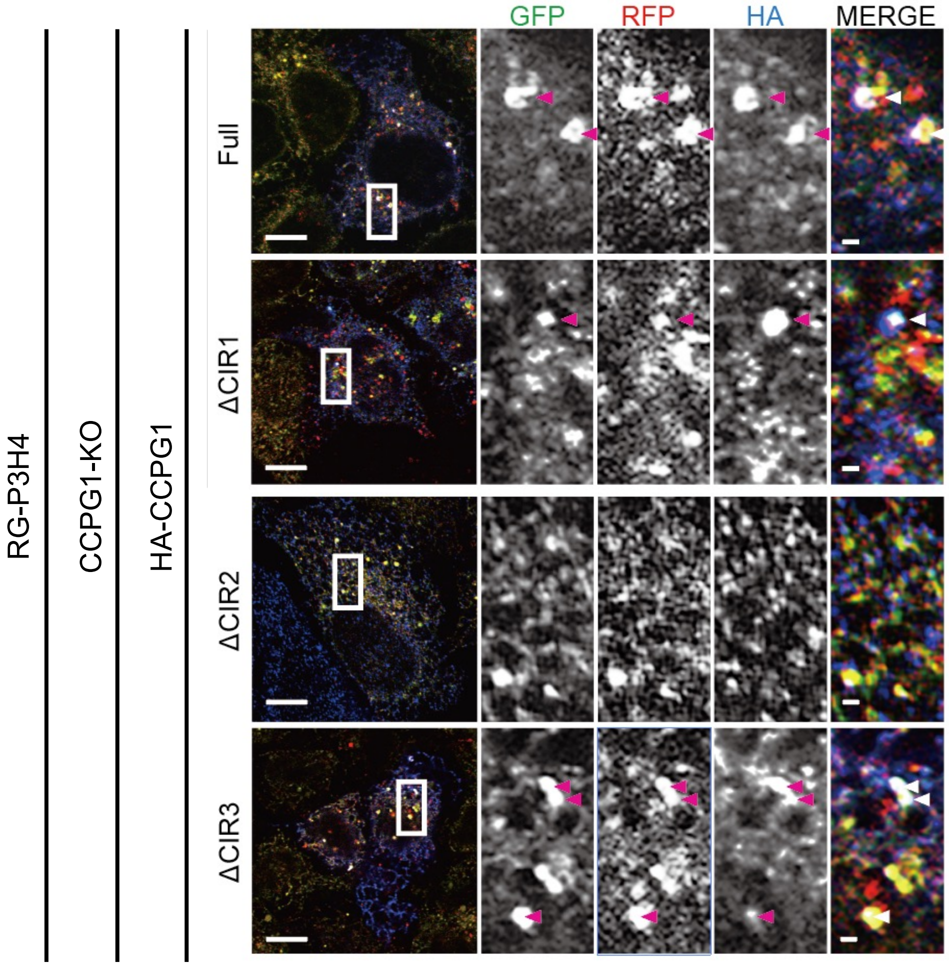

Figure 53. CIR2 of CCPG1 is required for lysosomal degradation of P3H4.

Tet-On WT HeLa cells and CCPG1 KO HeLa cells co-expressing full-length or CIR-mutant CCPG1 (constitutive) and SS-RFP-GFP-P3H4 (Tet-On) were stained with antibodies against HA-tag and analyzed through immunofluorescence microscopy. GFP and RFP-positive signals colocalizing with HA-positive structures (arrowhead) are indicated. Scale bars represent 10 and 1 μm (inset).

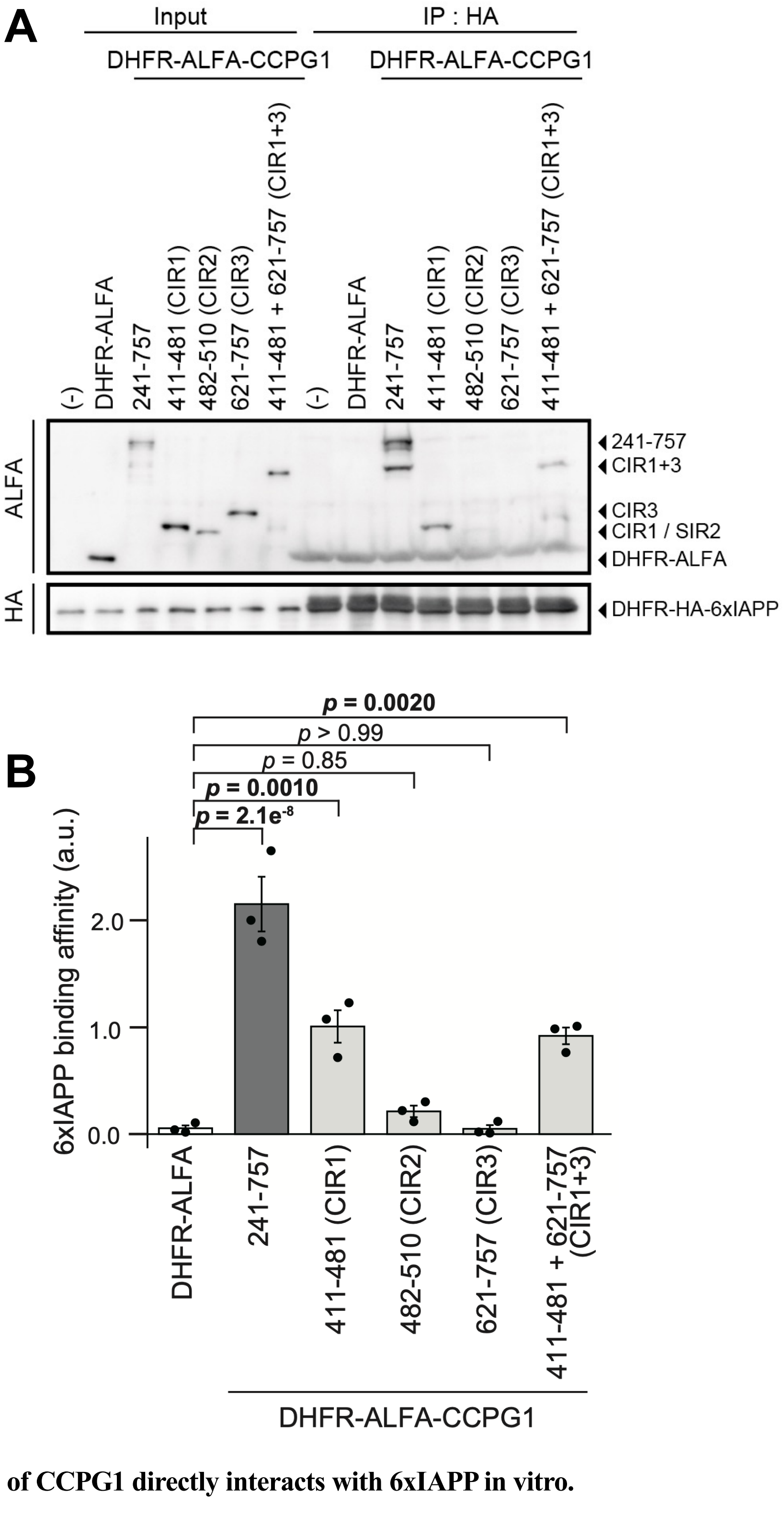

Figure 54. CIR1 of CCPG1 directly interacts with 6xIAPP in vitro.

DHFR-ALFA-tagged C-terminal truncated mutants of CCPG1 and DHFR-HA-6xIAPP synthesized using a cell-free protein synthesis system were mixed with anti-HA antibody-conjugated Sepharose and incubated at 4° C for 1 h. After washing, eluates from the Sepharose were analyzed through immunoblotting with antibodies against ALFA-tag and HA-tag (A). The band intensities of DHFR-tag and the luminal domains of CCPG1 were quantified; the ratio of IP to input is shown. Data represent the mean ± SE of three independent experiments. Differences were statistically analyzed by Dunnett's multiple comparison test (B).

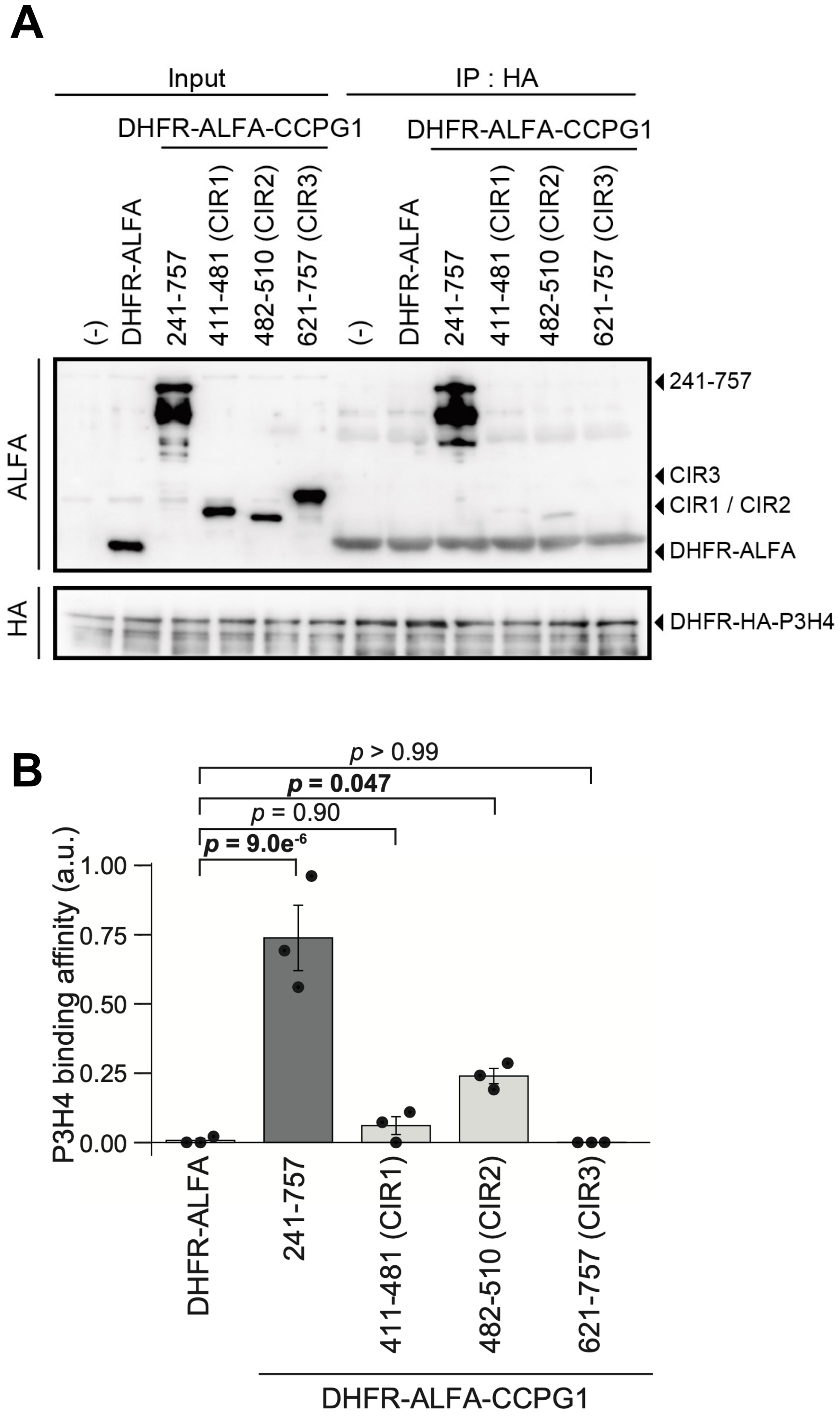

Figure 55. CIR2 of CCPG1 directly interacts with P3H4 in vitro.

DHFR-ALFA-tagged C-terminal truncated mutants of CCPG1 and DHFR-HA-P3H4 were synthesized using a cell-free protein synthesis system, and then mixed with anti-HA antibody-conjugated Sepharose and incubated at 4° C for 1 h. After washing, eluates from the Sepharose were analyzed through immunoblotting with antibodies against ALFA-tag and HA-tag (A). The band intensities of DHFR-tag and luminal domains of CCPG1 were quantified; the ratio of IP to input is shown. Data represent the mean ± SE of three independent experiments . Differences were statistically analyzed by Dunnett's multiple comparison test (B).

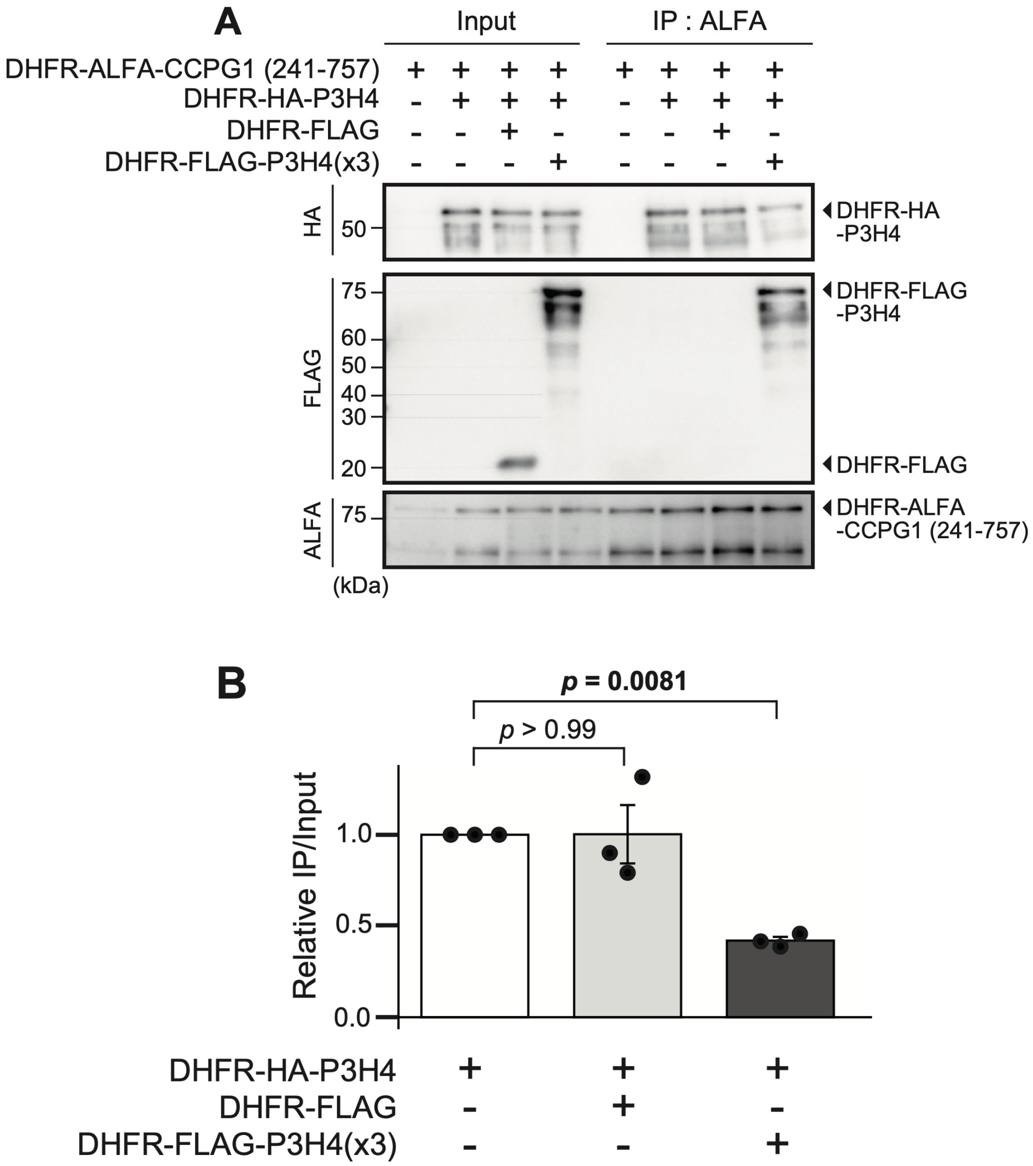

Figure 56. The same ER luminal cargo competitively inhibits the interaction with CCPG1.

DHFR-ALFA-CCPG1 (C-terminal full-length) and DHFR-HA-P3H4 with or without DHFR-FLAG-P3H4 or DHFR-FLAG were synthesized using a cell-free protein synthesis system, mixed with anti-ALFA Sepharose and then incubated at 4° C for 1 h. FLAG-tagged products were added at three times the level of HA-tagged cargos (indicated as ×3). Eluted products were analyzed through immunoblotting with antibodies against ALFA-, FLAG- and HA-tag (A). The bar graph shows the ratio between the indicated band intensities. Data represent the mean ± SE of three independent experiments. Differences were statistically analyzed by Dunnett's multiple comparison test (B).

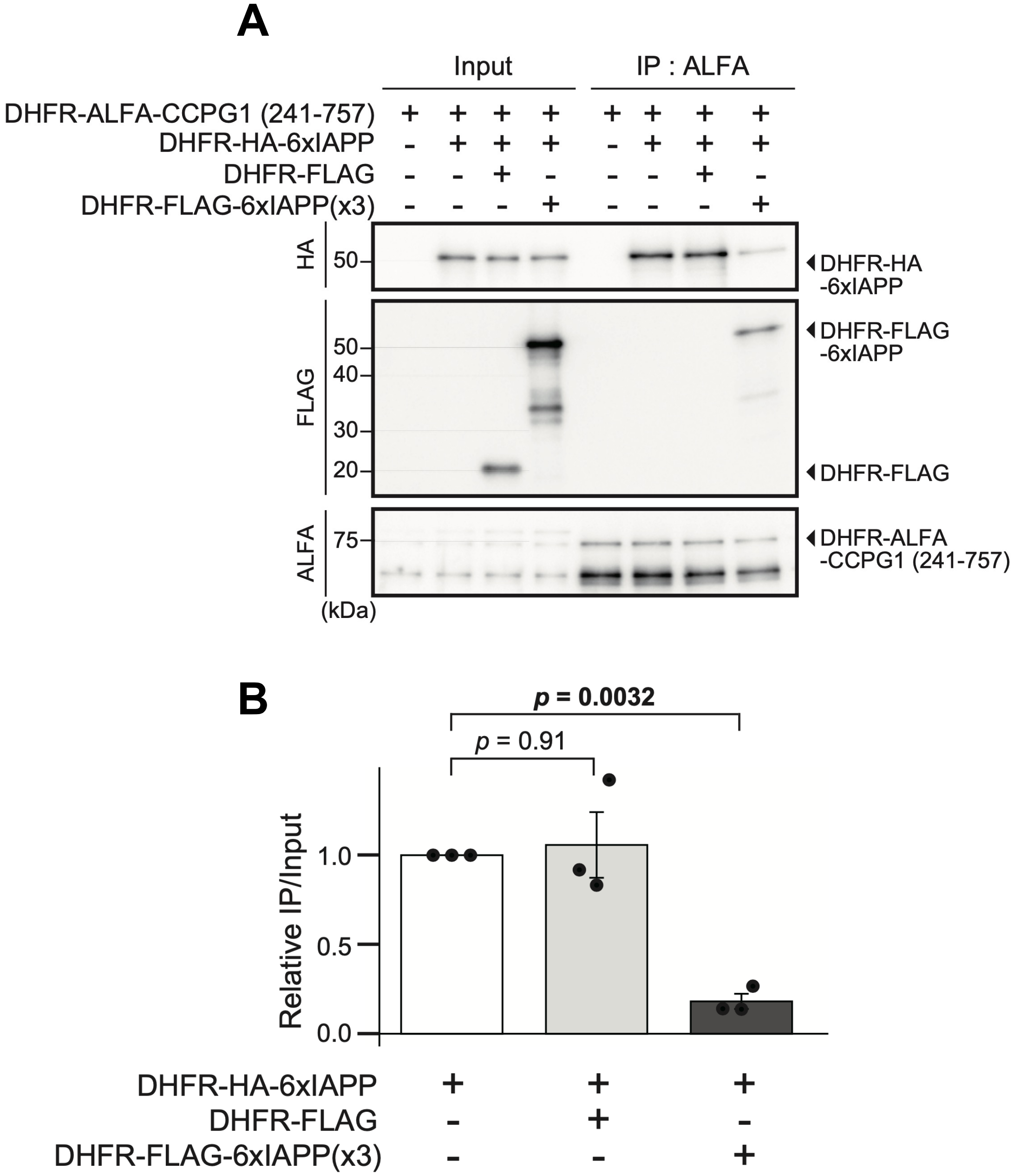

Figure 57. The same ER luminal cargo competitively inhibits the interaction with CCPG1.

DHFR-ALFA-CCPG1 (C-terminal full-length) and DHFR-HA-6xIAPP with or without DHFR-FLAG-6xIAPP or DHFR-FLAG were synthesized using a cell-free protein synthesis system, mixed with anti-ALFA Sepharose and then incubated at 4° C for 1 h. FLAG-tagged products were added at three times the level of HA-tagged cargos (indicated as ×3). Eluted products were analyzed through immunoblotting with antibodies against ALFA-, FLAG- and HA-tag (A). The bar graph shows the ratio between the indicated band intensities. Data represent the mean ± SE of three independent experiments. Differences were statistically analyzed by Dunnett's multiple comparison test (B).

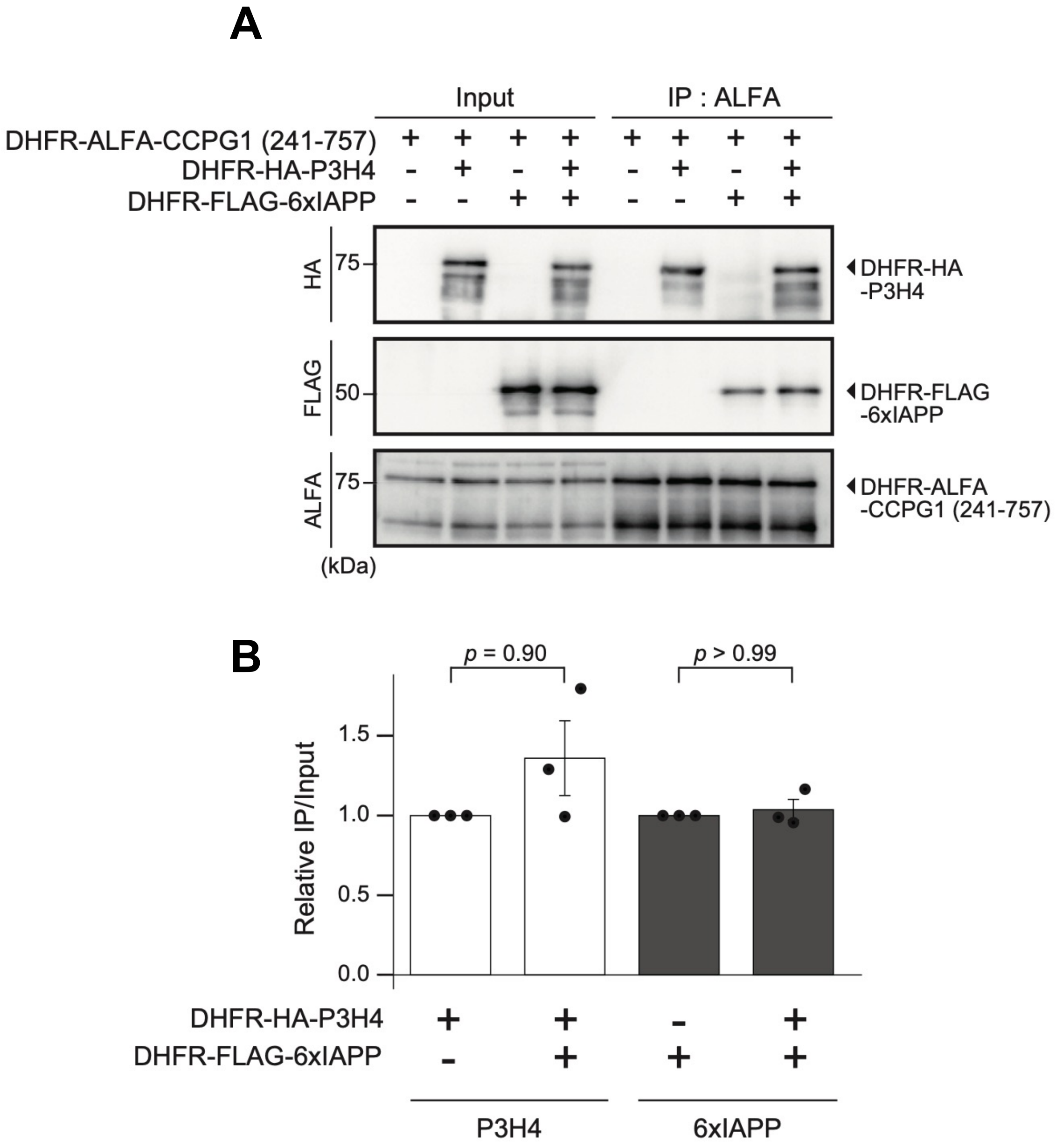

Figure 58. Different ER luminal cargos are able to interact with CCPG1 simultaneously.

Synthesized DHFR-HA-P3H4 and DHFR-FLAG-6xIAPP were mixed with DHFR-ALFA-CCPG1 (C-terminal), either alone or in combination. Anti-ALFA beads were added to the mixture, which was allowed to react at 4° C for 1 h. After washing four times with 1× lysis buffer, SDS sample buffer was added and each eluate was analyzed through immunoblotting using antibodies against ALFA-, FLAG- and HA-tag (A). The bar graph shows the ratio of IP to input ($n = 3$). The data represent mean ± SE. Differences were statistically analyzed by Dunnett's multiple comparison test (B).

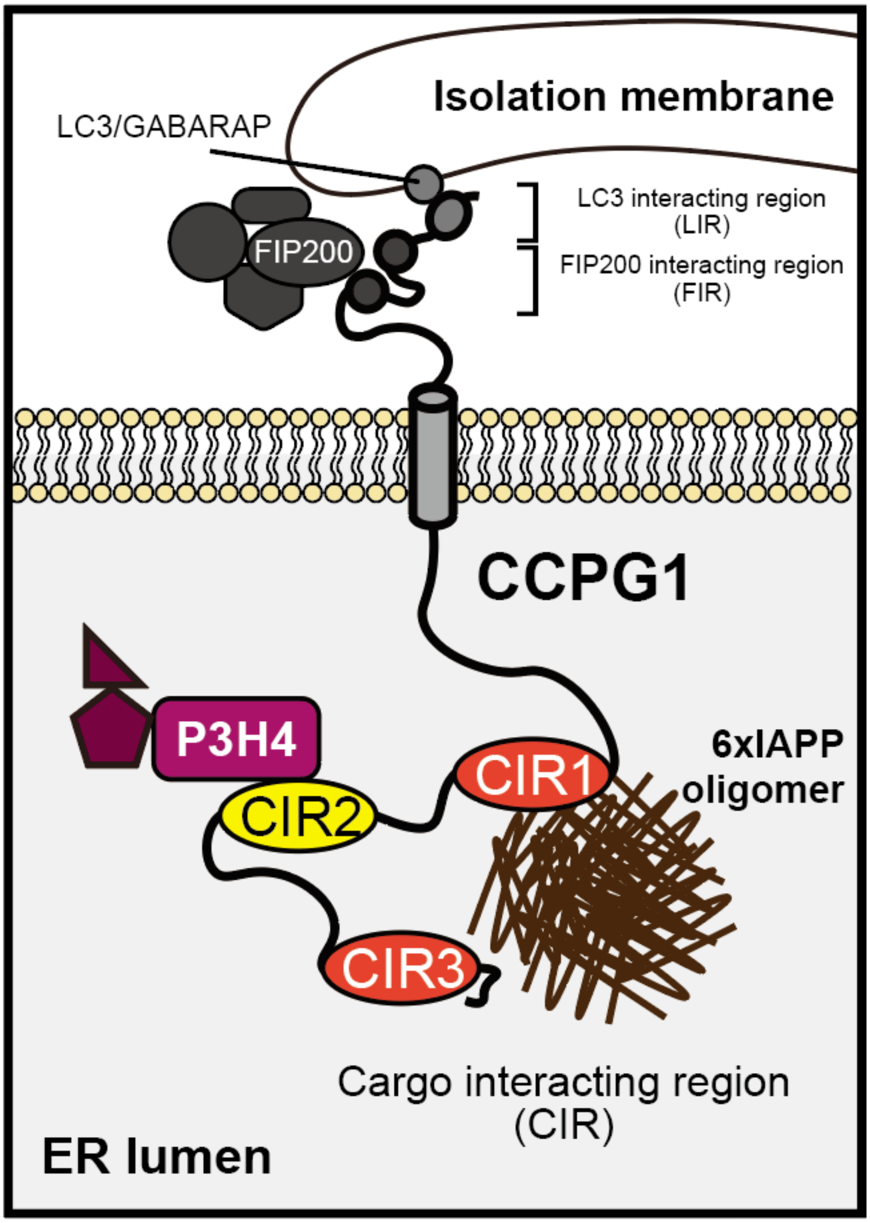

Figure 59. A simultaneous recognition model, in which CCPG1 directly interacts with multiple ER luminal cargos.

ACKNOWLEDGEMENTS

I thank Dr. Yoshitaka Tanaka (Kyushu University) for the anti-LAMP1 anti-bodies; Prof. Takeshi Murata (Chiba University) for cell sorting support; and Keita Chagi, Eigo Takeda, Yutaro Hama and members of the Matsuura lab for valuable discussions.

I also thank JSPS KAKENHI (Grant Numbers 22J12812), and JST SPRING (Grant Number JPMJSP2109) for providing research grant.

I finally thank Dr. Eisuke Itakura (Chiba University) and Prof. Akira Matsuura (Chiba University) very much for supervising my study for seven-years.

REFERENCES

Adamson, B., Norman, T.M., Jost, M., Cho, M.Y., Nuñez, J.K., Chen, Y., Villalta, J.E., Gilbert, L.A., Horlbeck, M.A., Hein, M.Y., Pak, R.A., Gray, A.N., Gross, C.A., Dixit, A., Parnas, O., Regev, A., and Weissman, J.S. (2016). A Multiplexed Single-Cell CRISPR Screening Platform Enables Systematic Dissection of the Unfolded Protein Response. Cell *167*, 1867-1882.e1821.

Albe, K.R., Butler, M.H., and Wright, B.E. (1990). Cellular concentrations of enzymes and their substrates. J Theor Biol *143*, 163-195.

An, H., Ordureau, A., Paulo, J.A., Shoemaker, C.J., Denic, V., and Harper, J.W. (2019). TEX264 Is an Endoplasmic Reticulum-Resident ATG8-Interacting Protein Critical for ER Remodeling during Nutrient Stress. Mol Cell *74*, 891-908.e810.

Ast, T., Michaelis, S., and Schuldiner, M. (2016). The Protease Ste24 Clears Clogged Translocons. Cell *164*, 103-114.

Bernales, S., McDonald, K.L., and Walter, P. (2006). Autophagy counterbalances endoplasmic reticulum expansion during the unfolded protein response. PLoS biology *4*, e423.

Bhaskara, R.M., Grumati, P., Garcia-Pardo, J., Kalayil, S., Covarrubias-Pinto, A., Chen, W., Kudryashev, M., Dikic, I., and Hummer, G. (2019). Curvature induction and membrane remodeling by FAM134B reticulon homology domain assist selective ER-phagy. Nature communications *10*, 2370.

Blum, M., Chang, H.Y., Chuguransky, S., Grego, T., Kandasaamy, S., Mitchell, A., Nuka, G., Paysan-Lafosse, T., Qureshi, M., Raj, S., Richardson, L., Salazar, G.A., Williams, L., Bork, P., Bridge, A., Gough, J., Haft, D.H., Letunic, I., Marchler-Bauer, A., Mi, H., Natale, D.A., Necci, M., Orengo, C.A., Pandurangan, A.P., Rivoire, C., Sigrist, C.J.A., Sillitoe, I., Thanki, N., Thomas, P.D., Tosatto, S.C.E., Wu, C.H., Bateman, A., and Finn, R.D. (2021). The InterPro protein families and domains database: 20 years on. Nucleic Acids Res *49*, D344-D354.

Boersema, P.J., Raijmakers, R., Lemeer, S., Mohammed, S., and Heck, A.J. (2009). Multiplex peptide stable isotope dimethyl labeling for quantitative proteomics. Nat Protoc *4*, 484-494.

Bradbury, J. (2003). Chaperones: keeping a close eye on protein folding. Lancet *361*, 1194-1195.

Brown, G.C. (1991). Total cell protein concentration as an evolutionary constraint on the metabolic control distribution in cells. J Theor Biol *153*, 195-203.

Bukau, B., Weissman, J., and Horwich, A. (2006). Molecular chaperones and protein quality control. Cell *125*, 443-451.

Butler, A.E., Janson, J., Bonner-Weir, S., Ritzel, R., Rizza, R.A., and Butler, P.C. (2003). Beta-cell deficit and increased beta-cell apoptosis in humans with type 2 diabetes. Diabetes *52*, 102-110.

Callea, F., Brisigotti, M., Fabbretti, G., Bonino, F., and Desmet, V.J. (1992). Hepatic endoplasmic reticulum storage diseases. Liver *12*, 357-362.

Callea, F., and Desmet, V. (2021). The Discovery of Endoplasmic Reticulum Storage Disease. The Connection between an H&E Slide and the Brain. Int J Mol Sci *22*.

Chakrabarti, A., Chen, A.W., and Varner, J.D. (2011). A review of the mammalian unfolded protein response. Biotechnol Bioeng *108*, 2777-2793.

Chen, Q., Xiao, Y., Chai, P., Zheng, P., Teng, J., and Chen, J. (2019). ATL3 Is a Tubular ER-Phagy Receptor for GABARAP-Mediated Selective Autophagy. Current biology : CB *29*, 846-855.e846.

Chino, H., Hatta, T., Natsume, T., and Mizushima, N. (2019). Intrinsically Disordered Protein TEX264 Mediates ER-phagy. Molecular cell *74*, 909-921.e906.

Chino, H., Yamasaki, A., Ode, K.L., Ueda, H.R., Noda, N.N., and Mizushima, N. (2022). Phosphorylation by casein kinase 2 enhances the interaction between ER-phagy receptor TEX264 and ATG8 proteins. EMBO Rep, e54801.

Chipurupalli, S., Ganesan, R., Martini, G., Mele, L., Reggio, A., Esposito, M., Kannan, E., Namasivayam, V., Grumati, P., Desiderio, V., and Robinson, N. (2022). Cancer cells adapt FAM134B/BiP mediated ER-phagy to survive hypoxic stress. Cell Death Dis *13*, 357.

DE DUVE, C. (1963). The lysosome. Sci Am *208*, 64-72.

De Leonibus, C., Cinque, L., and Settembre, C. (2019). Emerging lysosomal pathways for quality control at the endoplasmic reticulum. FEBS letters *593*, 2319-2329.

Ellgaard, L., and Helenius, A. (2003). Quality control in the endoplasmic reticulum. Nat Rev Mol Cell Biol *4*, 181-191.

Forrester, A., De Leonibus, C., Grumati, P., Fasana, E., Piemontese, M., Staiano, L., Fregno, I., Raimondi, A., Marazza, A., Bruno, G., Iavazzo, M., Intartaglia, D., Seczynska, M., van Anken, E., Conte, I., De Matteis, M.A., Dikic, I., Molinari, M., and Settembre, C. (2019). A selective ER-phagy exerts procollagen quality control via a Calnexin-FAM134B complex. The EMBO journal *38*.

Fregno, I., Fasana, E., Bergmann, T.J., Raimondi, A., Loi, M., Soldà, T., Galli, C., D'Antuono, R., Morone, D., Danieli, A., Paganetti, P., van Anken, E., and Molinari, M. (2018). ER-to-lysosome-associated degradation of proteasome-resistant ATZ polymers occurs via receptor-mediated vesicular transport. EMBO J *37*.

Fumagalli, F., Noack, J., Bergmann, T.J., Cebollero, E., Pisoni, G.B., Fasana, E., Fregno, I., Galli, C., Loi, M., Soldà, T., D'Antuono, R., Raimondi, A., Jung, M., Melnyk, A., Schorr, S., Schreiber, A., Simonelli, L., Varani, L., Wilson-Zbinden, C., Zerbe, O., Hofmann, K., Peter, M., Quadroni, M., Zimmermann, R., and Molinari, M. (2016). Translocon component Sec62 acts in endoplasmic reticulum turnover during stress recovery. Nature cell biology *18*, 1173-1184.

Gruenwald, K., Castagnola, P., Besio, R., Dimori, M., Chen, Y., Akel, N.S., Swain, F.L., Skinner, R.A., Eyre, D.R., Gaddy, D., Suva, L.J., and Morello, R. (2014). Sc65 is a novel endoplasmic reticulum protein that regulates bone mass homeostasis. J Bone Miner Res *29*, 666-675.

Grumati, P., Dikic, I., and Stolz, A. (2018). ER-phagy at a glance. J Cell Sci *131*.

Grumati, P., Morozzi, G., Hölper, S., Mari, M., Harwardt, M.I., Yan, R., Müller, S., Reggiori, F., Heilemann, M., and Dikic, I. (2017). Full length RTN3 regulates turnover of tubular endoplasmic reticulum via selective autophagy. eLife *6*.

Götzke, H., Kilisch, M., Martínez-Carranza, M., Sograte-Idrissi, S., Rajavel, A., Schlichthaerle, T., Engels, N., Jungmann, R., Stenmark, P., Opazo, F., and Frey, S. (2019). The ALFA-tag is a highly versatile tool for nanobody-based bioscience applications. Nat Commun *10*, 4403.

Hao, L., Pang, K., Pang, H., Zhang, J., Zhang, Z., He, H., Zhou, R., Shi, Z., and Han, C. (2020). Knockdown of P3H4 inhibits proliferation and invasion of bladder cancer. Aging (Albany NY) *12*, 2156-2168.

Hara, T., Takamura, A., Kishi, C., Iemura, S., Natsume, T., Guan, J.L., and Mizushima, N. (2008). FIP200, a ULK-interacting protein, is required for autophagosome formation in mammalian cells. J Cell Biol *181*, 497-510.

Heard, M.E., Besio, R., Weis, M., Rai, J., Hudson, D.M., Dimori, M., Zimmerman, S.M., Kamykowski, J.A., Hogue, W.R., Swain, F.L., Burdine, M.S., Mackintosh, S.G., Tackett, A.J., Suva, L.J., Eyre, D.R., and Morello, R. (2016). Sc65-Null Mice Provide Evidence for a Novel Endoplasmic Reticulum Complex Regulating Collagen Lysyl Hydroxylation. PLoS Genet *12*, e1006002.

Hebert, D.N., and Molinari, M. (2007). In and out of the ER: protein folding, quality control, degradation, and related human diseases. Physiol Rev *87*, 1377-1408.

Hetz, C., Zhang, K., and Kaufman, R.J. (2020). Mechanisms, regulation and functions of the unfolded protein response. Nat Rev Mol Cell Biol *21*, 421-438.

Houck, S.A., Ren, H.Y., Madden, V.J., Bonner, J.N., Conlin, M.P., Janovick, J.A., Conn, P.M., and Cyr, D.M. (2014). Quality control autophagy degrades soluble ERAD-resistant conformers of the misfolded membrane protein GnRHR. Mol Cell *54*, 166-179.

Ishida, Y., Yamamoto, A., Kitamura, A., Lamandé, S.R., Yoshimori, T., Bateman, J.F., Kubota, H., and Nagata, K. (2009). Autophagic elimination of misfolded procollagen aggregates in the endoplasmic reticulum as a means of cell protection. Molecular biology of the cell *20*, 2744-2754.

Iwakura, M., Furusawa, K., Kokubu, T., Ohashi, S., Tanaka, Y., Shimura, Y., and Tsuda, K. (1992). Dihydrofolate reductase as a new "affinity handle". J Biochem *111*, 37-45.

Jia, W., Pua, H.H., Li, Q.J., and He, Y.W. (2011). Autophagy regulates endoplasmic reticulum homeostasis and calcium mobilization in T lymphocytes. Journal of immunology (Baltimore, Md. : 1950) *186*, 1564-1574.

Jiang, X., Wang, X., Ding, X., Du, M., Li, B., Weng, X., Zhang, J., Li, L., Tian, R., Zhu, Q., Chen, S., Wang, L., Liu, W., Fang, L., Neculai, D., and Sun, Q. (2020). FAM134B oligomerization drives endoplasmic reticulum membrane scission for ER-phagy. The EMBO journal *39*, e102608.

Jin, X., Zhou, H., Song, J., Cui, H., Luo, Y., and Jiang, H. (2021). P3H4 Overexpression Serves as a Prognostic Factor in Lung Adenocarcinoma. Comput Math Methods Med *2021*, 9971353.

Jumper, J., Evans, R., Pritzel, A., Green, T., Figurnov, M., Ronneberger, O., Tunyasuvunakool, K., Bates, R., Žídek, A., Potapenko, A., Bridgland, A., Meyer, C., Kohl, S.A.A., Ballard, A.J., Cowie, A., Romera-Paredes, B., Nikolov, S., Jain, R., Adler, J., Back, T., Petersen, S., Reiman, D., Clancy, E., Zielinski, M., Steinegger, M., Pacholska, M., Berghammer, T., Bodenstein, S., Silver, D., Vinyals, O., Senior, A.W., Kavukcuoglu, K., Kohli, P., and Hassabis, D. (2021). Highly accurate protein structure prediction with AlphaFold. Nature *596*, 583-589.

Juszkiewicz, S., and Hegde, R.S. (2018). Quality Control of Orphaned Proteins. Mol Cell *71*, 443-457.

Kang, S.W., Rane, N.S., Kim, S.J., Garrison, J.L., Taunton, J., and Hegde, R.S. (2006). Substrate-specific translocational attenuation during ER stress defines a pre-emptive quality control pathway. Cell *127*, 999-1013.

Katayama, H., Yamamoto, A., Mizushima, N., Yoshimori, T., and Miyawaki, A. (2008). GFP-like proteins stably accumulate in lysosomes. Cell Struct Funct *33*, 1-12.

Kayatekin, C., Amasino, A., Gaglia, G., Flannick, J., Bonner, J.M., Fanning, S., Narayan, P., Barrasa, M.I., Pincus, D., Landgraf, D., Nelson, J., Hesse, W.R., Costanzo, M., Myers, C.L., Boone, C., Florez, J.C., Lindquist, S., and Consortium, A.T.D.-G. (2018). Translocon Declogger Ste24 Protects against IAPP Oligomer-Induced Proteotoxicity. Cell *173*, 62-73.e69.

Keles, U., Iscan, E., Yilmaz, H.E., Karakülah, G., Suner, A., Bal, E., Tasdemir, N., Cavga, A.D., Ekin, U., Mutlu, Z., Kahyaoglu, S., Serdar, M.A., Atabey, N., and Ozturk, M. (2020).

Differential expression of full-length and NH. Am J Physiol Gastrointest Liver Physiol *319*, G733-G747.

Khaminets, A., Heinrich, T., Mari, M., Grumati, P., Huebner, A.K., Akutsu, M., Liebmann, L., Stolz, A., Nietzsche, S., Koch, N., Mauthe, M., Katona, I., Qualmann, B., Weis, J., Reggiori, F., Kurth, I., Hübner, C.A., and Dikic, I. (2015). Regulation of endoplasmic reticulum turnover by selective autophagy. Nature *522*, 354-358.

Kimura, S., Noda, T., and Yoshimori, T. (2007). Dissection of the autophagosome maturation process by a novel reporter protein, tandem fluorescent-tagged LC3. Autophagy *3*, 452-460.

Kitamura, T., Koshino, Y., Shibata, F., Oki, T., Nakajima, H., Nosaka, T., and Kumagai, H. (2003). Retrovirus-mediated gene transfer and expression cloning: powerful tools in functional genomics. Exp Hematol *31*, 1007-1014.

Klionsky, D.J., Petroni, G., Amaravadi, R.K., Baehrecke, E.H., Ballabio, A., Boya, P., Bravo-San Pedro, J.M., Cadwell, K., Cecconi, F., Choi, A.M.K., Choi, M.E., Chu, C.T., Codogno, P., Colombo, M.I., Cuervo, A.M., Deretic, V., Dikic, I., Elazar, Z., Eskelinen, E.L., Fimia, G.M., Gewirtz, D.A., Green, D.R., Hansen, M., Jäättelä, M., Johansen, T., Juhász, G., Karantza, V., Kraft, C., Kroemer, G., Ktistakis, N.T., Kumar, S., Lopez-Otin, C., Macleod, K.F., Madeo, F., Martinez, J., Meléndez, A., Mizushima, N., Münz, C., Penninger, J.M., Perera, R.M., Piacentini, M., Reggiori, F., Rubinsztein, D.C., Ryan, K.M., Sadoshima, J., Santambrogio, L., Scorrano, L., Simon, H.U., Simon, A.K., Simonsen, A., Stolz, A., Tavernarakis, N., Tooze, S.A., Yoshimori, T., Yuan, J., Yue, Z., Zhong, Q., Galluzzi, L., and Pietrocola, F. (2021). Autophagy in major human diseases. EMBO J *40*, e108863.

Klöppel, G., Löhr, M., Habich, K., Oberholzer, M., and Heitz, P.U. (1985). Islet pathology and the pathogenesis of type 1 and type 2 diabetes mellitus revisited. Surv Synth Pathol Res *4*, 110-125.

Kohno, S., Shiozaki, Y., Keenan, A.L., Miyazaki-Anzai, S., and Miyazaki, M. (2019). An N-terminal-truncated isoform of FAM134B (FAM134B-2) regulates starvation-induced hepatic selective ER-phagy. Life Sci Alliance *2*.

Kostenko, E.V., Olabisi, O.O., Sahay, S., Rodriguez, P.L., and Whitehead, I.P. (2006). Ccpg1, a novel scaffold protein that regulates the activity of the Rho guanine nucleotide exchange factor Dbs. Mol Cell Biol *26*, 8964-8975.

Kraft, C., Deplazes, A., Sohrmann, M., and Peter, M. (2008). Mature ribosomes are selectively degraded upon starvation by an autophagy pathway requiring the Ubp3p/Bre5p ubiquitin protease. Nat Cell Biol *10*, 602-610.

Kurth, I., Pamminger, T., Hennings, J.C., Soehendra, D., Huebner, A.K., Rotthier, A., Baets, J., Senderek, J., Topaloglu, H., Farrell, S.A., Nürnberg, G., Nürnberg, P., De Jonghe, P., Gal, A., Kaether, C., Timmerman, V., and Hübner, C.A. (2009). Mutations in FAM134B, encoding a newly identified Golgi protein, cause severe sensory and autonomic neuropathy. Nat Genet *41*, 1179-1181.

Lemasters, J.J. (2005). Selective mitochondrial autophagy, or mitophagy, as a targeted defense against oxidative stress, mitochondrial dysfunction, and aging. Rejuvenation Res *8*, 3-5.

Li, W., Ye, L., Chen, Y., and Chen, P. (2018). P3H4 is correlated with clinicopathological features and prognosis in bladder cancer. World J Surg Oncol *16*, 206.

Liang, C.C., Wang, C., Peng, X., Gan, B., and Guan, J.L. (2010). Neural-specific deletion of FIP200 leads to cerebellar degeneration caused by increased neuronal death and axon degeneration. J Biol Chem *285*, 3499-3509.

Linxweiler, M., Schick, B., and Zimmermann, R. (2017). Let's talk about Secs: Sec61, Sec62 and Sec63 in signal transduction, oncology and personalized medicine. Signal Transduct Target Ther *2*, 17002.

Maejima, I., Takahashi, A., Omori, H., Kimura, T., Takabatake, Y., Saitoh, T., Yamamoto, A., Hamasaki, M., Noda, T., Isaka, Y., and Yoshimori, T. (2013). Autophagy sequesters damaged lysosomes to control lysosomal biogenesis and kidney injury. EMBO J *32*, 2336-2347.

Marciniak, S.J., Ordóñez, A., Dickens, J.A., Chambers, J.E., Patel, V., Dominicus, C.S., and Malzer, E. (2016). New Concepts in Alpha-1 Antitrypsin Deficiency Disease Mechanisms. Ann Am Thorac Soc *13 Suppl 4*, S289-296.

McGuffin, L.J., Bryson, K., and Jones, D.T. (2000). The PSIPRED protein structure prediction server. Bioinformatics *16*, 404-405.

Melia, T.J., Lystad, A.H., and Simonsen, A. (2020). Autophagosome biogenesis: From membrane growth to closure. J Cell Biol *219*.

Mercer, T.J., Gubas, A., and Tooze, S.A. (2018). A molecular perspective of mammalian autophagosome biogenesis. J Biol Chem *293*, 5386-5395.

Mizushima, N., and Komatsu, M. (2011). Autophagy: renovation of cells and tissues. Cell *147*, 728-741.

Mizushima, N., Yamamoto, A., Hatano, M., Kobayashi, Y., Kabeya, Y., Suzuki, K., Tokuhisa, T., Ohsumi, Y., and Yoshimori, T. (2001). Dissection of autophagosome formation using Apg5-deficient mouse embryonic stem cells. J Cell Biol *152*, 657-668.

Mochida, K., and Nakatogawa, H. (2022). ER-phagy: selective autophagy of the endoplasmic reticulum. EMBO Rep *23*, e55192.

Mochida, K., Oikawa, Y., Kimura, Y., Kirisako, H., Hirano, H., Ohsumi, Y., and Nakatogawa, H. (2015). Receptor-mediated selective autophagy degrades the endoplasmic reticulum and the nucleus. Nature *522*, 359-362.

Mochida, K., Yamasaki, A., Matoba, K., Kirisako, H., Noda, N.N., and Nakatogawa, H. (2020). Super-assembly of ER-phagy receptor Atg40 induces local ER remodeling at contacts with forming autophagosomal membranes. Nat Commun *11*, 3306.

Molinari, M. (2021). ER-phagy responses in yeast, plants, and mammalian cells and their crosstalk with UPR and ERAD. Dev Cell *56*, 949-966.

Morita, K., Hama, Y., Izume, T., Tamura, N., Ueno, T., Yamashita, Y., Sakamaki, Y., Mimura, K., Morishita, H., Shihoya, W., Nureki, O., Mano, H., and Mizushima, N. (2018). Genome-wide CRISPR screen identifies. J Cell Biol *217*, 3817-3828.

Murphy, S.M., Davidson, G.L., Brandner, S., Houlden, H., and Reilly, M.M. (2012). Mutation in FAM134B causing severe hereditary sensory neuropathy. J Neurol Neurosurg Psychiatry *83*, 119-120.

Nakagawa, I., Amano, A., Mizushima, N., Yamamoto, A., Yamaguchi, H., Kamimoto, T., Nara, A., Funao, J., Nakata, M., Tsuda, K., Hamada, S., and Yoshimori, T. (2004). Autophagy defends cells against invading group A Streptococcus. Science *306*, 1037-1040.

Ni, M., and Lee, A.S. (2007). ER chaperones in mammalian development and human diseases. FEBS Lett *581*, 3641-3651.

Nthiga, T.M., Kumar Shrestha, B., Sjøttem, E., Bruun, J.A., Bowitz Larsen, K., Bhujabal, Z., Lamark, T., and Johansen, T. (2020). CALCOCO1 acts with VAMP-associated proteins to mediate ER-phagy. The EMBO journal *39*, e103649.

Ochs, R.L., Stein, T.W., Chan, E.K., Ruutu, M., and Tan, E.M. (1996). cDNA cloning and characterization of a novel nucleolar protein. Mol Biol Cell *7*, 1015-1024.

Owen, M.C., Brennan, S.O., Lewis, J.H., and Carrell, R.W. (1983). Mutation of antitrypsin to antithrombin. alpha 1-antitrypsin Pittsburgh (358 Met leads to Arg), a fatal bleeding disorder. N Engl J Med *309*, 694-698.

Pedrazzini, E., Villa, A., Longhi, R., Bulbarelli, A., and Borgese, N. (2000). Mechanism of residence of cytochrome b(5), a tail-anchored protein, in the endoplasmic reticulum. J Cell Biol *148*, 899-914.

Pengo, N., Scolari, M., Oliva, L., Milan, E., Mainoldi, F., Raimondi, A., Fagioli, C., Merlini, A., Mariani, E., Pasqualetto, E., Orfanelli, U., Ponzoni, M., Sitia, R., Casola, S., and Cenci, S. (2013). Plasma cells require autophagy for sustainable immunoglobulin production. Nature immunology *14*, 298-305.

Rappsilber, J., Mann, M., and Ishihama, Y. (2007). Protocol for micro-purification, enrichment, pre-fractionation and storage of peptides for proteomics using StageTips. Nat Protoc *2*, 1896-1906.

Ruggiano, A., Foresti, O., and Carvalho, P. (2014). Quality control: ER-associated degradation: protein quality control and beyond. The Journal of cell biology *204*, 869-879.

Rutishauser, J., and Spiess, M. (2002). Endoplasmic reticulum storage diseases. Swiss Med Wkly *132*, 211-222.

Saitoh, T., Fujita, N., Hayashi, T., Takahara, K., Satoh, T., Lee, H., Matsunaga, K., Kageyama, S., Omori, H., Noda, T., Yamamoto, N., Kawai, T., Ishii, K., Takeuchi, O., Yoshimori, T., and Akira, S. (2009). Atg9a controls dsDNA-driven dynamic translocation of STING and the innate immune response. Proc Natl Acad Sci U S A *106*, 20842-20846.

Schröder, M., and Kaufman, R.J. (2005). ER stress and the unfolded protein response. Mutat Res *569*, 29-63.

Shi, Q., Ge, Y., Sharoar, M.G., He, W., Xiang, R., Zhang, Z., Hu, X., and Yan, R. (2014). Impact of RTN3 deficiency on expression of BACE1 and amyloid deposition. J Neurosci *34*, 13954-13962.

Shimizu, Y., Inoue, A., Tomari, Y., Suzuki, T., Yokogawa, T., Nishikawa, K., and Ueda, T. (2001). Cell-free translation reconstituted with purified components. Nat Biotechnol *19*, 751-755.

Shimizu, Y., Kanamori, T., and Ueda, T. (2005). Protein synthesis by pure translation systems. Methods *36*, 299-304.

Singh, R., Kaushik, S., Wang, Y., Xiang, Y., Novak, I., Komatsu, M., Tanaka, K., Cuervo, A.M., and Czaja, M.J. (2009). Autophagy regulates lipid metabolism. Nature *458*, 1131-1135.

Smith, M., and Wilkinson, S. (2017). ER homeostasis and autophagy. Essays Biochem *61*, 625-635.

Smith, M.D., Harley, M.E., Kemp, A.J., Wills, J., Lee, M., Arends, M., von Kriegsheim, A., Behrends, C., and Wilkinson, S. (2018). CCPG1 Is a Non-canonical Autophagy Cargo Receptor Essential for ER-Phagy and Pancreatic ER Proteostasis. Dev Cell *44*, 217-232.e211.

Srivastava, D.K., and Bernhard, S.A. (1986). Enzyme-enzyme interactions and the regulation of metabolic reaction pathways. Curr Top Cell Regul *28*, 1-68.

Stephani, M., Picchianti, L., Gajic, A., Beveridge, R., Skarwan, E., Sanchez de Medina Hernandez, V., Mohseni, A., Clavel, M., Zeng, Y., Naumann, C., Matuszkiewicz, M., Turco, E., Loefke, C., Li, B., Dürnberger, G., Schutzbier, M., Chen, H.T., Abdrakhmanov, A., Savova, A., Chia, K.S., Djamei, A., Schaffner, I., Abel, S., Jiang, L., Mechtler, K., Ikeda, F., Martens, S., Clausen, T., and Dagdas, Y. (2020). A cross-kingdom conserved ER-phagy receptor maintains endoplasmic reticulum homeostasis during stress. Elife *9*.

Stolz, A., Ernst, A., and Dikic, I. (2014). Cargo recognition and trafficking in selective autophagy. Nat Cell Biol *16*, 495-501.

Sun, J., Wang, W., and Zheng, H. (2022). ROOT HAIR DEFECTIVE3 Is a Receptor for Selective Autophagy of the Endoplasmic Reticulum in. Front Plant Sci *13*, 817251.

Teckman, J.H., and Perlmutter, D.H. (2000). Retention of mutant alpha(1)-antitrypsin Z in endoplasmic reticulum is associated with an autophagic response. Am J Physiol Gastrointest Liver Physiol *279*, G961-974.

Tian, X., Jin, R.U., Bredemeyer, A.J., Oates, E.J., Błazewska, K.M., McKenna, C.E., and Mills, J.C. (2010). RAB26 and RAB3D are direct transcriptional targets of MIST1 that regulate exocrine granule maturation. Mol Cell Biol *30*, 1269-1284.

Turco, E., Witt, M., Abert, C., Bock-Bierbaum, T., Su, M.Y., Trapannone, R., Sztacho, M., Danieli, A., Shi, X., Zaffagnini, G., Gamper, A., Schuschnig, M., Fracchiolla, D., Bernklau, D., Romanov, J., Hartl, M., Hurley, J.H., Daumke, O., and Martens, S. (2019). FIP200 Claw Domain Binding to p62 Promotes Autophagosome Formation at Ubiquitin Condensates. Molecular cell *74*, 330-346.e311.

Uhlén, M., Fagerberg, L., Hallström, B.M., Lindskog, C., Oksvold, P., Mardinoglu, A., Sivertsson, Å., Kampf, C., Sjöstedt, E., Asplund, A., Olsson, I., Edlund, K., Lundberg, E., Navani, S., Szigyarto, C.A., Odeberg, J., Djureinovic, D., Takanen, J.O., Hober, S., Alm, T., Edqvist, P.H., Berling, H., Tegel, H., Mulder, J., Rockberg, J., Nilsson, P., Schwenk, J.M., Hamsten, M., von Feilitzen, K., Forsberg, M., Persson, L., Johansson, F., Zwahlen, M., von Heijne, G., Nielsen, J., and Pontén, F. (2015). Proteomics. Tissue-based map of the human proteome. Science *347*, 1260419.

Varadi, M., Anyango, S., Deshpande, M., Nair, S., Natassia, C., Yordanova, G., Yuan, D., Stroe, O., Wood, G., Laydon, A., Žídek, A., Green, T., Tunyasuvunakool, K., Petersen, S., Jumper, J., Clancy, E., Green, R., Vora, A., Lutfi, M., Figurnov, M., Cowie, A., Hobbs, N., Kohli, P., Kleywegt, G., Birney, E., Hassabis, D., and Velankar, S. (2022). AlphaFold Protein Structure Database: massively expanding the structural coverage of protein-sequence space with high-accuracy models. Nucleic Acids Res *50*, D439-D444.

Webb, J.L., Ravikumar, B., Atkins, J., Skepper, J.N., and Rubinsztein, D.C. (2003). Alpha-Synuclein is degraded by both autophagy and the proteasome. J Biol Chem *278*, 25009-25013.

Wilfling, F., Lee, C.W., Erdmann, P.S., Zheng, Y., Sherpa, D., Jentsch, S., Pfander, B., Schulman, B.A., and Baumeister, W. (2020). A Selective Autophagy Pathway for Phase-Separated Endocytic Protein Deposits. Mol Cell *80*, 764-778.e767.

Wilkinson, S. (2020). Emerging Principles of Selective ER Autophagy. Journal of molecular biology *432*, 185-205.

Yamasaki, A., Alam, J.M., Noshiro, D., Hirata, E., Fujioka, Y., Suzuki, K., Ohsumi, Y., and

Noda, N.N. (2020). Liquidity Is a Critical Determinant for Selective Autophagy of Protein Condensates. Mol Cell *77*, 1163-1175.e1169.

Yang, J., Anishchenko, I., Park, H., Peng, Z., Ovchinnikov, S., and Baker, D. (2020). Improved protein structure prediction using predicted interresidue orientations. Proc Natl Acad Sci U S A *117*, 1496-1503.

Yim, W.W., Yamamoto, H., and Mizushima, N. (2022). A pulse-chasable reporter processing assay for mammalian autophagic flux with HaloTag. Elife *11*.

Yoshii, S.R., Kuma, A., Akashi, T., Hara, T., Yamamoto, A., Kurikawa, Y., Itakura, E., Tsukamoto, S., Shitara, H., Eishi, Y., and Mizushima, N. (2016). Systemic Analysis of Atg5-Null Mice Rescued from Neonatal Lethality by Transgenic ATG5 Expression in Neurons. Dev Cell *39*, 116-130.

Zha, B.S., Wan, X., Zhang, X., Zha, W., Zhou, J., Wabitsch, M., Wang, G., Lyall, V., Hylemon, P.B., and Zhou, H. (2013). HIV protease inhibitors disrupt lipid metabolism by activating endoplasmic reticulum stress and inhibiting autophagy activity in adipocytes. PLoS One *8*, e59514.

Zhao, D., Zou, C.X., Liu, X.M., Jiang, Z.D., Yu, Z.Q., Suo, F., Du, T.Y., Dong, M.Q., He, W., and Du, L.L. (2020). A UPR-Induced Soluble ER-Phagy Receptor Acts with VAPs to Confer ER Stress Resistance. Mol Cell *79*, 963-977.e963.

Zou, Y., He, W., Wang, K., Han, H., Xiao, T., Chen, X., Zhou, B., Tan, J., Xia, K., Tang, B., Chen, C., Shen, L., Yan, R., and Zhang, Z. (2018). Identification of rare RTN3 variants in Alzheimer's disease in Han Chinese. Hum Genet *137*, 141-150.

ˇverbye, A., Fengsrud, M., and Seglen, P.O. (2007). Proteomic analysis of membrane-associated proteins from rat liver autophagosomes. Autophagy *3*, 300-322.